Solid Solution Pt_xRh_{1-x} Nanoparticles

Synthesis, Characterization, Catalyst Preparation and Thermal Stability Evaluations

Walace Peterle Soares Kierulf-Vieira

Master Thesis in Chemistry

60 credits

Department of Chemistry
Faculty of Mathematics and Natural Sciences

UNIVERSITY OF OSLO

June 2022

Solid Solution Pt_xRh_{1-x} Nanoparticles

Synthesis, Characterization, Catalyst Preparation and Thermal Stability Evaluations

2022

Solid Solution Pt_xRh_{1-x} Nanoparticles – Synthesis, Characterization, Catalyst Preparation and Thermal Stability Evaluations

Walace Peterle Soares Kierulf-Vieira

http://www.duo.uio.no/

Print: Reprosentralen, Universitetet i Oslo Trykk: Reprosentralen, Universitetet i Oslo

Acknowledgements

I would like to thank my supervisors Prof. Anja O. Sjåstad and Martin Jensen for all the help and guidance throughout this project.

I would also like to thank:
Kirsten Kierulf-Vieira for unconditional love, patience, and support.
Eva Kierulf-Vieira for being cute and sweet.
Bruno Gonano for constructive feedback.
Salah Bra Amedi for technical support.
Prof. Patricia Kooyman for assistance with sample analysis.
My parents-in-law Petter and Sigrun for support and babysitting.
My parents for teaching me the value of hard work.

Abstract

The goal of this master's thesis was to develop well-defined model catalysts for selective oxidation of NH_3 into N_2, through the synthesis of solid solution Pt_xRh_{1-x} nanoparticles with homogeneous element distribution, deposition of the nanoparticles on Al_2O_3 support, and testing of the thermal stability of the produced solid solution $Pt_{0.50}Rh_{0.50}$ nanoparticles by *in situ* scanning transmission electron microscopy (STEM).

We started with concurrent trials to produce Pt_xRh_{1-x} by the heat-up method using an autoclave and a reflux. Through the autoclave method, we produced monodispersed well-defined nanoparticles of monometallic Pt using $Pt(acac)_2$ as a precursor in toluene, and using the mixed surfactants oleyl amine and trioctylphosphine. Although the developed procedure was promising, the experimental work using the autoclave was halted, as we reached the goal of synthesizing Pt_xRh_{1-x} using the heat-up method.

The heat-up method using a reflux was developed to produce solid solution Pt_xRh_{1-x} nanoparticles in ethylene glycol using polyvinylpyrrolidone (PVP) as a surfactant, despite differences in the relative kinetics of $Pt(acac)_2$ and $Rh(acac)_3$ precursors. A novel step was introduced to account for the different reaction kinetics of the two metal precursors. For this system, the kinetics of $Rh(acac)_3$ was faster than that of $Pt(acac)_2$, but we identified a reaction window where both precursors were reacting at the same time. By halting the synthesis before the $Rh(acac)_3$ was depleted, it was demonstrated that solid solution Pt_xRh_{1-x} nanoparticles with homogeneous element distribution could be synthesized for $0 < x < 1$. The result was verified by energy-dispersive X-ray spectroscopy (EDS) elemental mapping, and the unit cell dimensions were extracted from powder X-ray diffraction data. The stoichiometry of the nanoparticles was verified by EDS, inductively coupled plasma - optical emission spectrometry (ICP-OES) and Vegard's law considerations based on the nanoparticles' unit cell dimensions.

Procedures to obtain well-defined catalysts of Pt/Al_2O_3 and $Pt_{0.5}Rh_{0.5}/Al_2O_3$ with a targeted metal loading of 0.5 weight % were developed using the concept of depositing as-synthesized nanoparticles directly onto the Al_2O_3 support. Pt and solid solution $Pt_{0.5}Rh_{0.5}$ nanoparticles were first synthesized by the heat-up method using a reflux. In order to ensure good dispersion of the nanoparticles on the oxide material, a series of trial and error experiments were carried out

varying the sonication method and the solvent used during the deposition step. Additionally, the role of surfactant concentration during the nanoparticle synthesis step was investigated. Scanning electron microscopy (SEM) imaging in low angle backscattered electron mode was used to document that highly dispersed Pt and $Pt_{0.50}Rh_{0.50}$ nanoparticles on Al_2O_3 is only achievable when using a higher surfactant concentration than previously reported (338 mM *versus* 1 to 250 mM). The metal loading was tested by ICP-OES and we found that the metal loading was 0.56 weight % for the Pt nanoparticles and 0.61 weight % for the solid solution $Pt_{0.5}Rh_{0.5}$ nanoparticles.

The thermal stability of the solid solution Pt_xRh_{1-x} nanoparticles, where x ranged from 0.40 ± 0.03 to 0.52 ± 0.03, was explored using *in situ* STEM in ultra-high vacuum (UHV) in the temperature range from room temperature to 600 °C. Nanoparticles in the size range of 5.7 to 14 nm were measured. For the experiment, EDS maps and high-angle annular dark field images of the nanoparticles were obtained at room temperature, at 300 and 600 °C, and at room temperature again after exposure to heat (in total, 300 °C for one hour and 600 °C for 4.5 hours). Data analysis was carried out in a manner that excluded beam damage. The results demonstrated that the as-synthesized Pt_xRh_{1-x} nanoparticles were in solid solution before heating, during the *in situ* STEM measurements, and after the *in situ* STEM measurements. The results indicate that the solid solution configuration was not altered by exposure to 300 °C for one hour and 600 °C for 4.5 hours in UHV, indicating that a solid solution can be the stable configuration in the studied temperature interval at UHV. However, the potential influence of the surfactant on the stability of the nanoparticles was not accounted for, and requires further investigations.

Abbreviations

ccp: Cubic close-packed

CIF: Crystallographic information files

EDS: Energy-dispersive X-ray spectroscopy

HAADF: High-angle annular dark-field

ICP-MS: Inductively coupled plasma - mass spectroscopy

ICP-OES: Inductively coupled plasma - optical emission spectrometry

NP: Nanoparticle

OAm: Oleylamine

PVP: Polyvinylpyrrolidone

PXRD: Powder X-ray diffraction

SE: Secondary electron

SEM: Scanning electron microscopy

STEM: Scanning transmission electron microscopy

TOP: Trioctylphosphine

UHV: Ultra-high vacuum

UV-VIS: Ultraviolet–visible spectroscopy

XPS: X-ray photoelectron spectroscopy

Table of Contents

1 Introduction

1.1 Background

At least 60 % of commercialized chemicals are currently made using catalysts, and about 90 % of chemical processes involve catalysis[1]. Industries are motivated to produce catalysts that use less energy and have a higher selectivity for the desired product. Catalyst development involves the synthesis, characterization, and investigation of model materials. The knowledge developed through the systematic fundamental studies of model catalysts is translated into optimized industrial catalysts. The model materials must be well defined regarding particle size, shape, and composition. In addition, their performance and reaction mechanisms should preferably be investigated using tools that facilitate studies under realistic process conditions.

1.2 Nanomaterials

From the stone– to the silicon age, functional materials have defined the epochs in human history. Today, nanotechnology is steadily becoming omnipresent in our lives. Nanomaterials are present in different sectors, from medicine, computing, data storage, catalysis, and energy harvesting to sunscreen and cosmetics[2]. Perhaps we could now be in the dawn of the "nano–era"[2].

Nanoscale materials are generally defined as materials between one to 100 nm in at least one dimension. For perspective, 1 nm equals 10^{-9} m, and the diameter of hydrogen- and gold atoms are 25- and 160 Å, respectively[3]. In addition, nanomaterials are classified according to their dimensionality. Nanoparticles are zero-dimensional (0D), nanorods and nanowires are one-dimensional (1D), and thin films are two-dimensional (2D) nanomaterials. Finally, bulk materials are three-dimensional (3D).

Nanomaterials possess unique physical and chemical characteristics when compared to their bulk counterpart. For example, nanomaterials have a lower melting point when compared to bulk. Atoms at the surface of materials are less coordinated when compared to the sub-surface atoms. When the particle becomes smaller, the percentage of atoms on the surface increase. For that reason, nanoparticles have lower cohesive energy and thus require less thermal energy to undergo surface-induced melting[4]. Gold, for example, has a bulk melting point of 1064 °C, but gold nanoparticles in the range of 3 to 4 nm melt at room temperature[5] (Figure 1.1).

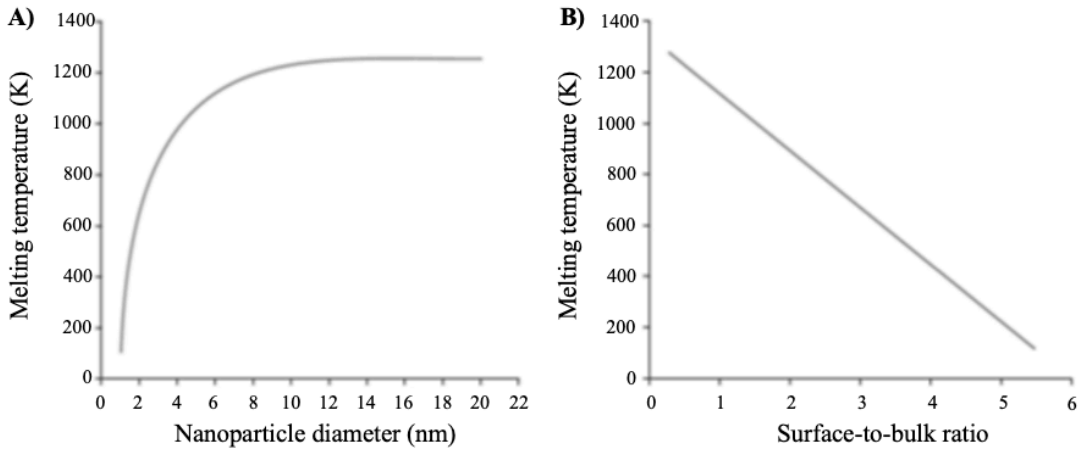

Figure 1.1: The nano-effect on the melting point of Au. A) Melting point of Au nanoparticles as a function of the nanoparticle diameter; B) Melting point of Au nanoparticles as a function of the surface-to-bulk ratio. Figure adapted from Rogers[6].

Another size-dependent effect is the transition from ferri– and ferromagnetism to superparamagnetism. Superparamagnetism arises when the nanoparticle becomes smaller than the ferri– or ferro domain. When that happens, each nanoparticle has a single magnetic domain. The effect usually arises in nanoparticles smaller than 3-50 nm, depending on the material. The consequence of superparamagnetism is the loss of the hysteresis loop observed in magnetization measurements as a function of the application of an external magnetic field (Figure 1.2). Superparamagnetic nanoparticles are of technological relevance within biomedicine[7] and data storage[8].

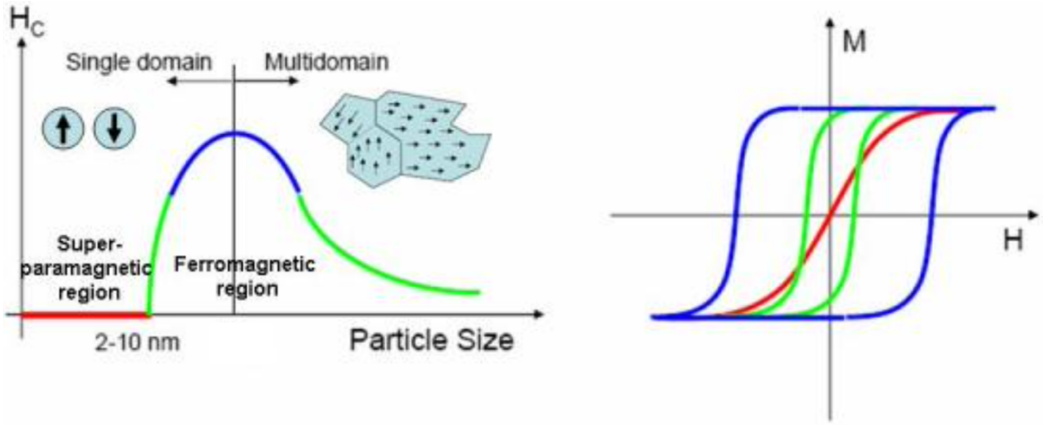

Figure 1.2: The effects of superparamagnetism. Left: Residual magnetism (H_C) as a function of particle size; Right: Hysteresis loop during magnetization (M) as function of the external magnetic field (H). Figure adapted from Kim[9].

The bandgap of semiconductor nanomaterials can be tuned by adjusting the nanoparticle size. In single atoms, electrons are present in atomic orbitals. The atomic orbitals combine into molecular orbitals with discrete energy levels in molecules. In larger atomic clusters to nanoparticles, the discrete energy levels start to overlap until they are finally characterized as a continuous energy level in bulk materials (Figure 1.3). Consequently, the bandgap of semiconductor nanomaterials can be tuned by controlling the size, where smaller nanomaterials have a larger bandgap. Optical effects, such as light emission, are also observed when the energy levels are discrete at the rim of the valence- and conduction bands (quantum dots). Bandgap tuning is widely used in industrial activities where semiconductors are central, such as electronics and optics.

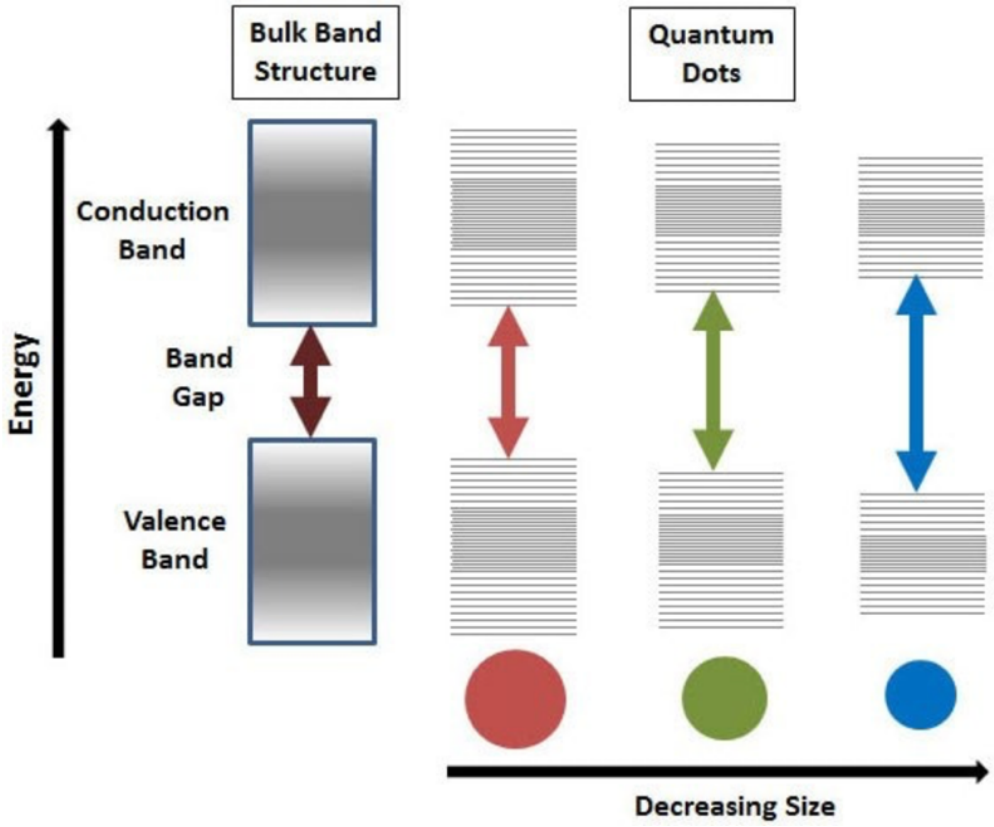

Figure 1.3: Nanoparticle size as a function of the bandgap of a semiconductor. Note that the energy levels in both the valence- and conduction band become discrete (in the figure called Quantum Dots. Figure adapted from Sigma Aldrich[10].

Nanomaterials have a larger surface area when compared to bulk. As particles become small, a higher fraction of atoms per mass of material is on the surface (Figure 1.4). The increase in surface

area is especially beneficial for catalysis, as heterogeneously catalyzed reactions happen on the surface of the material[11].

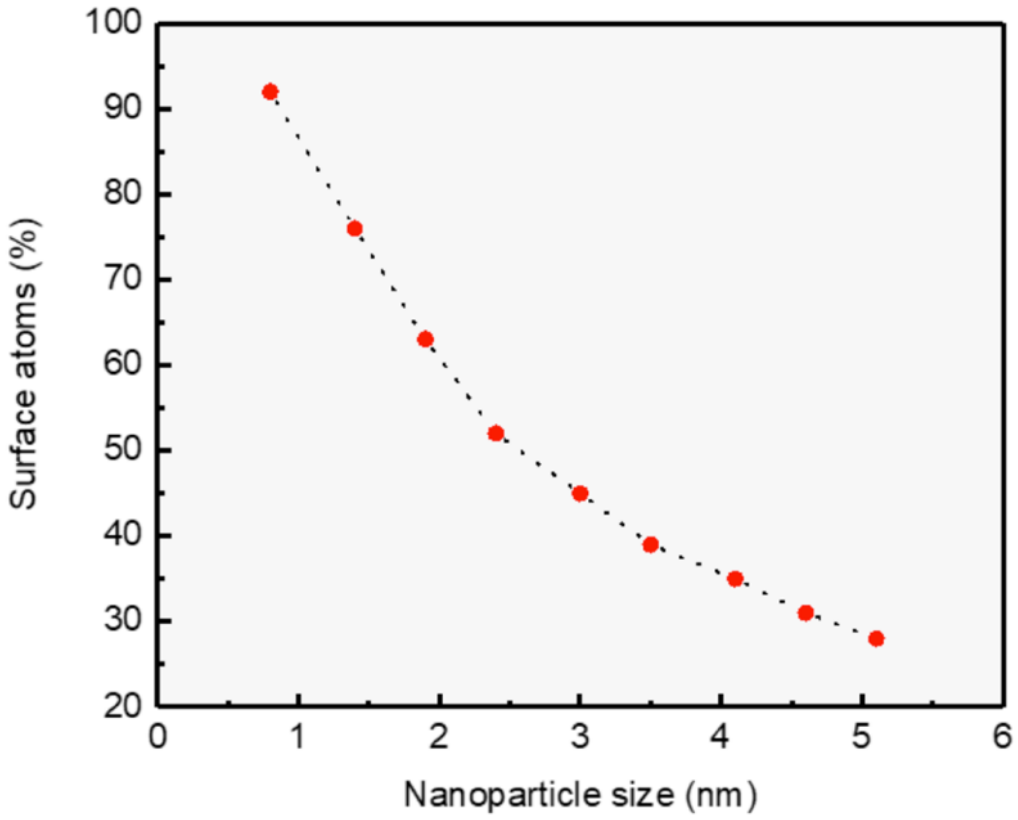

Figure 1.4: Surface area atoms percentage of cuboctahedra platinum nanoparticles versus nanoparticle size. Figure adapted from Xiong[12].

1.3 Catalytic oxidation of NH_3

The products of the oxidation of ammonia could be either N_2, NO, or N_2O and H_2O (Equations 1.1, 1.2, and 1.3).

$$4NH_3(g) + 5O_2(g) \rightarrow 4NO(g) + 6H_2O(g) \quad (1.1)$$

$$4NH_3(g) + 4O_2(g) \rightarrow 2N_2O(g) + 6H_2O(g) \quad (1.2)$$

$$4NH_3(g) + 3O_2(g) \rightarrow 2N_2(g) + 6H_2O(g) \quad (1.3)$$

Ammonia oxidation is crucial for producing artificial fertilizers and for environmental applications. High selectivity toward NO formation (Equation 1.1) is vital for fertilizer production.

This is achievable over Pt-Rh wires woven into nets acting as catalysts operated at typically 900 °C and 2-13 bar of pressure, using $65/35$ ratio of O_2/NH_3[13]. The NO is subsequently oxidized to NO_2, followed by a reaction with water to form HNO_3[14].

For NO_x abatement applications, intermediate-temperature oxidation of ammonia is essential in order to obtain N_2 as the main product (Equation 1.2). Here, unreacted ammonia from the selective catalytic reduction (SCR) unit, which uses NH_3 to reduce NO_x to N_2, is selectively oxidized to N_2 (Equation 1.3). This reaction is frequently referred to as the ammonia "slip" oxidation and is usually done at the $99/1$ ratio of O_2/NH_3. The temperature range for this procedure is 200-500 °C. In addition, Pt-Rh nanoparticles supported on oxides have shown to be promising as catalysts for this reaction[15]. The formation of N_2O (Equation 1.2) is undesired for both the described applications.

1.4 Background information on solid solution Pt_xRh_{1-x} nanoparticle systems

The literature search for previous work on Pt_xRh_{1-x} nanoparticles is limited to the synthesis using the *polyol synthesis* method (Methods and Theory 2.4.1), which relies on using a polyalcohol acting both as the solvent and reducing agent. In addition, we restrict the survey to synthesis that used polyvinylpyrrolidone (PVP) as a surfactant. Table 1.1 presents relevant previous publications on the synthesis of Pt_xRh_{1-x} nanoparticles and Figure 1.5 shows nanoparticles from the syntheses reported in Table 1.1. Syntheses of monometallic Rh nanoparticles are not reported as their preparation was not attempted in this Master's thesis.

Table 1.1: Summary of results from previous works to synthesize Pt and solid solution Pt_xRh_{1-x} nanoparticles using the polyol route and PVP as surfactant. An image from the nanoparticles produced by each group reported in Table 1.1 was selected and shown in Figure 1.5. PVP, polyvinylpyrrolidone; NP, nanoparticle; UV-VIS, ultraviolet–visible spectroscopy; TEM, transmission electron microscopy; PXRD, powder X-ray diffraction; XPS, X-ray photoelectron spectroscopy; EDS, energy-dispersive X-ray spectroscopy; ICP–MS, inductively coupled plasma - mass spectroscopy; STEM, scanning transmission electron microscopy.

Reference	**Precursors + Solvent**	**Pt_xRh_{1-x} x =**	**$\sum(Pt + Rh)$ (mM)**	**Molar ratio $\frac{[PVP]}{[Metal]}$**	**Synthesis Temperature (°C)**	**Synthesis duration (hours)**	**NP size (nm)**	**Characterization method**
Hei *et al.*[16] (2012) Figure 1.5 A	H_2PtCl_6 Ethylene glycol	1	0.1 0.3 0.6 1.2 2.4 4.8 0.1 0.1 0.1 0.1 0.1	10/1 10/1 10/1 10/1 10/1 10/1 5/1 10/1 15/1 20/1 40/1	190 190 190 190 190 190 190 190 190 190 190	2 2 2 2 2 2 2 2 2 2 2	3.2 4.6 5.7 6.1 6.4 4.1 ~4.9 ~4.8 ~5.0 ~15 ~25	UV–VIS TEM
Long *et al.*[17] (2011) Figure 1.5 B	H_2PtCl_6 Ethylene glycol	1	41.6	6/1	160	0.17 to 0.5 (*10– 30 min*)	~ 8	UV–VIS PXRD TEM
Papa *et al.*[18] (2011) Figure 1.5 C	H_2PtCl_6 Ethylene glycol	1	38	10/1	120	1	4.9	TEM XPS PXRD
Han *et al.*[19] (2008) Figure 1.5 D	H_2PtCl_6 Ethylene glycol	1	1	9/1	180	1	3.6	TEM

Table 1.1 (Continuation): Summary of results from previous works to synthesize Pt and solid solution Pt_xRh_{1-x} nanoparticles using the polyol route and PVP as surfactant. An image from the nanoparticles produced by each group reported in Table 1.1 was selected and shown in Figure 1.5. PVP, polyvinylpyrrolidone; NP, nanoparticle; UV-VIS, ultraviolet–visible spectroscopy; TEM, transmission electron microscopy; PXRD, powder X-ray diffraction; XPS, X-ray photoelectron spectroscopy; EDS, energy-dispersive X-ray spectroscopy; ICP–MS, inductively coupled plasma - mass spectroscopy; STEM, scanning transmission electron microscopy.

Song *et al.*[20] (2005) Figure 1.5 E	H_2PtCl_6 Ethylene glycol	1	13	12/1	197	0.083 (*5 min*)	9.4 ± 0.6	TEM UV–VIS PXRD
Herricks *et al.*[21] (2004) Figure 1.5 F	H_2PtCl_6 Ethylene glycol	1	10	2.6/1	160	not specified	3 – 5 nm	TEM
Koebel *et al.*[22] (2008) Figure 1.5 G	H_2PtCl_6 Ethylene glycol	1	1.3 2.7 5.3 7.9	9/1	120	0.25 (*15 min*)	3.12 ± 0.54 4.65 ± 0.66 6.05 ± 0.69 7.81 ± 1.19	TEM
Safo *et al.*[23] (2019) Figure 1.5 H	H_2PtCl_6 Ethylene glycol	1	2.6 2.6 2.6	3/1 6/1 12/1	Not specified	0.25 (*15 min*)	~8.0 ~7.7 ~7.5	TEM
Park *et al.*[24] (2008) Figure 1.5 I	$Pt(acac)_2$ $Rh(acac)_3$ 1,4–butanediol	1 0.8 0.6 0.5 0.4 0.2	5 2.5 1.25 1.25 1.25 1.25	10/1	215 220 225 225 225 225	1 1 1 1 2 1.5	9.2 ± 2.4 9.3 ± 1.2 8.1 ± 0.8 8.5 ± 0.9 9.2 ± 1.1 9.5 ± 1.8	TEM XPS
Alayoglu *et al.*[25] (2008) Figure 1.5 J	$Pt(acac)_2$ $Rh(CO)_4Cl_2$ Ethylene glycol	0.5	10	2.5/1	170	2	4.9	XPS EDS line–scan

Table 1.1 (Continuation): Summary of results from previous works to synthesize Pt and solid solution Pt_xRh_{1-x} nanoparticles using the polyol route and PVP as surfactant. An image from the nanoparticles produced by each group reported in Table 1.1 was selected and shown in Figure 1.5. PVP, polyvinylpyrrolidone; NP, nanoparticle; UV-VIS, ultraviolet–visible spectroscopy; TEM, transmission electron microscopy; PXRD, powder X-ray diffraction; XPS, X-ray photoelectron spectroscopy; EDS, energy-dispersive X-ray spectroscopy; ICP–MS, inductively coupled plasma - mass spectroscopy; STEM, scanning transmission electron microscopy.

Musselwhite *et al.*[26] (2013) Figure 1.5 K	H_2PtCl_6 $Pt(acac)_2$ $Rh(acac)_3$ Triethylene glycol	1 0.9 0.8 0.8	10 10 10 10	2.5/1	230 230 230 230	1 1 1 1	6.5 6.5 6.5 2.5	XPS EDS map
Park *et al.*[27] (2011) Figure 1.5 L	$Pt(acac)_2$ $Rh(acac)_3$ 1,4–butanediol	0.5 0.5 0.5 0.5	0.625 1.25 5 10	10/1	220 220 220 220	2 2 2 2	6.8 ± 0.6 5.7 ± 0.7 8.5 ± 1.1 11.0 ± 1.7	TEM XPS
Muri[28] (2015) Figure 1.5 M	$Pt(acac)_2$ $Rh(acac)_3$ 1,4–butanediol	1 1 0.2 0.5 0.5 0.8	10 10 10 10 10 10	10/1	220 190 to 230 220 220 190 to 230 220	0.5 to 3 2 2 0.5 to 3 2 2	9.1 to 16.7 9.1 to 15.8 6.0 ± 1.4 6.0 to 7.4 6.3 to 7.4 7.4 ± 1.5	STEM PXRD ICP–MS
Bundli *et al.*[29] (2019) Figure 1.5 N	$Pt(acac)_2$ $Rh(acac)_3$ 1,4–butanediol	0.2 to 0.5	10	10/1	190 to 230	1 to 5	~7	PXRD STEM EDS

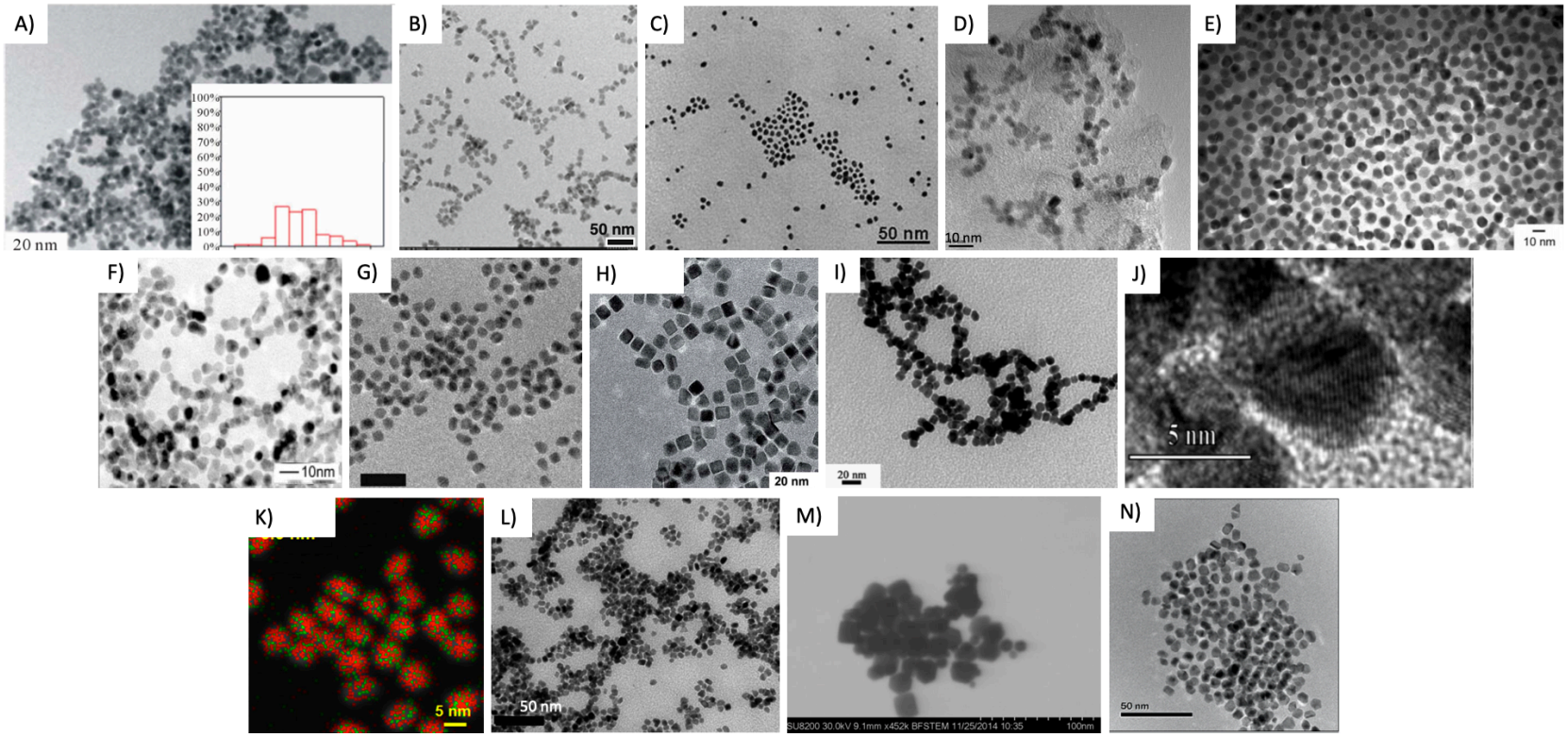

Figure 1.5: Selected images from the nanoparticles produced by each group are reported in Table 1.1. A) Pt nanoparticles from Hei et al.[16], B) Pt nanoparticles from Long et al.[17], C) Pt nanoparticles from Papa et al.[18] (2011), D) Pt nanoparticles from Han et al.[19], E) Pt nanoparticles from Song et al.[20], F) Pt nanoparticles from Herricks et al.[21], G) Pt nanoparticles from Koebel et al.[22], H) Pt nanoparticles from Safo et al.[23], I) Pt nanoparticles from Park et al.[24], J) Solid solution $Pt_{0.5}Rh_{0.5}$ nanoparticles from Alayoglu et al.[25], K) Solid solution $Pt_{0.80}Rh_{0.20}$ nanoparticles from Musselwhite et al.[26], L) Solid solution $Pt_{0.5}Rh_{0.5}$ from Park et al.[27], M) Pt nanoparticles from Muri[28], N) Solid solution $Pt_{0.5}Rh_{0.5}$ nanoparticles from Bundli et al.[29]

The bulk Pt–Rh system

The end members in the Pt–Rh system, Pt and Rh, when in bulk, pack their atoms in cubic close packing (ccp) crystal structures described in space group Fm–3m[30]. In addition, according to the binary Pt-Rh phase diagram (Figure 1.6), all compositions of Pt_xRh_{1-x}, where $0 \leq x \leq 1$, form a solid solution at temperatures above 760 °C. Table 1.2 reports previously measured a-axis values for Pt, Rh, and $Pt_{0.5}Rh_{0.5}$ in bulk. Furthermore, the phase diagram predicts that below 760 °C, phase separation occurs, giving a Pt- and an Rh-rich phase, both crystallizing in a ccp crystal structure.

On the other hand, the phase diagram for nanomaterials diverges from the bulk[31]. In small nanoparticles, the surface area dominates the total Gibbs energy of the system, resulting in a shift in the solubility lines present in the bulk phase diagram[31]. For example, nanoparticles in the solid solution configuration of immiscible Pd and Ru[32], Ag and Rh[33], Au and Ru[34], and Cu and Ru[35] have been previously synthesized.

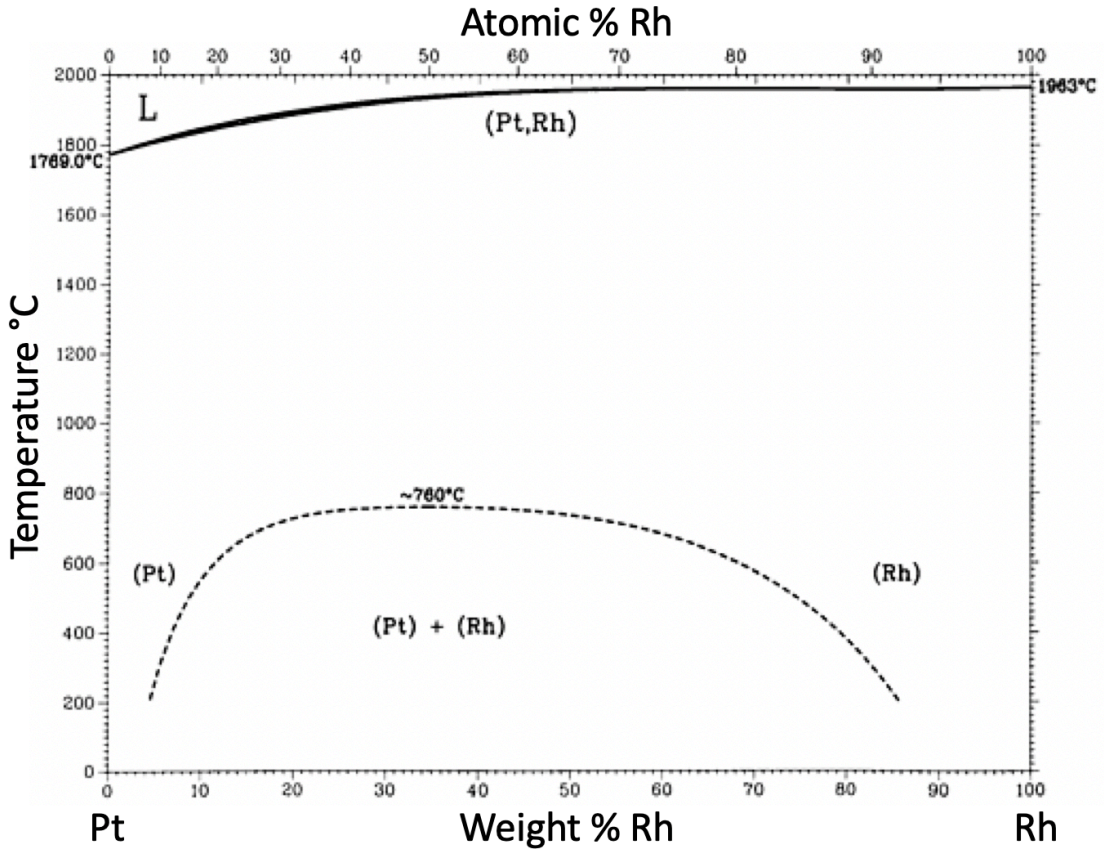

Figure 1.6: Binary phase diagram for the Pt–Rh system in bulk. Figure adapted from ASM International[30].

Table 1.2: Reported a-axis values for Pt, Rh, and $Pt_{0.5}Rh_{0.5}$ in bulk.

Reference	Pt (Å)	$Pt_{0.5}Rh_{0.5}$ (Å)	Rh (Å)
Nuding *et al.*[36] (1997)			3.8033
Arblaster [37] (1997)			3.8034 ± 0.0002
Raub[38] (1959)		3.858	
Raub *et al.*[39] (1964)		3.864	
Arblaster (1997)[40]	3.9236 ± 0.0006		
Gibaud *et al.*[41] (2009)	3.9276		

Pt_xRh_{1-x} nanoparticles

Although the bulk phase diagram predicts phase segregation of Pt and Rh, nanoparticles having the solid solution configuration have been obtained using the polyol method[24–29,42]. On the other hand, much of the early works report the atomic composition obtained from X-ray photoelectron spectroscopy (XPS), giving thus little to no information on atomic distribution within the nanoparticles. Energy-dispersive X-ray spectroscopy (EDS) line scans or EDS maps are usually used to report the atomic distribution of bimetallic nanoparticles. Based on an EDS line scan, Alayoglu *et al.*[25] reported synthesizing solid solution $Pt_{0.5}Rh_{0.5}$ nanoparticles (Figure 1.7 A). Bundli *et al.*[29] used an EDS map to show that a thin shell of Pt forms on the solid solution ($Pt_{0.5}Rh_{0.5}$) nanoparticles synthesized using the co-reduction route (Figure 1.7 B). Musselwhite et al.[26] reported a synthesis method that produced a solid solution Pt–Rh core with an Rh enriched shell. For an overview of previously established Pt_xRh_{1-x} solid solution syntheses, see Table 1.1. Table 1.3 reports nanoscale a-axis values for Pt, Rh, and $Pt_{0.5}Rh_{0.5}$.

Table 1.3: Reported a-axis values for Pt, Rh, and $Pt_{0.50}Rh_{0.50}$ on the nanoscale.

Reference	Pt (Å)	$Pt_{0.50}Rh_{0.50}$ (Å)	Rh (Å)
Kalyva *et al.*[43] (2017)	3.9171 ± 0.0001		3.8351 ± 0.0001
Song *et al.*[44] (2018)			3.8094 to 3.8133
Salgado *et al.*[45] (2008)	3.91211 to 3.92185		
Muri[28] (2015)	3.918 ± 0.005		3.811 ± 0.005
Bundli *et al.*[29] (2019)		3.852 to 3.864[1]	

[1] Variation due different synthesis parameters.

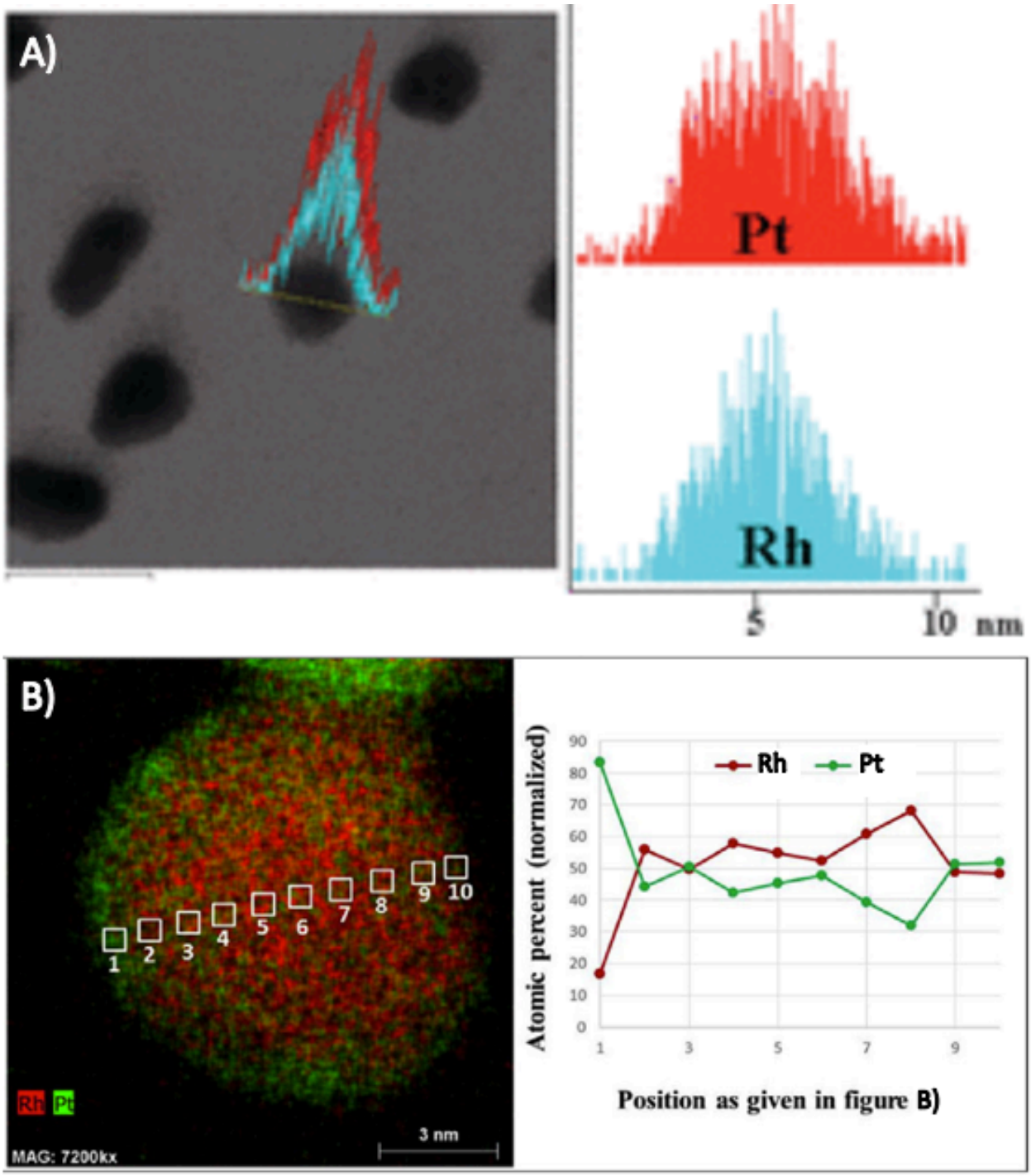

Figure 1.7: Previously synthesized Pt_xRh_{1-x} nanoparticles containing a solid solution Pt_xRh_{1-x} core and a Pt enriched shell. A) EDS line–scan (right) of nanoparticle in bright-field image, images taken from Alayoglu[25]; B) EDS map of nanoparticle (right) with local composition from line–scan (left). Images taken from Bundli[29].

1.5 *In situ* TEM experiment in monometallic Pt nanoparticles

To our knowledge, no previous *in situ* TEM/STEM measurements have been done in the Pt_xRh_{1-x} systems. However, a few *in situ* experiments in a vacuum were done. For example, Wang *et al.*[46] studied the shape transformation and surface melting of Pt nanoparticles as a function of temperature, and Yu *et al*. the thermal wetting of Pt nanocrystals on SiO_2 surfaces.

Wang *et al.*[46] used a colloidal synthesis to prepare Pt nanoparticles that averaged 8 nm in diameter. They used the polymer polyacrylate as a surfactant. After the synthesis, they deposited their sample in an amorphous carbon film supported by a copper grid for the *in situ* TEM experiments. Afterward, they obtained TEM images of the nanoparticles at temperatures ranging from 25 °C to 660 °C (Figure 1.8). They found that the surfactant was removed when the specimen was at a temperature between 180 – 250 °C in a vacuum (Figure 1.8 A to C) and that the particle shape does not change when the temperature is lower than 350 °C (Figure 1.8 A to D), that truncation starts to occur at temperatures between 350- to 450 °C (Figure 1.8 E), and that the nanoparticles adopt a spherical-like shape at temperatures higher than 500 °C (Figure 1.8 F to H).

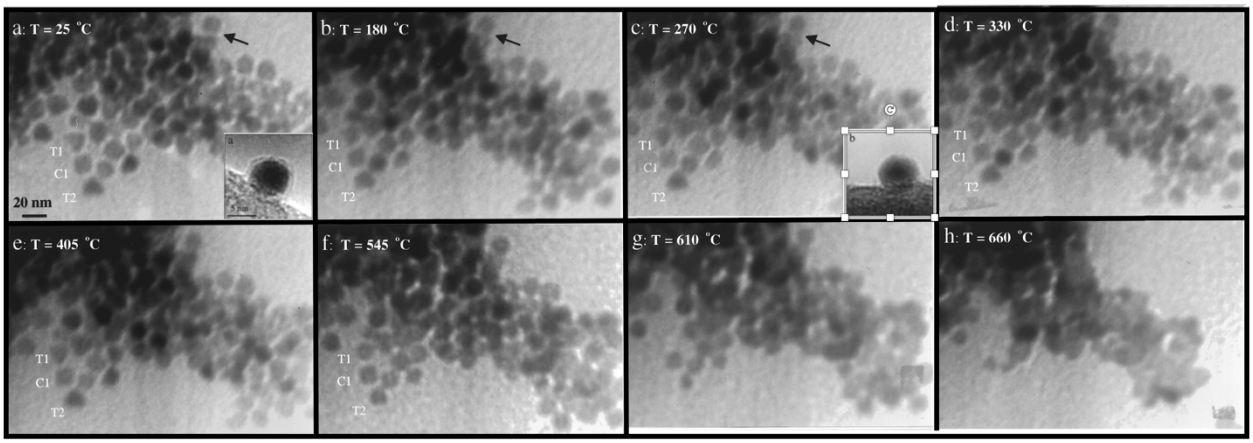

Figure 1.8: *In situ* TEM experiment using Pt nanoparticles. *In situ* TEM image at A) 25 °C, B) 180 °C, C) 270 °C, D) 330 °C, E) 405 °C, F) 545 °C, G) 610 °C, and H) 660 °C showing evaporation of the surfactant (the nanoparticle indicated with a black arrow is magnified on images A and C), coalescing and microscopic melting of an agglomeration of Pt nanoparticles. Images modified from Wang[46].

Yu *et al*.[47] used a colloidal synthesis to prepare Pt nanoparticles that averaged 9 nm in diameter. After the synthesis, they deposited their sample in a copper grid with amorphous SiO_2 film. They obtained *in situ* TEM images from temperatures ranging from 25- to 800 °C. Wetting was measured by the nanoparticle's area change as a function of the temperature the image was

obtained. They reported that Pt nanoparticles wet on the SiO_2 film at temperatures above 500 °C (Figure 1.9). The wetting occurs due to negative interface energy between Pt and SiO_2 that favors the diffusion of Pt onto the SiO_2's surface.

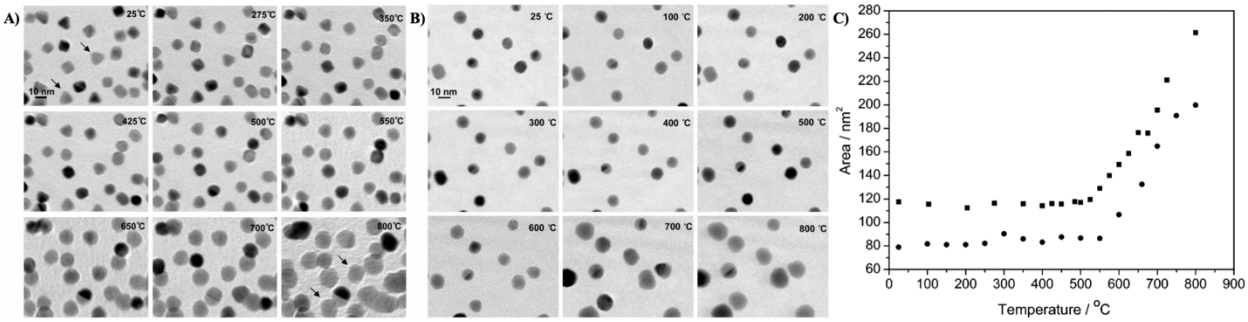

Figure 1.9: *In situ* TEM images of Pt nanoparticles recorded during the heating process. A) Mixed tetrahedral and cubic nanoparticles; B) Cuboctahedral nanoparticles; C) Area in nm^2 as a function of temperature in °C of sample *(A)* represented by squares and sample *(B)* represented by circles. Images modified from Yu[47].

1.6 *Ex situ* TEM experiment in bimetallic Pt_xRh_{1-x} solid solution nanoparticles

A few *ex situ* TEM experiments were done to study the stability of monometallic Pt[48,49] and bimetallic Pt–Rh solid solution nanoparticles[50]. The nanoparticles were synthesized and deposited on a barium hexa-aluminate (BHA) support. The thermal stability of the nanoparticles was tested by calcination in air at temperatures up to 850 °C using a furnace. The as-synthesized and the calcinated samples were characterized by TEM, and the chemical composition was investigated by EDS on single nanoparticles. The critical findings in those experiments were that monometallic nanoparticles are unstable at 600 °C and sinter into larger structures[48–50], but solid solution $Pt_{0.25}Rh_{0.75}$ nanoparticles are stable at temperatures up to 600 °C[50] (Figure 1.10 A). In addition, at temperatures higher than 600 °C, Pt bleeds out of the solid solution $Pt_{0.75}Rh_{0.25}$ nanoparticles[50]. Consequently, monometallic Pt nanoparticles form on the BHA support (Figure 1.10 B to G), and the stoichiometry of the $Pt_{0.75}Rh_{0.25}$ solid solution nanoparticles changes to ~$Pt_{0.67}Rh_{0.33}$ (Figure 1.10 H and I).

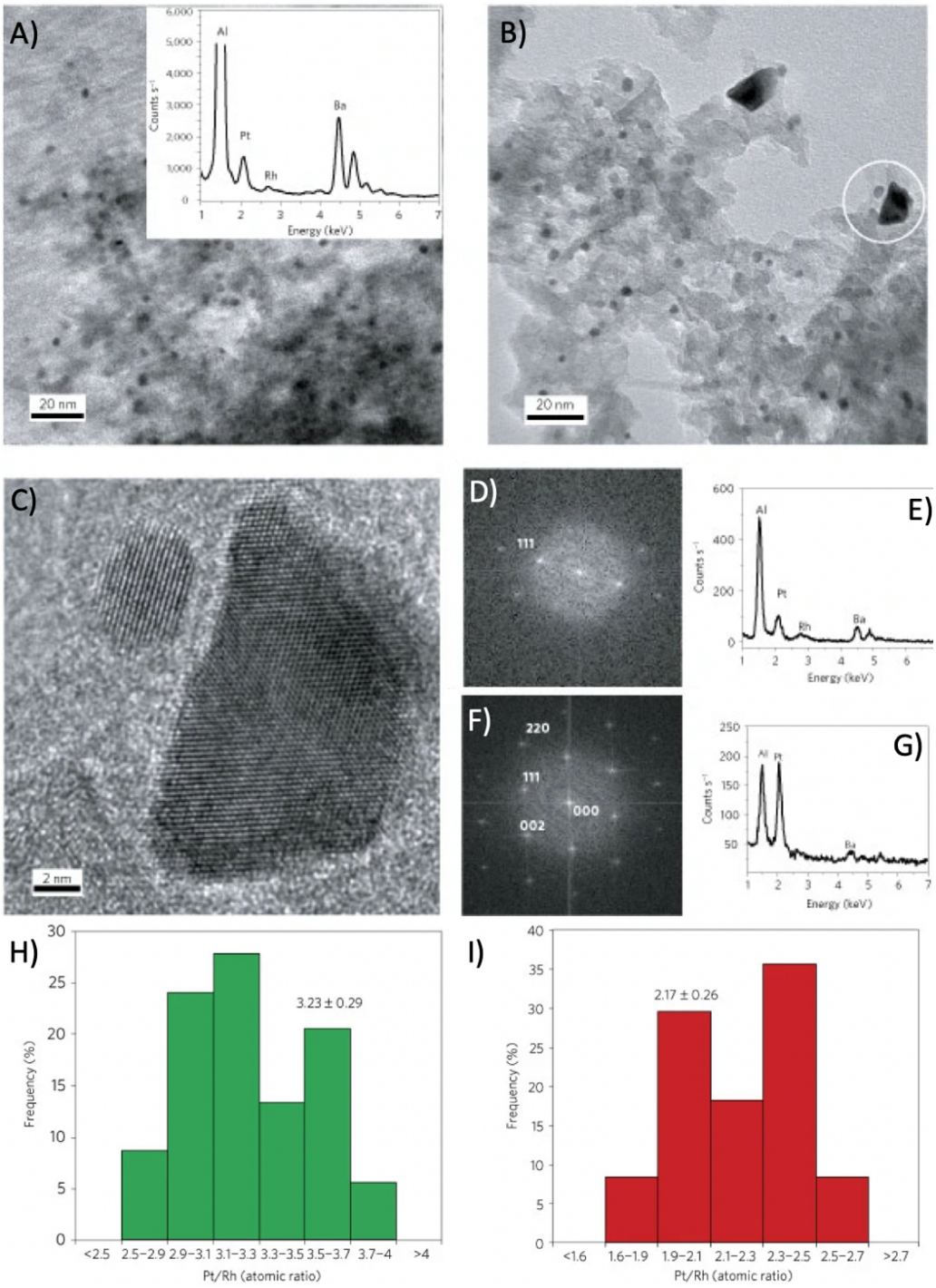

Figure 1.10: *Ex situ* experiment measuring the stability of bimetallic Pt–Rh solid solution nanoparticles. $Pt_{0.75}Rh_{0.25}$ calcined at A) 600 °C (EDS pattern on the inset), B) 700 °C; C) HRTEM image showing an enlarged view of the two representative small and large particles indicated by the white circle in B); D) The FFT pattern and E) EDS spectrum for the smaller particle; F) The FFT pattern and G) EDS spectrum for the larger particle; The composition distribution after calcination at H) 600 °C and I) 700 °C of at least 150 nanoparticles. Images modified from Cao[50].

1.7 Background information on in–situ TEM in bimetallic systems

Since no previous *in situ* TEM measurements have been done in the Pt_xRh_{1-x} systems, some selected studies on other bimetallic systems are presented.

Xing *et al.*[51] studied the thermodynamic stability of $Ag@NiP_x$ core-shell nanoparticles by heating experiments in UHV (Ultra-high vacuum) facilitated by *in situ* STEM. They obtained high-angle annular dark-field (HAADF) images (Figure 1.11 – top row) and EDS maps (Figure 1.11 – bottom row) of the as-synthesized nanoparticles before heating and *in situ* at temperatures up to 500 °C. They found that the $Ag@NiP_x$ core-shell nanoparticles are not stable upon thermal treatment. Figure 1.11 shows that Ag migrates from the core to the surface when heated to 250 °C, forming thus a subclustered segregated nanoparticle (Methods and Theory 2.5 – Figure 2.10). The new structure is stable to up to 450 °C, but when the temperature is increased to 500 °C, Ag sublimates, leaving behind pure $Ni_{12}P_5$ nanoparticles (Figure 1.11).

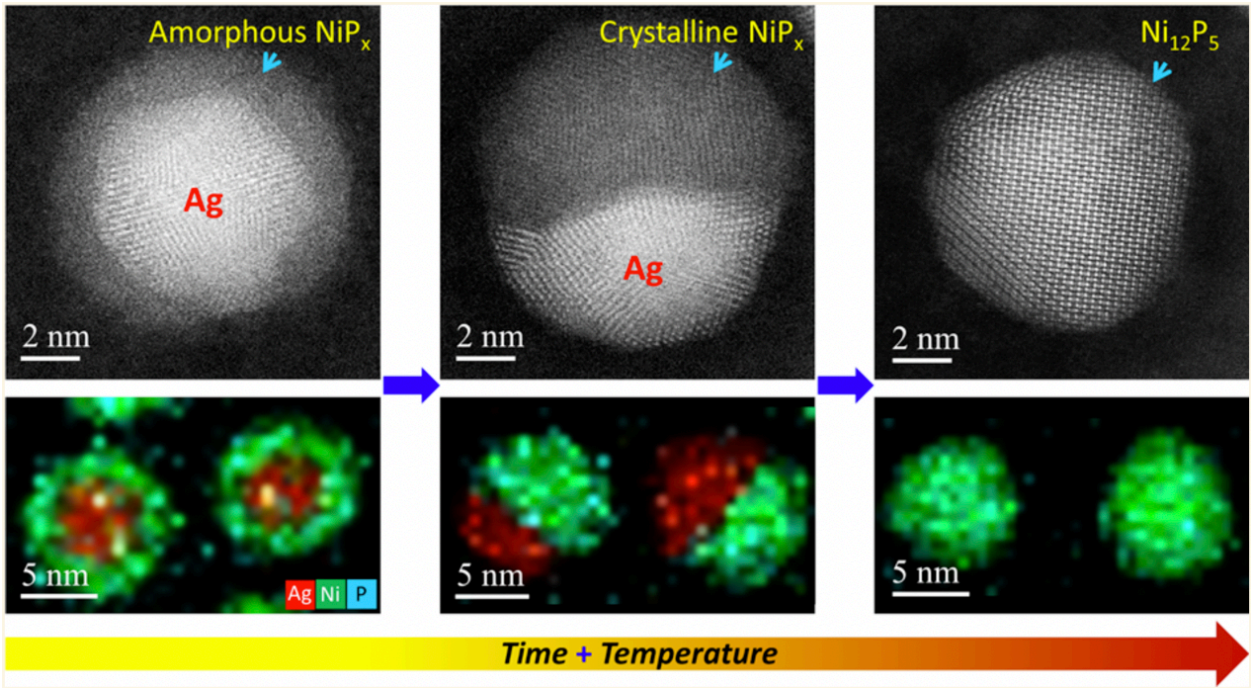

Figure 1.11: In situ STEM measurements of the effects of time and temperature on $Ag@NiP_x$ core-shell nanoparticles. HAADF images on the top, EDS map images on the bottom. The first image depicts the sample at room temperature; The following image depicts the sample in situ at 250 °C; The last image depicts the sample in situ at 500 °C; Images taken from Huang[51]. The EDS signal for Ag is shown in red, Ni in green, and P in blue.

Bonifacio *et al.*[52] studied the thermodynamic stability of Ni@Co core-shell nanoparticles by heating experiments in UHV facilitated by *in situ* STEM. In their experiment, they measured the nanoparticles' atomic distribution using EDS maps as-synthesized at room temperature and then *in situ* at temperatures up to 600 °C. They found that Ni@Co core-shell nanoparticles are stable at temperatures below 440 °C (Figure 1.12 A, B, and C). At temperatures above 440 °C, the surface oxide is removed, and nickel starts to segregate from the core to the shell (Figure 1.12 D and E). When heated to 600 °C, the nanoparticle transforms into a solid solution (Figure 1.12 F).

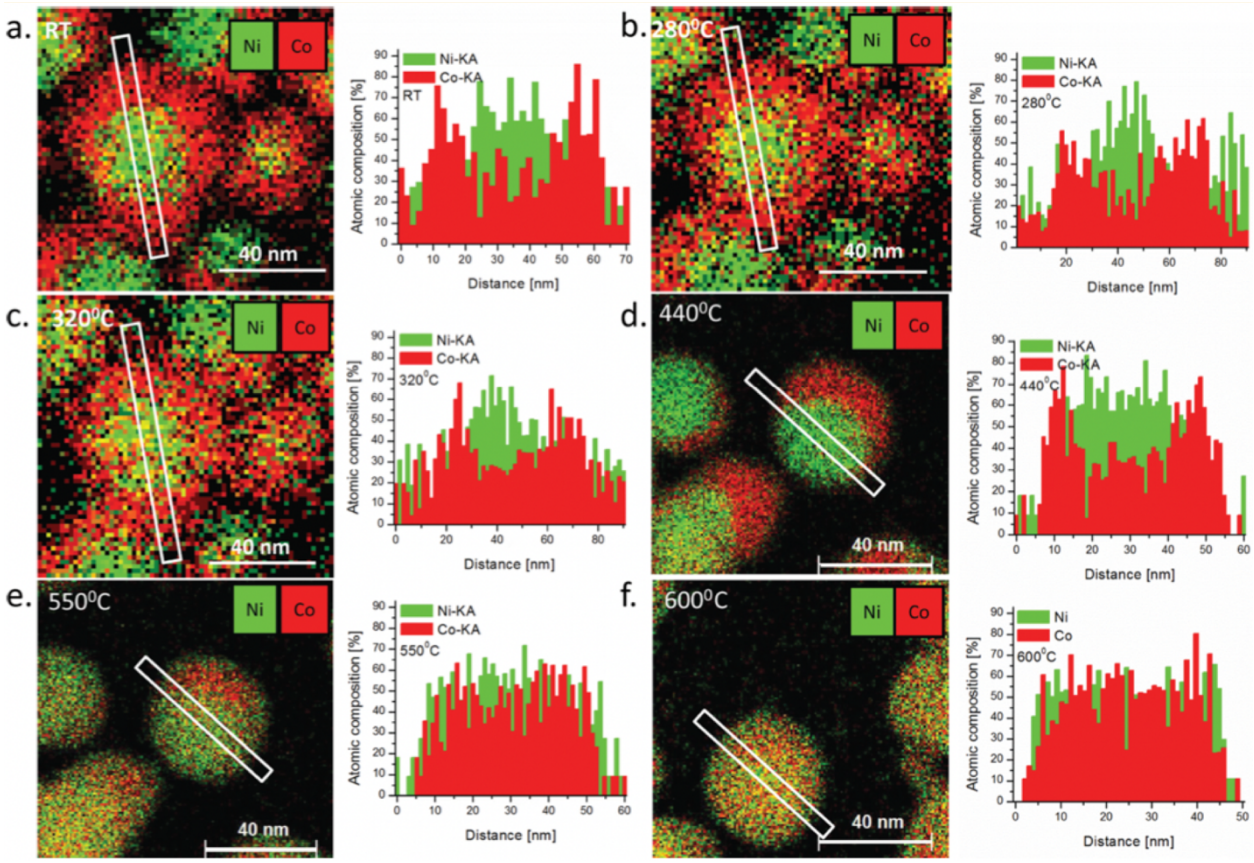

Figure 1.12: In situ STEM measurements of the effects of time and temperature on Ni@Co. A) EDS map series recorded at room temperature and B) in situ at 280 °C, C) 320 °C, D) 440 °C, E) 550 °C, F) 600 °C. A line scan was extracted from the marked particle and is shown to the right of the EDS map. The EDS signal for Ni is shown in green, Co in red. Images taken from Bonifacio[52].

1.8 Motivation

Within the NAFUMA research group, we have for several decades been working on developing synthesis strategies and characterization protocols for producing well-defined model materials. The model materials, with respect to morphology and shape, include surfaces, thin films, nanoparticles, powders, as well as wires woven into nets with a diameter of ~ 100 - 200 μm. The materials are often developed with the purpose of undertaking systematic single parameters studies of various functional properties, including catalyst performance evaluations. With respect to characterization and property studies, the NAFUMA research group is moving in the direction of analyzing the functional properties at pressure, temperature, and gas atmosphere conditions that are relevant for the functional property in question; for instance, through *in situ* studies. When characterizing dynamic structural changes in realistic conditions, while simultaneously measuring the performance of the material, we frequently use the term *operando*.

The motivation behind this master's thesis is to improve our understanding of Pt-Rh metallic nanoparticles. Our purpose is to utilize them in the production of supported model catalysts in ammonia oxidation for NO_x abatement ("NH_3 slip"). Ammonia oxidation for NH_3 slip, can selectively handle oxidation of ppm levels of ammonia into N_2 at ambient pressure in the temperature interval of 200-500 ^oC.

Therefore, a key goal of this master's thesis was to develop colloidal synthesis routes that can provide well-defined Pt_xRh_{1-x} nanoparticles, where parameters such as nanoparticle size, elemental composition and element distribution is controlled, as these parameters are important for designing well performing catalysts. The obtained nanoparticles were therefore characterized with respect to phase content, particle size and, in particular, how the Pt-Rh elements are distributed within the nanoparticles.

The second part the thesis focused on converting the as-synthesized Pt-Rh nanoparticles into supported catalysts; metal-on-support catalysts. A key element of this work was to ensure that the as-synthesized nanoparticles were successfully deposited onto the support material (Al_2O_3), resulting in a catalyst with well dispersed Pt-Rh nanoparticles on Al_2O_3.

The third part of this thesis was dedicated to introductory *in situ* TEM experiments to unravel information on whether the bimetallic Pt_xRh_{1-x} nanoparticles were stable as a solid solution, or

rather in a variant where the two elements were segregated. Effort was put into evaluations on how to avoid beam damage due to electron dosing during the imaging.

For this thesis we used various techniques, such as autoclaves and Schlenk-lines for nanoparticle synthesis, as well as furnace systems, in the preparation of the model catalysts. Powder X-ray diffraction (PXRD) was used for phase identification and refinement of unit cell dimensions of solid solution Pt_xRh_{1-x} nanoparticles. Scanning electron microscopy (SEM) was used for nanoparticle size measurements and for evaluating whether the sample was suitable for further analysis. Finally, TEM was used for analysis of particle size distributions, elemental mapping of individual nanoparticles, as well as for the *in situ* variable temperature experiments.

2 Methods and Theory

2.1 Preparation and mechanisms for the formation of nanoparticles

Nanoparticles can be prepared by the top-down and bottom-up approaches (Figure 2.1). In the top-down methods, external forces break down bulk materials into smaller pieces by applying mechanical force, chemical procedures, or by using other energy sources. The bottom-up approach assembles individual building blocks, often the atoms, into more complex entities.

This work focuses on the bottom-up approach, using solution-phase chemical synthesis, as it allows for control of morphology, atomic arrangement, and chemical composition. It can also be optimized to produce nanoparticles with narrow size distribution[12].

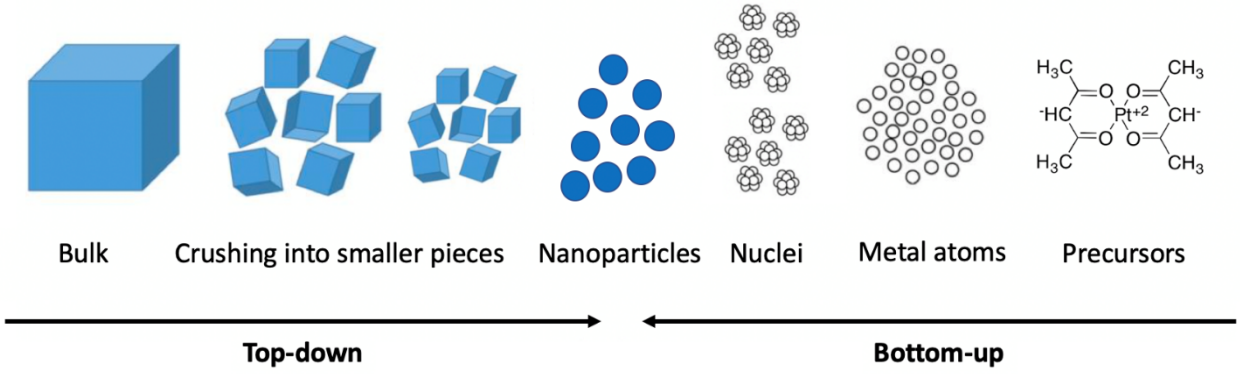

Figure 2.1: Nanoparticle preparation approaches. Figure modified from Jia[53].

The synthesis using the solution-phase chemical approach for monodispersed nanoparticles requires command of the nucleation and growth steps. This subchapter discusses the theory behind nucleation and growth in heterogeneous systems.

2.1.1 Nucleation

Nucleation is the initial process in the formation of a crystal and it can occur in liquid, solid, or gas phases. The nuclei consist of a few atoms, ions, or molecules of the growth species. This master's thesis focuses on the nucleation of solid material from a liquid phase.

There are two types of nucleation processes: heterogeneous and homogeneous. Heterogeneous nucleation occurs at a nucleation site on a solid interface. Homogeneous nucleation requires the system to be in a supercritical state - such as supersaturation[12], leading to the spontaneous formation of this foreign phase.

Homogeneous nucleation

According to thermodynamic considerations, the driving force for nucleation is the reduction in Gibbs free energy from the solvated material to the material in a solid phase (Equation 2.1). Equation 2.1 expresses the total free energy change (ΔG) as the sum of the free energy for the formation of a new volume (ΔG_V) and the free energy for the formation of a new surface (γ), where r corresponds to the cluster radius.

$$\Delta G = -\frac{4}{3}\pi r^3 \Delta G_V + 4\pi r^2 \gamma \tag{2.1}$$

Figure 2.2 shows a plot of the total free energy (ΔG) *versus* the cluster radius from Equation 2.1. The surface energy of Equation 2.1 is always a positive function of the radius squared, while the bulk free energy is always a negative function of the radius cubed. The critical radius (r_c) is the minimal size required for a cluster to be thermodynamically stable, which means that for small clusters ($r < r_c$), the cluster is likely to dissolve again. On the other hand, when $r > r_c$., a nucleus forms and starts to grow. The sum of the volume and surface total free energy at the critical radius provides the activation energy for nucleation (ΔG^*).

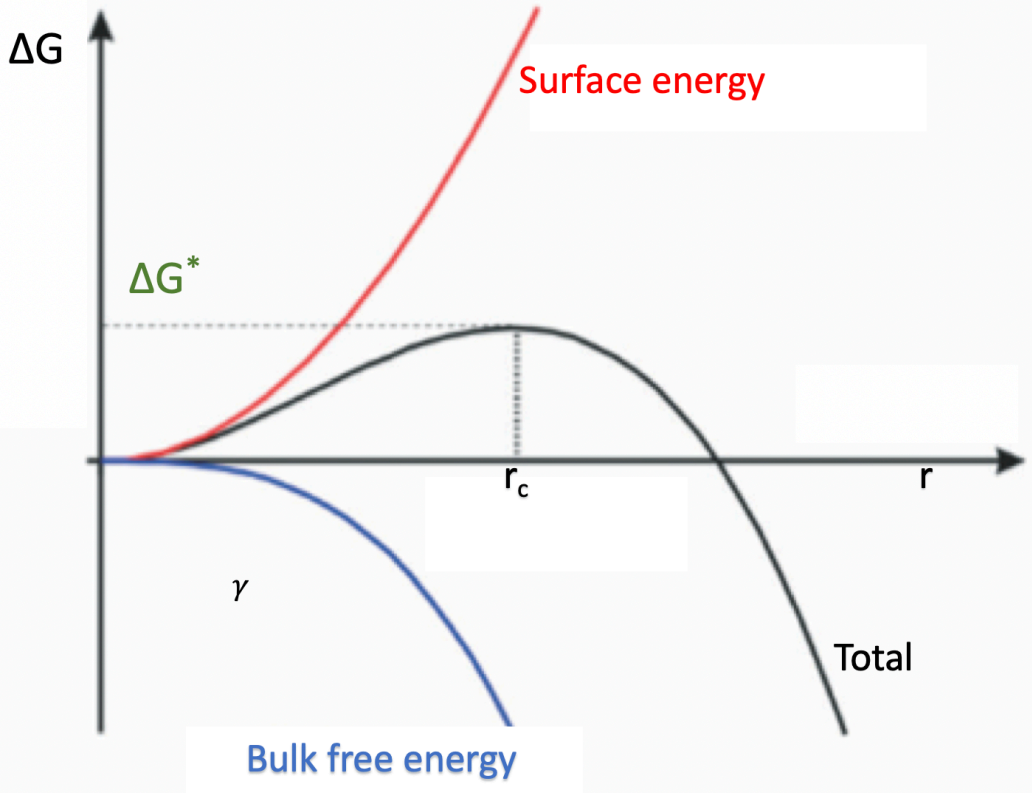

Figure 2.2: Total free energy (ΔG) as a function of cluster radius. Figure modified from Polte[54].

The rate of nucleation (J; Equation 2.2) is the quantification of how many nuclei (N) form per unit volume and time (t) is essential when considering the nucleation event[54]. In Equation 2.2, A is a pre-exponential factor that accounts for the collision frequency, γ is the surface energy, V_m is the molar volume of the nucleating material, K_b is the Boltzmann constant, T is temperature, and S is the degree of supersaturation.

$$J = \frac{dN}{dt} = A\, exp\left(\frac{16\pi\gamma^3 V_m^2}{3k_B^3 T^3 (lnS)^2}\right) \tag{2.2}$$

Heterogeneous nucleation

Heterogeneous nucleation is a process that occurs at specific nucleation sites on a solid interface of a different material. The nucleation occurs at preferential sites of the surface of already nucleated particles, air bubbles, the surface of the reactor, etc. This process lowers the activating energy of the nucleation process. Heterogeneous nucleation is part of the nanoparticle growth process. However, in the context of this work, it is only desired after burst nucleation occurs (Methods and Theory 2.1.2 - The LaMer model). If heterogeneous nucleation occurs due to impurities in the reactor, the result is uncontrolled nucleation that leads to the synthesis of nanoparticles with a broad size distribution[55].

2.1.2 The LaMer model

In 1950, LaMer *et al*. proposed the concept of the burst nucleation process (the formation of many nuclei simultaneously, followed by growth with no generation of new nuclei)[56]. Burst nucleation allows the synthesis of nanoparticles of the same size and is usually referred to as separating the nucleation and growth processes.

Figure 2.3 shows a LaMer plot where the three stages of nanoparticle formation are shown[12,54]. At the first stage, the concentration of monomer increases due to the decomposition of the precursor in question, reaching the equilibrium concentration, *Cs*. At *Cs*, although possible, homogeneous nucleation is not likely since the system needs to overcome the energy barrier for nucleation ΔG^*. At the second stage, the solute concentration increases, reaching C_{min}, the minimum concentration required for precipitation. When C_{min} is reached, ΔG^* is overcome, and homogeneous nucleation occurs. The nucleation events cause the concentration of monomers to decrease. When it is below C_{min}, no more homogeneous nucleation can occur, and the third stage of nanoparticle growth process starts. The growth process continues until the solute concentration reaches C_s, which is the concentration where the systems reach equilibrium.

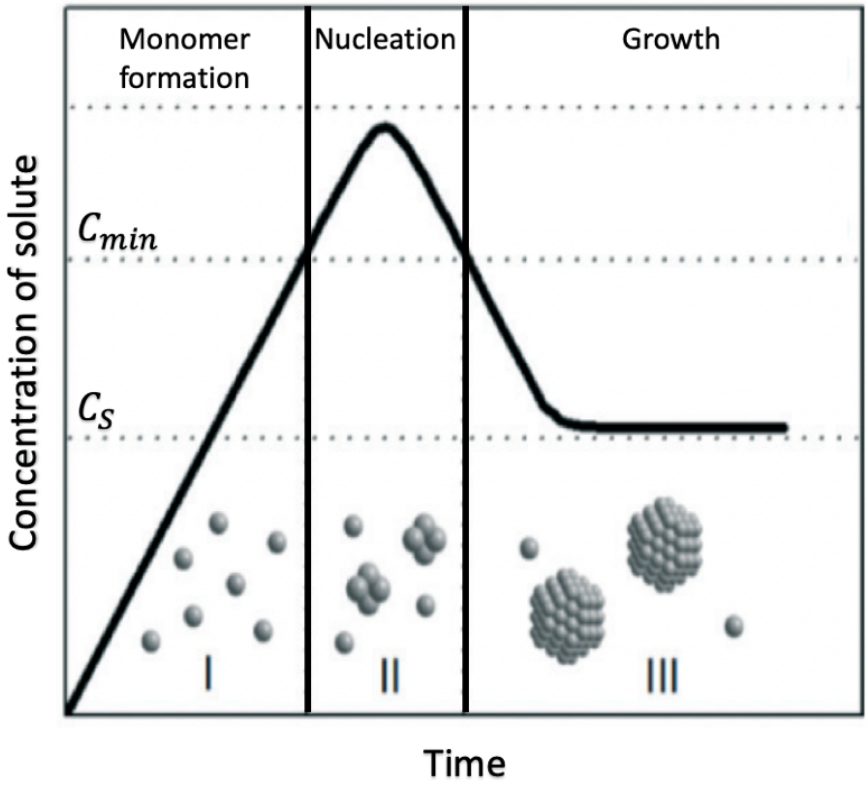

Figure 2.3: LaMer plot describing the monomer formation, nucleation, and growth stages of nanoparticle synthesis. Figure modified from Polte[54].

2.1.3 Growth

The nanoparticle growth process in solution can be controlled by either diffusion or surface processes. In diffusion-controlled processes, the monomers of the growth species are supplied to the growth surface. In surface processes, the monomer forms by a chemical reaction on the particle's surface. When only one nucleation event occurs, nanoparticles with narrow size distribution form from diffusion-limited growth[12,55]. The Reiss growth by diffusion model[57] predicts that in diffusional growth, small particles will grow faster than large particles. Small nanoparticles grow faster than large ones because they have higher intrinsic surface activity and lower coverage of ligand on the surface that affects the fraction and reactivity of the free surface sites[58]. The process leads to the narrowing of the size distribution of the system, called *size focusing*[54,55].

2.1.4 Ostwald ripening and coalescence

When the concentration of monomers in the solution approaches its equilibrium concentration (*Cs line* from Figure 2.3), Ostwald ripening and coalescence can still lead to nanoparticle growth (Figure 2.4). Oswald ripening happens when a solution has particles of different sizes, where particle 1 >> particle 2. The smaller particle is less thermodynamic stable than the larger one. Therefore, they dissolve. The dissolution of the smallest particles adds monomers to the solution that gets deposited and stabilized onto the larger particle. In other words, the larger particles grow at the expense of the smaller ones. The process only stops when the smaller particles are entirely dissolved[59].

Coalesce occurs when two particles meet, fuse, and form a larger particle. Here, a dynamic exchange is not observed, as opposed to the Ostwald ripening[60]. The driving force behind the process is a reduction in the surface area.

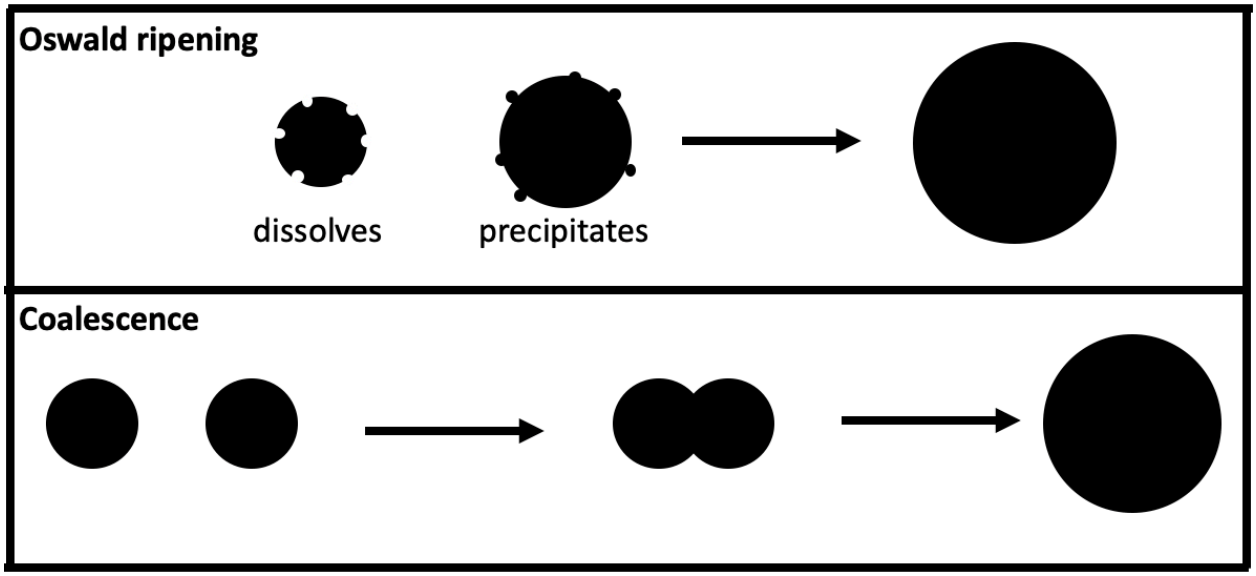

Figure 2.4: Illustration of Ostwald ripening and coalescence processes of nanoparticle growth.

2.2 Nanoparticle stabilization in colloidal synthesis

Solution-phase synthesis of nanoparticles requires stabilizing agents, capping agents, or surfactants. Uncoated nanoparticles have high surface energy when compared to their corresponding bulk phase. When bare nanoparticles approach each other, van der Waals forces or dipole-dipole interactions (in magnetic nanoparticles) may lead to reversible or irreversible aggregation[54]. The three types of nanoparticle stabilization in solution-phase synthesis are (i) electrostatic, (ii) steric, and (iii) electrosteric stabilization.

(i) Electrostatic stabilization take place in aqueous systems where the nanoparticles may become charged and hydrated. Ions present in the solution get adsorbed to the particle's surface, forming a charged layer while solvated counterions surround the particle. This phenomenon gives rise to a charge-neutral electrical double layer with a higher repulsion force than the van der Waals attractive force. Figure 2.5A shows a graphical representation of the interaction potential energy of particles as a function their distance. The potential energy of the particles (Figure 2.5A – solid line) is calculated by summing the van der Waals attractive forces and the repulsive electrical forces (Figure 2.5A – dashed lines). The *primary minimum* corresponds to the distance where the nanoparticles will undergo irreversible flocculation[12]. The system will not undergo irreversible flocculation unless the *energy barrier* is reached. At the *secondary minimum* of the solid line in Figure 2.5A, the nanoparticles are in a reversible flocculated state[12]. Notably, the electrostatic stabilization is also a function of the concentration of ions in the suspension and is only valid for diluted systems[12].

(ii) Steric stabilization refers to the use of organic molecules or polymers (Figure 2.5B) to compensate for the van der Waals attractive forces. These molecules have functional groups that coordinate to the nanoparticle's surface. The functional group is bonded to a bulky carbon chain that provides spatial isolation from nanoparticle to nanoparticle. Steric stabilization is based on the entropic- and osmotic effects. The entropic effect is due to the reduction in entropy of the molecule's chains in the interparticle region. When the particles are apart, the free energy of the system decreases. The osmotic effect comes from the increase of the concentration of the surfactant in the interparticle region[12,61], causing a flow of the dispersion medium from the areas of low- to areas of high solute concentration. The process drives the nanoparticles away from each other. In addition, the concentration of surfactant added is also a parameter for avoiding aggregation of the nanoparticles[62,63]. The nanoparticles will aggregate through the bridging flocculation process if the surfactant concentration is too low. If too much surfactant is used, the nanoparticles could aggregate due to depletion flocculation[62,63]. Steric stabilization is not dependent on the concentration nor the presence of electrolytes in the solution[61].

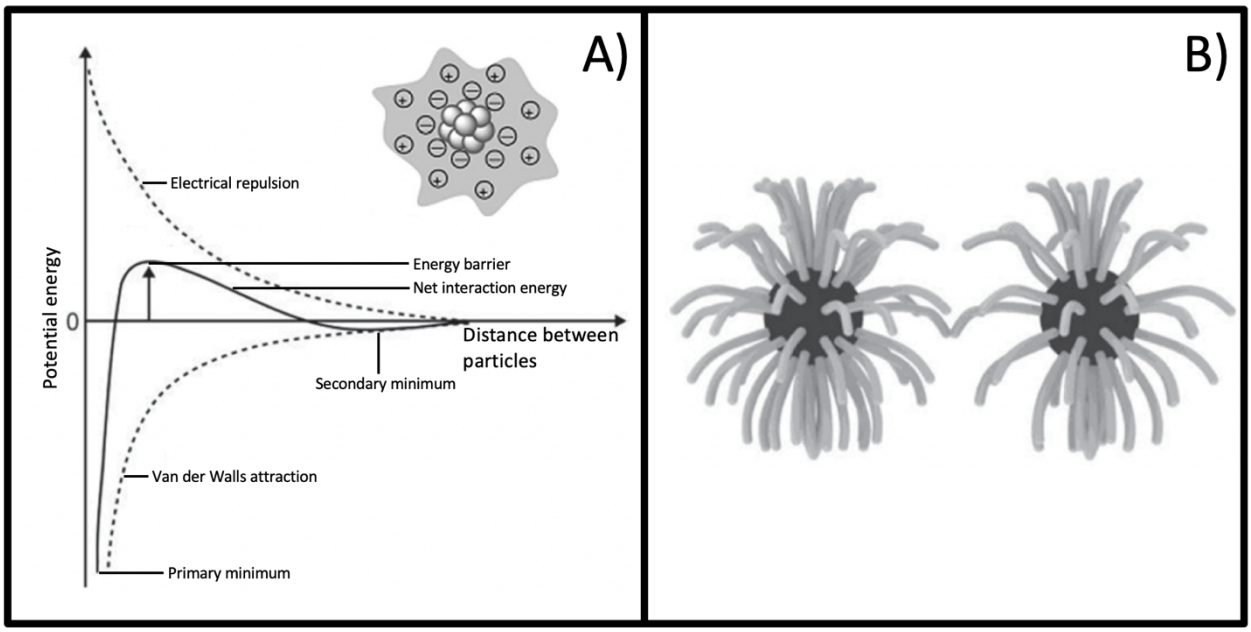

Figure 2.5: Nanoparticle stabilization in colloidal synthesis. A) Electrostatic and B) steric stabilization of nanoparticles in solution-phase systems. Figure modified from Xiong[12].

2.3 The hot-injection-, heat-up by reflux-, and hydrothermal/solvothermal synthesis methods

The hot-injection method (Figure 2.6A) exploits the burst nucleation concept. A concentrated precursor solution gets injected into a pre-heated solvent containing a stabilizing agent. The injection leads to supersaturation, thus to burst-nucleation. The stabilizing agent binds to the nanoparticle surface, preventing agglomeration and controlling their growth. The nanoparticles synthesized by hot-injection usually show a narrow size distribution (~ 10 % in diameter variation for spherical nanoparticles)[55,64,65].

The heat-up method was developed as a scalable alternative to the hot-injection method. In the heat-up method (Figure 2.6B), the precursors and stabilizing agents are dissolved and mixed at a temperature where the reagents are stable. The reaction mixture is then heated to the temperature where nucleation and growth occurs[64,66]. The mechanisms for the nucleation and growth of nanoparticles are similar to that in the hot-injection method[66].

In the hydrothermal and solvothermal methods, the reaction that produces the nanoparticles is performed in a sealed container (Figure 2.6C). Therefore, the solvents can be heated to a temperature above their boiling points, thus increasing to the autogenous pressure in the container. This is exemplified for some commonly used solvents in Figure 2.7. The increase in pressure can boost the solubility and reactivity of the precursors[12]. In addition, the size of the nanoparticles can be controlled by choice of solvent, pressure, reaction temperature, time, heating rate, and amount of surfactant. When applying the hydrothermal/solvothermal methods, one has to avoid overcoming the temperature- and pressure limit of the system. Furthermore, the expansion coefficient of the solvent has to be considered in order to decide on the degree of filling of the autoclave (Figure 2.8). If either the pressure limit is exceeded or the solvent expands over the physical limits of the autoclave, the system could leak or even explode. In syntheses where a rapid heating rate is critical, microwave-assisted solvothermal methods can be used. When polar solvents are used with the aid of a microwave assistant reactor, the system can be heated to the desired temperature in a shorter time[67]. The solvothermal approach allows the synthesis of different types of materials: metallic, metal-oxides, chalcogenides nanoparticles, and nanostructures[68].

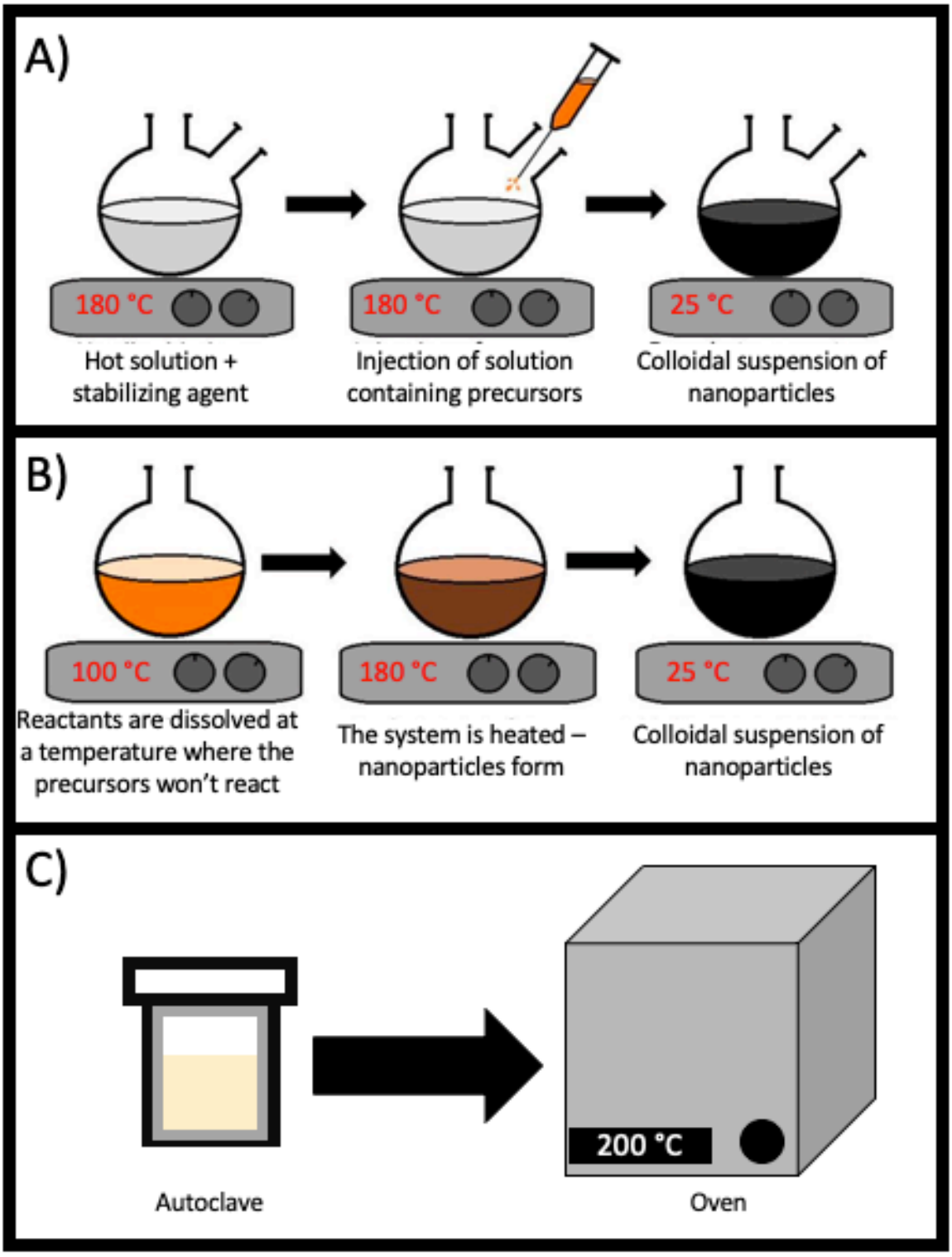

Figure 2.6: Graphical representation of nanoparticle synthesis. A) The hot-injection method; B) The heat-up method; C) The hydrothermal/solvothermal method. Figure modified from Jensen[69].

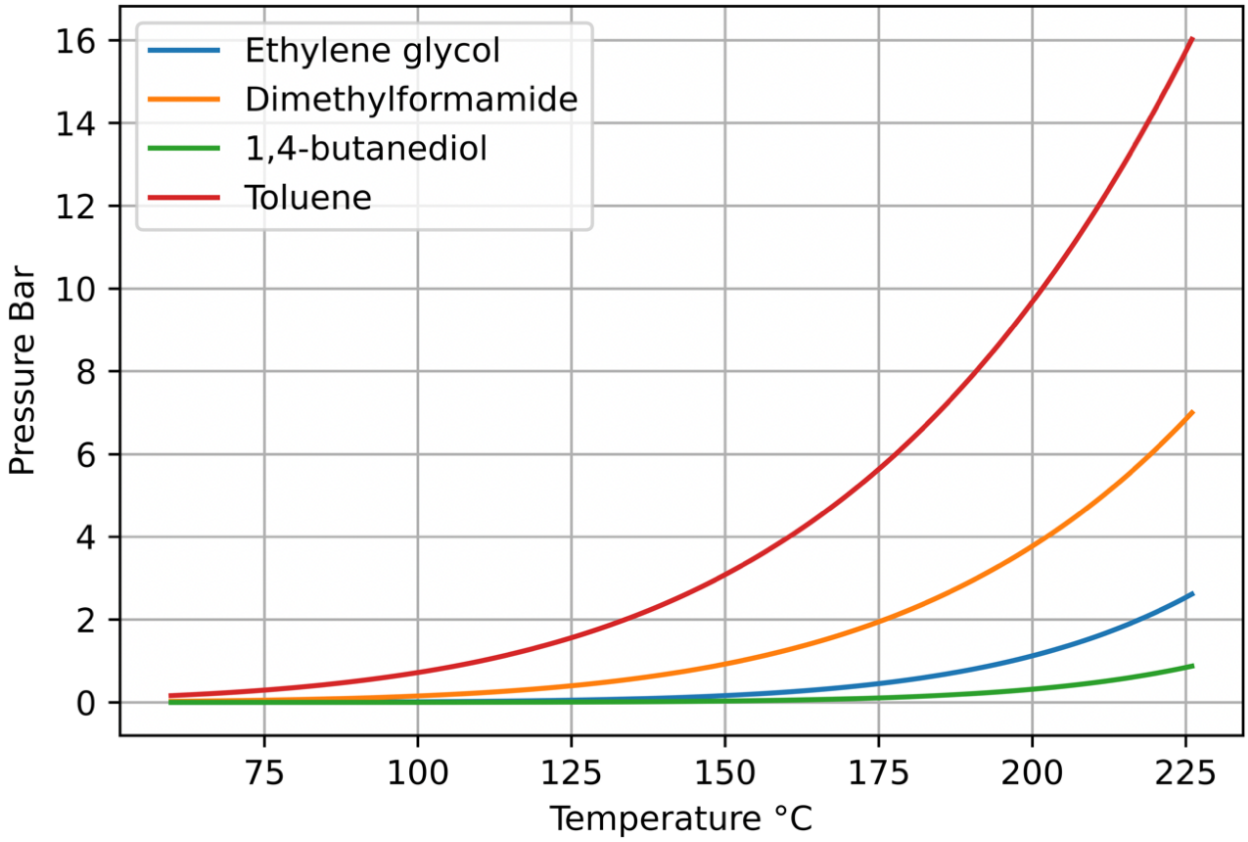

Figure 2.7: Graph showing the effect of pressure as a function of temperature for common solvents used for nanoparticle synthesis. The graph was prepared using the Clausius-Clapeyron equation[70] and the ΔH_{vap} was taken from Rumble[71].

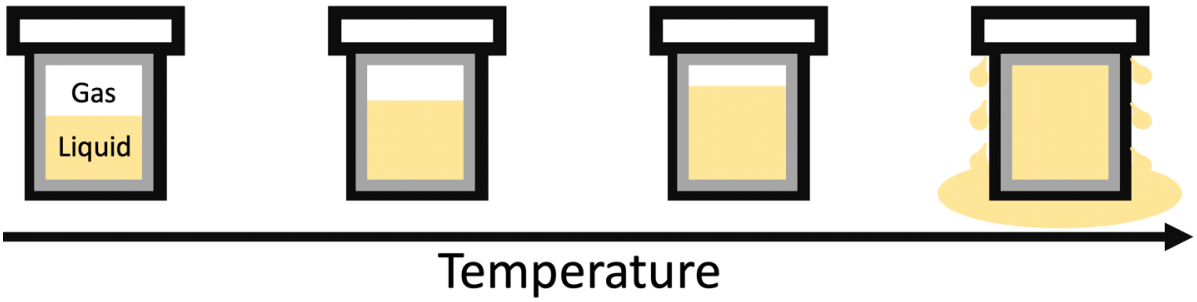

Figure 2.8: Schematic drawing of the development of liquid and gas phases in the autoclave as a function of temperature. At high temperature, the liquid phase reached the physical limit of the autoclave, causing the system to leak.

2.4 Synthesis using the solution-phase route for metallic nanoparticles

Metallic nanoparticles can be made through the solution phases by exploiting the chemical reduction- or thermal decomposition methods.

Chemical reduction (Equation 2.3) is a traditional method for synthesizing metallic nanoparticles. For chemical reduction to occur using the solution-phase method, at least four essential components must be present in the solution; the solvent, the metal precursor, the reducing agent, and the stabilizing agent. When chemical reduction is used, the size of the nanoparticles can be controlled by the concentration of stabilizing agents, reduction agents, and metal precursors, together with the solvent, reaction temperature, and time[53].

$$nM^{2+} + 2ne^{-} + stabilizing\ agent \rightarrow M^{0}\ nanoparticle \quad (2.3)$$

Thermal decomposition is also a method used in solution-phase routes for metallic nanoparticles. It has similar prerequisites as the chemical reduction route, but a reducing agent is not required. In this case, the metal is not oxidized but complexed by a chelating agent. The nanoparticles are produced by the thermal decomposition of the chelating agent in a solution. Thermal decomposition allows for mild reaction conditions, liberating free metal atoms in solution[72]. The method produces nanoparticles with a narrow size distribution as the mild reaction conditions facilitate control of the nucleation step.

The solvent: The solvent is the medium that facilitates the reaction in a chemical system. Switching solvents, for example, could alter the solubility of the precursors and stabilizing agents. That would alter the produced nanoparticle size and size distribution[73]. Furthermore, the concentration of precursors and stabilizing agents in the solvent may be used to tune the size and morphology of the nanoparticles[74].

The precursor: The precursor is a compound used to produce the nanoparticles through a chemical reaction. In the context of metal nanoparticles, the precursor is the source of the metal in question. There are different precursors of the same metal, and the choice of precursor affects the system's reactivity. It is shown that precursors with relative intermediate reactivity give a better yield and produce nanoparticles with a narrower size distribution[66].

The reducing agent: The reducing agent donates electrons to the metal ion, leading to the formation of metal atoms from which the metallic nanoparticles will form. In some syntheses, reduction agents such as $NaBH_4$, H_2, CO_2, amides, and amines are added to the solution. The surfactant, the solvent, or a combination of the surfactant and the solvent, could act as a reduction agent in other syntheses. Polyalcohols are examples of solvents that also act as a reducing agent.

The stabilizing agent: The stabilizing agent is used to prevent aggregation of the metal nanoparticles. Stabilizing agents are surfactants or polymers that deposit on the nanoparticles' surface. They are molecules that contain at least one hydrophobic chain and one hydrophilic group. The concentration, size of hydrophobic chain, type of hydrophilic group, and attachment preferences to certain crystal planes can determine the particle size and morphology[12].

2.4.1 The polyol method

The polyol method is a synthesis method exploiting the chemical reduction route[75]. The method uses a polyalcohol, a molecule that contains at least two alcohol groups (-OH), as both solvent and reducing agent (Figure 2.9). First, the polyol dissolves one or more metal precursors, then the polyol acts as a reducing agent[76], transforming the ions from the precursor into metal. A stabilizing agent is usually added to the solution to avoid aggregation and control the growth of the nanoparticles. The polyol route is an extensively used approach for synthesizing nanoparticles that vary in size and morphology[73]. Their solubility is comparable to water for many polar precursors. They can have relatively high boiling points, allowing for synthesis at up to 320 °C using atmospheric pressure.

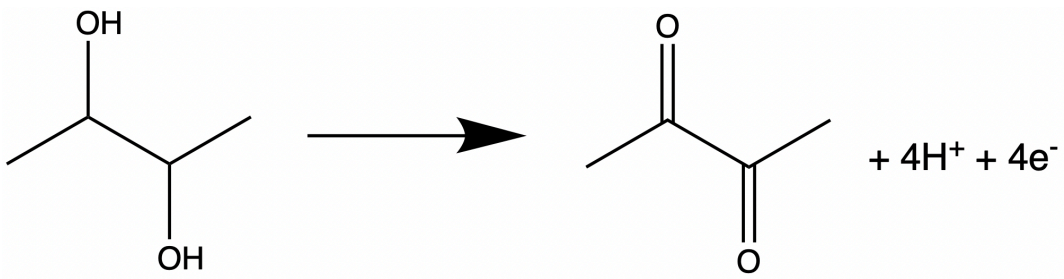

Figure 2.9: Example of an oxidation reaction of the polyalcohol 2,3-butanediol into 2,3-butanedione.

2.5 Bimetallic nanoparticles

Bimetallic nanoparticles are classified into mixed alloyed, core-shell segregated, and subcluster segregated nanoparticles (Figure 2.10). Mixed alloy nanoparticles can be in solid solution or intermetallic configurations; core-shell nanoparticles (A@B) have a core of one metal (A) clustered by a shell of another (B). Subcluster segregated nanoparticles are made of A and B subclusters that may share an interface.

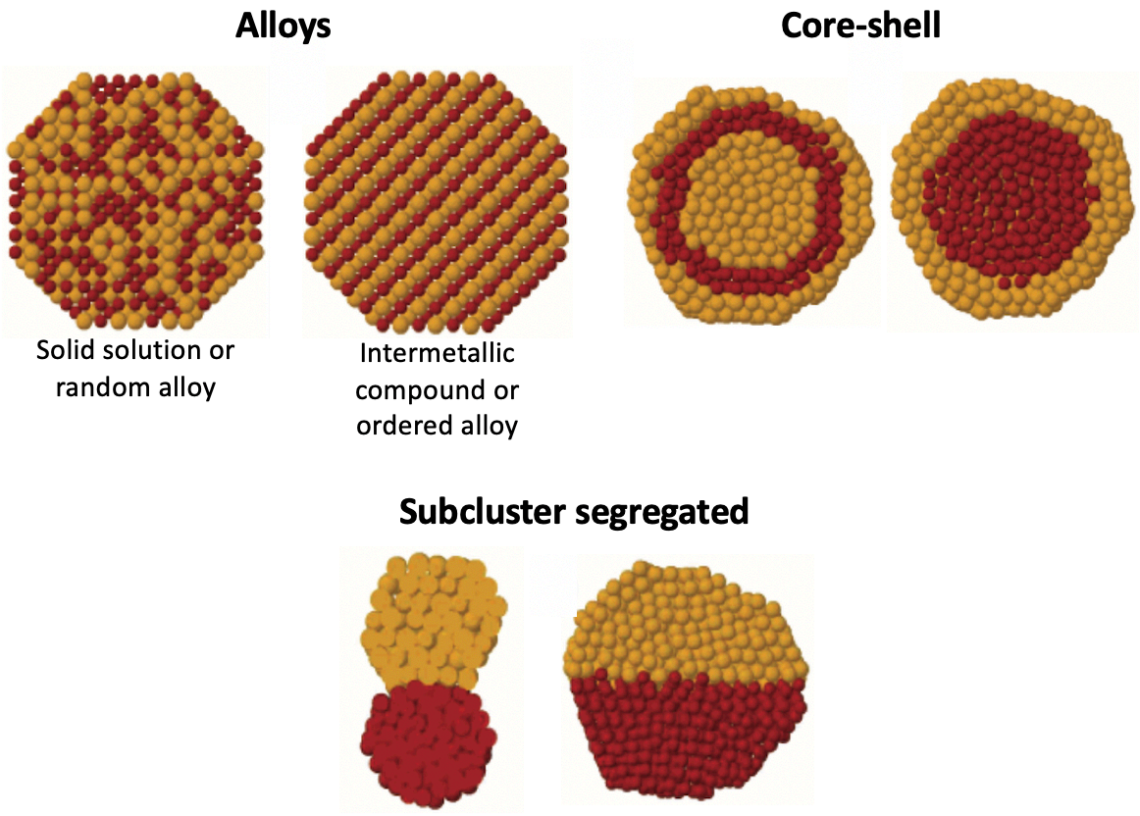

Figure 2.10: Main configuration of bimetallic nanoparticles. Figure modified from Ferrando[77].

In thermodynamically stable systems, six factors influence the degree of segregation or mixing and atomic ordering in bimetallic nanoparticles[77]:

i. The relative strength of bonds: Mixing is observed when A-B bonds are stronger than A-A and B-B. The element with the strongest homonuclear bonding in core-shells tends to be at the core.
ii. Surface energies of the metals: The metal with the lowest surface energy tends to segregate to the nanoparticle's surface.
iii. The relative atomic diameter: Smaller elements tend to segregate to the nanoparticle's core.

iv. Charge transfer: Electron transfer between the metals A and B favors elemental mixing in the nanoparticle.
v. Type of stabilizing ligand: The metal that makes the strongest bond to the functional groups of the surfactant tends to be on the surface of the nanoparticle.
vi. Magnetic or electronic effects: The electronic shell structure or electron spin interactions stabilized nanoparticles with specific sizes, compositions, and mixing patterns.
vii. Certain systems are at a kinetically stable configuration upon synthesis, but once enough energy is added to overcome the kinetic barrier, a phase transition occurs, leading to the formation of the thermodynamically stable phase[51,52,78,79].

2.6 Solution phase co-reduction route for the synthesis of bimetallic nanoparticles

Bimetallic nanoparticles can also be produced using the solution phase by exploiting the chemical reduction or the thermal decomposition methods (Methods and Theory 2.4). However, the presence of a second component increases the complexity of the synthesis. In bimetallic nanoparticle synthesis, the relative reaction kinetics of the precursor is a critical parameter as it dictates the final configuration of the nanoparticle[29].

Co-reduction refers to the simultaneous or successive reduction of precursors that contain two different metals[80,81]. In this case, the redox potential of the metals determines the structure of the nanoparticles. When there is a significant difference in redox potential, $\Delta E° \geq 0.20\,V$[82], segregated nanoparticles form. When the difference is small, solid solution nanoparticles are synthesized.

In conditions where there is a significant difference in reduction potentials between the metal precursors, the slowest reacting metal will deposit on the surface of the faster-reacting metal. Sub-cluster segregation occurs when the second metal favors deposition on a specific facet of the first metal.

Variation of the molar ratio of the metal precursors is one strategy to synchronize the reduction rates of metal ions with a significant gap in reduction potential[80,81]. Reducing agents, film flexibility, and surfactants also influence the nanoparticles' final configuration. A synthesis expected to give an A@B core-shell configuration could make a B@A by using a surfactant that binds strongly to the metal B.

2.7 Metal-on-support catalyst preparation

Metal nanoparticles are usually supported on high surface area materials when used as catalysts. There are several reasons for this. If not supported, the particles could sinter or be transported away from the reactor in the gas stream during the catalytic process. Therefore, the catalyst has two components: 1) the metallic nanoparticles, and 2) the support material. Materials such as Al_2O_3, TiO_2, SiO_2, Nb_2O_5, and CeO_2 are commonly used as support due to their high surface area relative to their weight[83]. It is crucial to maximize the surface area of a catalyzer because catalytic processes happen on the surface of the material.

2.7.1 Wet impregnation and direct colloidal deposition of nanoparticles onto a porous support

Two common methods for deposition of nanoparticles onto support are the wet impregnation- and the direct colloidal deposition methods[84]. In the wet impregnation method (Figure 2.11A), the support is submerged in a solution containing metal precursors for the nanoparticles. The solvent is evaporated, leaving the precursor salt deposited within the pores of the support. Finally, the support is calcinated in a reducing atmosphere, often containing H_2[85], reducing the metal ions, thus forming nanoparticles. The metal loading can be adjusted by the amount of support used for deposition.

In the direct colloidal deposition method, the support is submerged in the media where the catalyst is suspended. The nanoparticles in the suspension get adsorbed into the support (Figure 2.11B). Colloidal deposition is a direct and easy method to employ. In addition, it allows for the tailoring of the nanoparticle size and composition prior to support deposition. It allows utilizing a wide range of supports — such as carbon- and oxide materials. Moreover, like in the wet-impregnation method, the metal loading can be adjusted by the amount of support used for the deposition.

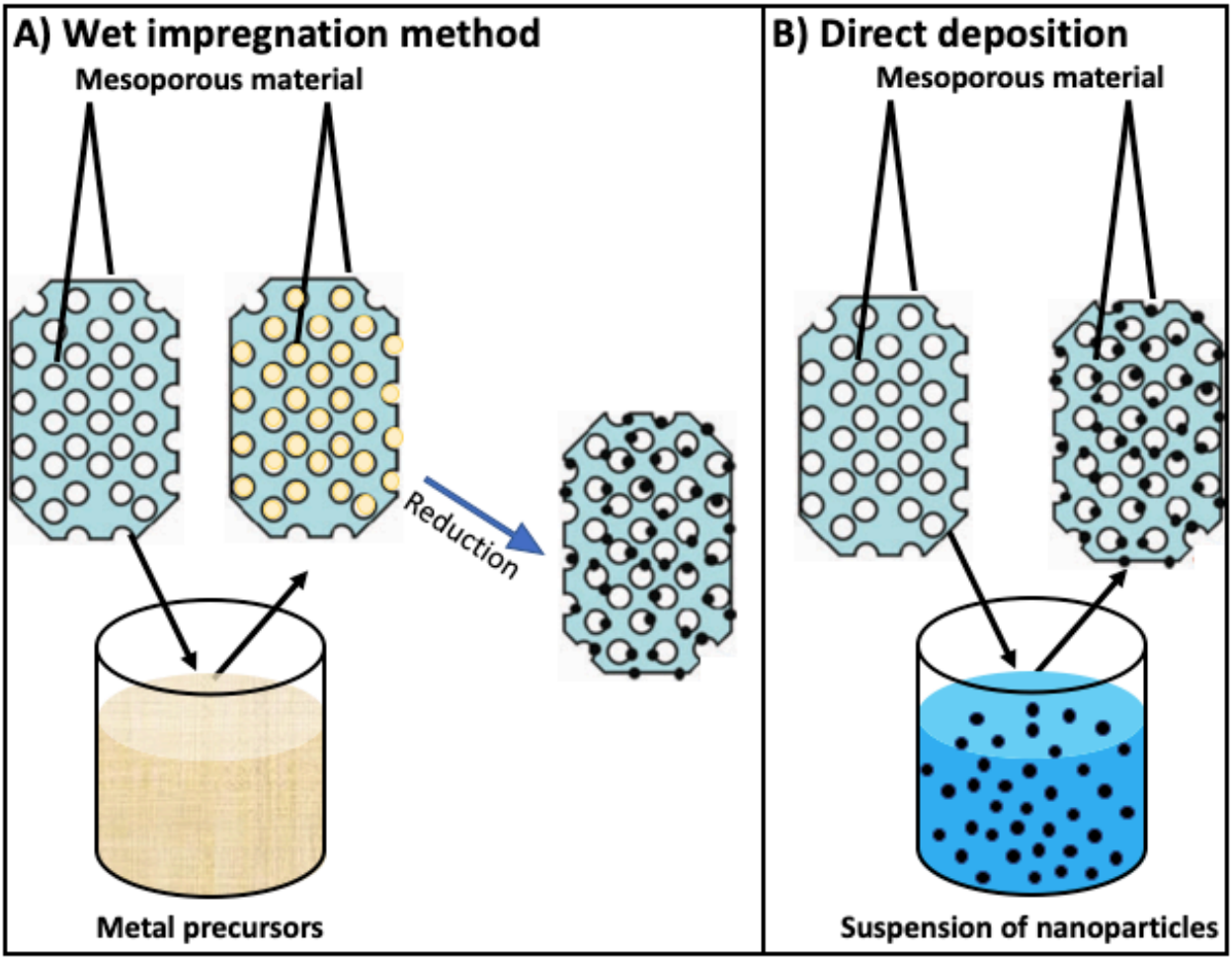

Figure 2.11: Common methods for deposition of nanoparticles onto support. A) Wet impregnation method; B) Direct colloidal deposition method. Figure modified from Linares[86].

2.7.2 Surfactant removal for catalyst activation by thermal oxidation or reduction treatment processes

Catalytic processes take place on the surface of the materials. Some nanoparticle syntheses involve the use of surfactants. Surfactants cover the nanoparticles' surface, which prevents the reactants from reaching the catalysts' active sites during the catalytic process. Therefore, the surfactant needs to be removed prior to application.

Most surfactants are either organic compounds or polymers. Thermal treatment under oxidation conditions will, therefore, convert the surfactants into CO_2 and H_2O[87,88]. In order to prevent unwanted structural changes such as sintering of the metallic nanoparticles, the treatment temperature must be chosen with caution[28]. At the same time, coke may be generated if the surfactant is not completely oxidized, which may have a negative effect on the system's catalytic properties[89]. In addition, heat treatment under oxidative atmospheres may cause the metal

nanoparticle to oxidize. To avoid oxidation of the nanoparticles, heat treatment under non-oxidative conditions is commonly employed[90]. In addition, sequential oxidation-reduction cycles[91], or the combination of oxidizing and reducing gases[92,93], are also effective strategies to prevent oxidation of the nanoparticles.

2.8 Characterization methods

2.8.1 The scanning electron microscope

The SEM is an instrument that examines microscopic structures by scanning the surface of a material with a focused electron beam. The SEM allows the detection of a range of different signals. The electron beam is generated by an electron gun and focused by a series of electromagnetic lenses (condenser- and objective lenses). In addition, the system employs electromagnetic coils that are used to steer the probe over a line and then direct the probe to the line that follows the scanned area. For a representation of the SEM column, see Figure 2.12A.

The electron beam forms the signals that create the image of the sample. Once the electron beam hits the sample, the electrons interact with the sample within an interaction zone. Consequently, various signals are created (Figure 2.12B). These signals can then be detected by different detectors. This section introduces the detectors for secondary electrons (SE), backscattered electrons (BSE), and transmitted electrons.

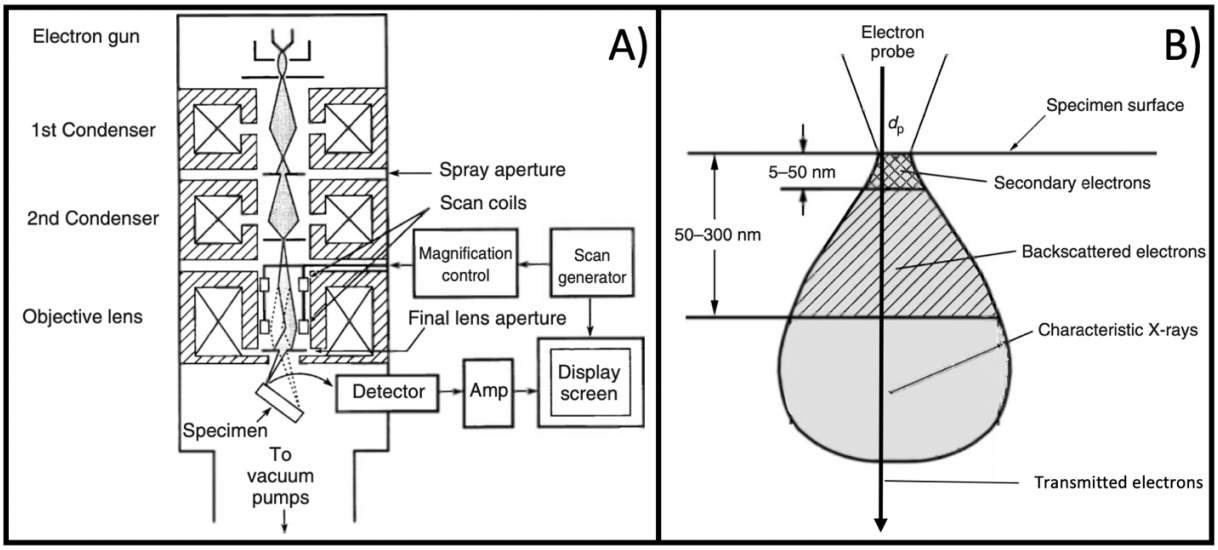

Figure 2.12: The Scanning Electron Microscope (SEM). A) Representation of the internal structure of the SEM; B) Interaction zone of electrons and signals created by the electron beam. Figure modified from Leng[94].

Secondary electrons: An SE is generated by inelastic interaction events[94] (Figure 2.13A). The electrons used for imaging originate from within 5 to 50 nm below the sample surface. The electrons can also be generated deeper in the sample, but because of their relatively low energy (50 eV), they are absorbed by the sample and never reach the detector[94]. Thus, SE imaging is surface sensitive, reflecting the sample's topography.

Backscattered electrons: Backscattered electrons are generated by elastic interaction events between the electron beam and the nuclei of the atoms in the specimen[94] (Figure 2.13B). They possess relatively high energy, keeping ~ 60-80 % of the incoming energy from the electron beam. The backscattered electrons come from a depth of 50 to 300 nm. The backscattered electron detector is especially useful when the specimen contains materials made of light (e.g. as in Al_2O_3) and relatively heavy elements (e.g. Rh and Pt). Heavier elements spread more electrons than the lighter ones because their nuclei are more positively charged. For that reason, images formed using backscattered electrons are sensitive to the atomic number Z contrast, light atoms appear darker than heavy atoms in the images.

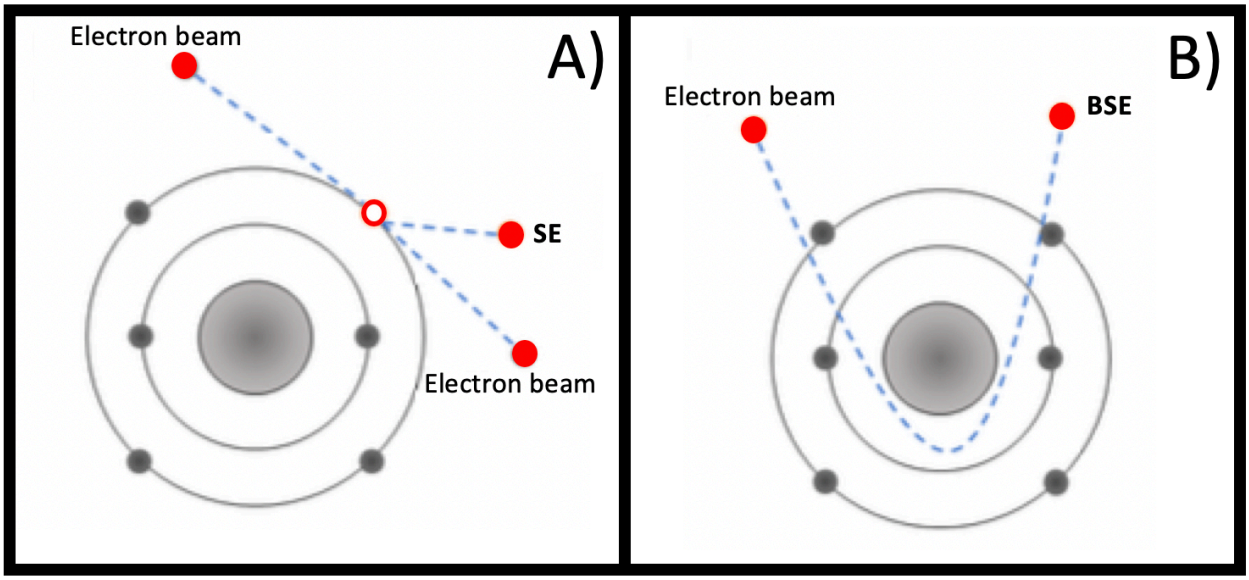

Figure 2.13: Formation of secondary- and backscattered electrons. A) Secondary electrons; B) Backscattered electrons. Figure modified from Leng and Jensen[69,94].

Transmitted electrons: Some scanning electron microscopes are also equipped with transmitted electron detectors. The formation, detection, and image information are similar to the bright-field scanning transmission microscopy (STEM; Methods and Theory 2.8.2). A key difference is that the bright-field-STEM from an SEM has lower spatial resolution compared to TEM.

2.8.2 The transmission electron microscope

Many of the principles for TEM are similar to that of SEM. Some key differences are that the TEM uses transmitted electrons (Figure 2.14B) to generate images. The TEM has higher magnification capabilities and better spatial resolution thanks to its relatively high acceleration voltage, 60 to 1000 kV, when compared to the SEM (1-30 kV)[38]. For TEM studies, the sample must be electron transparent, which means less than 100 nm thick. The generated image is a 2-D projection of a 3-D object[95].

Modern TEMs have two modes of operation for imaging; 1- conventional TEM and 2- scanning transmission electron microscopy (STEM). Additionally, the TEM has two main modes of operation for detecting the chemical composition, EDS and electron energy loss spectroscopy (EELS). This master's thesis used the STEM mode for imaging and EDS for characterizing the chemical composition of the samples.

Scanning transmission electron microscopy

In STEM, like in SEM, a finely focused electron beam is steered by electromagnetic scan coils. It directs the electron beam over a line on the sample, and once it finishes scanning that line, it directs the probe over the following line until it finishes scanning a pre-determined rectangle. The transmitted electrons are then detected as a function of the position of the sample in the x-y plane.

The two image detectors used for this master's thesis were the bright-field- and the high angular annular dark field (HAADF) detectors (Figure 2.14A). The bright-field-STEM images are formed from the coherently scattered beams. The primary forms of contrast are the mass thickness contrast, the phase contrast, and the atomic number Z contrast[95]. In this master's thesis, we used bright-field-STEM images to prepare histograms.

The HAADF-STEM is a dark field technique that uses incoherent electron scattering to form images. The image is formed by the electron beams scattering at a high angle (~ 70 to > 200 mrad)[95]. The image intensity is formed by the individual contribution of each atom and by the thickness of the sample[95]. HAADF-STEM images are useful for characterizing bimetallic nanoparticles with a large difference in Z, such as Rh (Z = 45) and Pt (Z = 78). The atomic Z contrast is proportional to Z^2. Yet, the difference in sample thickness is small throughout the nanoparticle. For that reason, the primary source of contrast will be the atomic number Z contrast.

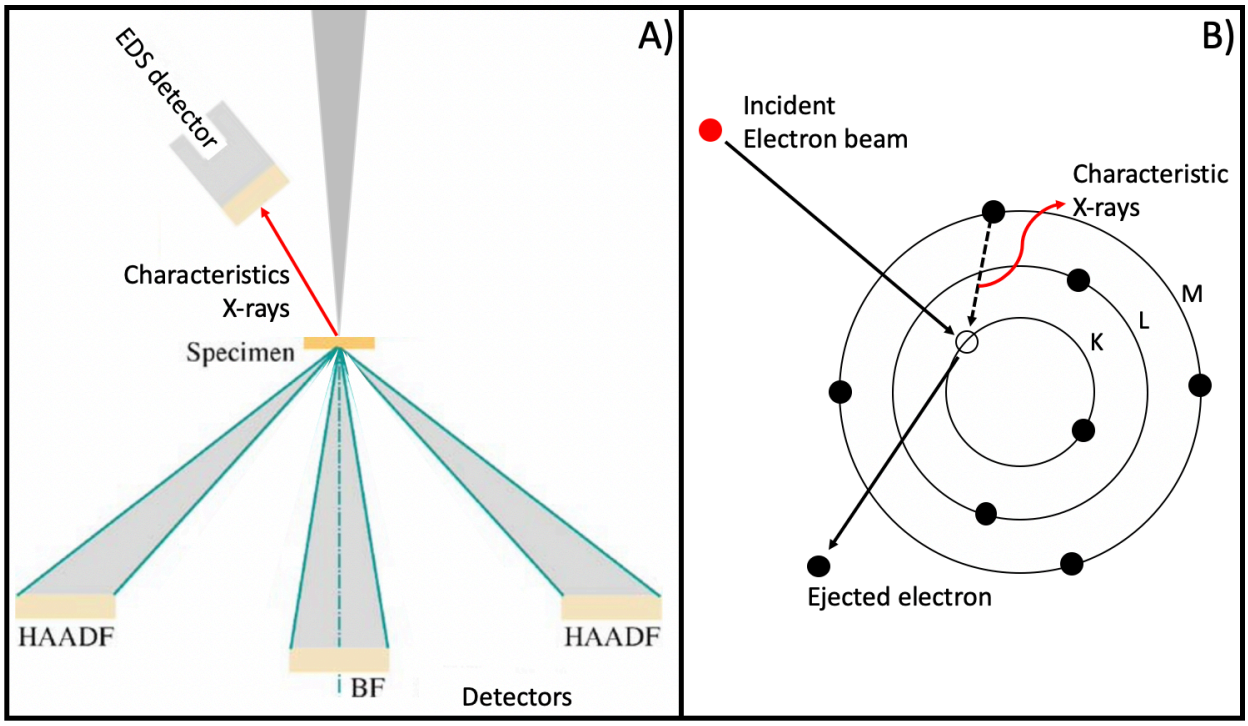

Figure 2.14: The scanning transmission electron microscope. A) Position of EDS-, bright-field-, and HAADF detectors in a TEM column; B) The principle behind the characteristic X-ray emissions detected by the EDS technique. Figure modified from Leng and Jensen[69,94].

Energy-dispersive X-ray spectroscopy

EDS is an element detection system with a typical energy resolution of 150-200 eV that can detect elements of atomic number $Z > 8$[94]. The technique is relatively easy and fast to use, as the detector collects all of the characteristic X-ray signals of the sample simultaneously.

When the incident electron beam hits the sample, atoms within the sample get ionized by the ejection of an electron from the atom's inner scale. The vacancy left by the ejected electron can be filled by an electron of a higher energy level. When the atom returns to its ground state, characteristic X-rays are emitted for each type of transition. Each element and each transition emits a characteristic X-ray. The process is depicted in Figure 2.14B.

A STEM-EDS map can be prepared using the STEM operational mode with an EDS detector. The map is obtained by scanning a selected area within the sample, pixel by pixel, several times. The EDS signal is collected with the atom's position from each scan. The image of the sample containing the elemental distribution is obtained by plotting the position as a function of the type of signal obtained on a x-y plane.

Sometimes the number of counts obtained during the measurements may not be sufficient for quantification of results. In that case, pre-filtering can be applied in order to improve the quality of the data. In addition, pre-filtering can ameliorate the quality of the elemental maps.

Beam damage

Beam damage occurs due to the inelastic collisions of the electron beam onto the sample. It may affect the structure, the chemistry, or both the structure and the chemistry of the material. Beam damage is a function of the electron dose or the charge density (C m^{-2}) that the sample is irradiated with[95]. The electron dose is a function of the exposure time of the sample, the magnification, and the beam current[96].

In metallic nanoparticles, the primary source of damage is knock-on damage[95]. This process occurs because the electron beam can displace atoms out of their atomic site, creating a vacancy and an interstitial, also called a Frankel pair. Vacancies caused by displacement damage are critical during *in situ* experiments of bimetallic nanoparticles. They can speed up diffusional transformations by enhancing the diffusion processes in systems where atomic diffusion occurs[95]. Beam damage may be identified by recording images of the same area before and after a measurement and then by comparing the contrast of the material under the same imaging conditions.

In situ TEM

One of the exciting developments within the TEM field is its application for *in situ* measurements. In routine TEM measurements, the sample is observed in UHV. In contrast, *in situ* experiments enable imaging of a sample while applying external stimuli, such as temperature and gas atmosphere[95].

Figure 2.15A illustrates the Protochips® *in situ* TEM solution. The system is an add-on to the TEM column. The Protochips® Fusion consists of a computer system, electronic controllers, and a TEM sampler holder (Figure 2.15B) that allows *in situ* measurement in UHV at temperatures up to 1000 °C. The Protochips® Atmosphere system consists of a computer system, electronic controllers, a gas mixing apparatus, and a TEM sampler holder (Figure 2.15C). The atmosphere system supports *in situ* measurements at temperatures up to 1000 °C and gas pressures up to 1 ATM.

In situ TEM is a powerful tool for studying bimetallic nanoparticles in conditions similar to where they are employed[97]. For instance, as-synthesized bimetallic nanoparticles might not be thermodynamically stable at the temperature and atmospheric conditions in which they are intended as catalysts (Methods and Theory 2.5 and 2.6).

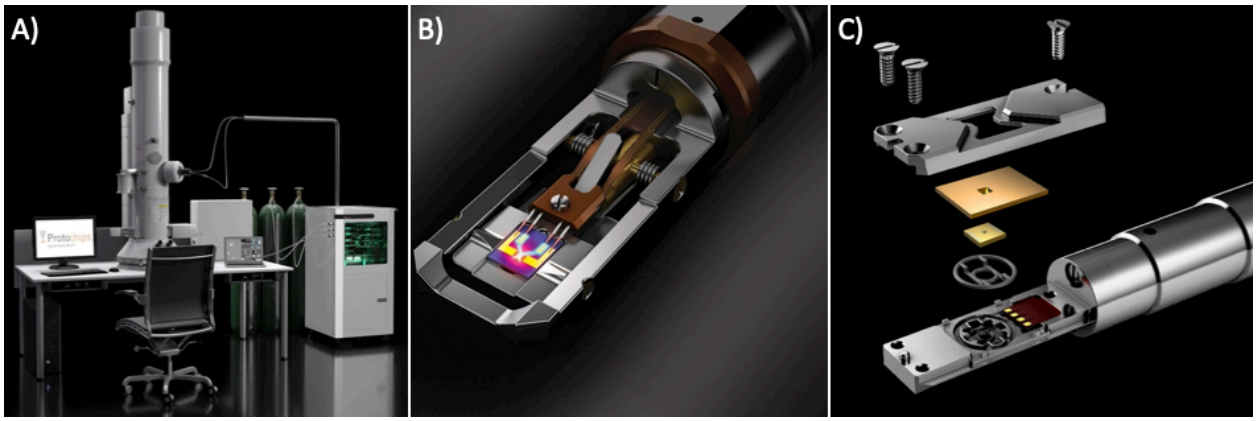

Figure 2.15: *In situ* STEM equipment. A) Illustration of a TEM column equipped with a Protochips® Atmosphere for in situ measurements in up to 1 ATM and temperatures up to 1000 °C; B) Illustration of the TEM holder for the Protochips® Atmosphere system; C) Illustration of the TEM holder for the Protochips® Fusion system, that enable TEM measurements at temperatures up to 1000 °C in UHV. Images modified from Protoships[98].

Operando TEM

Operando TEM uses the same equipment as *in situ* TEM (Protochips® Atmosphere system), but while characterizing dynamic structural changes in realistic conditions, for instance, it simultaneously measures the catalytic activity and selectivity. In *operando* experiments of a model catalyst, the exhaust outlet of the Atmosphere TEM holder is connected to a mass spectrometer.

2.8.3 Powder X-ray diffraction

PXRD is used to determine how the atoms of crystalline materials are arranged. The technique is based on the constructive interference of monochromatic waves when diffracting on a periodic structure (Figure 2.16). For constructive interference to occur, at least two incident beams with wavelength λ are reflected at a crystal structure: the first at the surface, the second after traveling a distance *d* (*PQ*). Constructive interference occurs when the waves' incidence-

and scattering angles (θ) are the same, and the path difference ($SQ + QT$) of the incident waves λ is a integer n (Equation 2.4).

$$n\lambda = 2dsin\theta \tag{2.4}$$

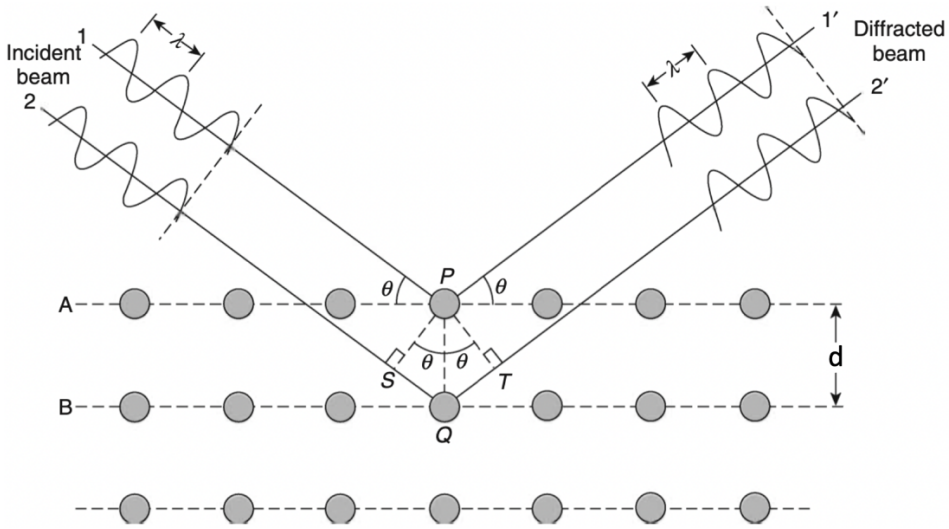

Figure 2.16: Representation of the diffraction of a monochromatic beam by a crystal structure. A and B represent the crystal planes, λ the wavelength, PQ = d the distance between the crystal planes, SQ + QT the path difference of the incident waves λ. Constructive interference occurs when SQ + QT is an integer value n of λ (Equation 2.4). Images taken from Leng[94].

The powder X-ray diffractogram provides information about phases present in the sample and nanoparticle size. It enables calculation of the unit cell size of the material. In addition, the method is used to refine or determine new crystal structures. The information may be extracted using direct- or refinement methods. This master's thesis uses the Rietveld method[99] to refine a known model structure against the diffractogram of the nanoparticles. The goal of the refinement is to extract precise unit cell size parameters. The refinement compares a theoretically generated diffractogram with the obtained diffractogram and minimizes the differences in between them by using the expression in Equation 2.5, where y_i^{calc} is the calculated profile at point i, y_i^{obs} is the observed data at point i, c is the scale factor ($y^{calc}=cy^{obs}$), and W_i is the statistical weight.

$$M = \sum_i W_i \left(y_i^{obs} - \frac{1}{c} y_i^{calc}\right)^2 \tag{2.5}$$

The quality of the Rietveld refinement is evaluated by the weighted profile residual factor (R_{wp}; Equation 2.6), and by analyzing the difference plot, which demonstrates the difference between the observed- and calculated data. A low R_{wp} value indicates that there was a good fit. However, the R_{wp} factor can omit parts of the diffractogram. Visual inspection of the difference plot is, therefore, important for determining the quality of the refinement.

$$R_{wp} = \sqrt{\frac{\sum_i W_i\left(y_i^{obs} - \frac{1}{c}y_i^{calc}\right)^2}{\sum_i W_i y_i^{obs^2}}} * 100 \quad (2.6)$$

Vegard's law

In bimetallic alloys in the solid solution configuration, PXRD can be used to determine the chemical composition of the sample[100]. According to Vegard's law, the lattice parameters of a solid solution bimetallic alloy is approximately the weighted mean of the two metals (Equation 2.7). In Equation 2.7, a_{12} is the lattice parameter of the solid solution alloy, a_1 and a_2 are the lattice parameters of metals 1 and 2, respectively; and x is the mole fraction of the metal 2 in the sample. Vegard's law is only applicable if the end members have the same crystal structure type. Furthermore, the prerequisites for the formation of a solid solution alloy according to the Hume-Rothery rules are: the metals need to have the same crystal structure, the difference in atomic radius should not be larger than 15 %, and the difference in electronegativity cannot be too large[101]. Complete solubility usually occurs when the solute and the solvent have the same valency.

$$x = \frac{a_{12} - a_1}{a_2 - a_1} \quad (2.7)$$

3 Experimental

3.1 Chemicals

Table 3.1 presents a list of the chemicals and reagents used to synthesize nanoparticles and for the washing-and redispersion procedures.

Table 3.1: List of chemicals and reagents used in this master´s thesis. CAS, Chemical Abstracts Service.

Chemical name	CAS number	Abbreviation	Chemical formula	Molar mass [g/mol]	Supplier	Purity [%]
Platinum(II) acetylacetonate	15170-57-7	$Pt(acac)_2$	$Pt(C_5H_7O_2)_2$	393.29	Sigma Aldrich	97
Rhodium(III) acetylacetonate	14284-92-5	$Rh(acac)_3$	$Rh(C_5H_7O_2)_3$	400.23	Sigma Aldrich	97
Palladium(II) acetylacetonate	14024-61-4	$Pd(acac)_2$	$Pd(C_5H_7O_2)_2$	304.64	Sigma Aldrich	99
Polyvinylpyrrolidone	9003-39-8	PVP	$(C_6H_9NO)_n$	111.14[2] (10 000)[3]	Sigma Aldrich	-
Oleylamine	112-90-3	OAm	$C_{18}H_{37}N$	267.49	Sigma Aldrich	70
Hexane	110-54-3	-	C_6H_{14}	86.18	Sigma Aldrich	95
Toluene	108-88-3	-	C_7H_8	92.14	Sigma Aldrich	99.8
Trioctylphosphine	4731-53-7	TOP	$C_{24}H_{51}P$	370.64	Sigma Aldrich	90
Formaldehyde solution[4]	50-00-0	-	CH_2O	30.03	Sigma Aldrich	-
Ethylene glycol	107-21-1	EG	$HO(CH_2)_2OH$	62.07	Sigma Aldrich	99.8
1,4-Butanediol	110-63-4	1,4-BD	$HO(CH_2)_4OH$	90.12	Sigma Aldrich	99
Argon	-	-	Ar	39.95	Praxair	99.999
Acetone	67-64-1	-	CH_3COCH_3	58.08	VWR	-
Methanol	67-56-1	Met-OH	CH_3OH	32.04	VWR	-
Ethanol	64-17-5	Et-OH	CH_3CH_2OH	46.07	VWR	-
Boehmite	1318-23-6	-	AlOOH	59.99	Sasol	-
Synthetic air	-	-	-	-	Praxair	99.999
Isopropanol	67-63-0	-	$(CH_3)_2CHOH$	60.1	VWR	-

[2] Monomer
[3] Average mol. weight
[4] 37 wt. % in water, containing 15 % methanol as stabilizer to prevent polymerization.

3.2 Autoclave method

For the synthesis, a volumetric pipette, a scale, a magnetic stir bar, a Radleys Carousel Tech hot plate, a Termaks TS 8056 oven, a 25 mL autoclave Teflon® insert, and a steel autoclave body were used. The synthesis was prepared by dissolving 0.040 mmol of metal precursor ($M(acac)_x$) at room temperature under stirring in a Teflon® insert containing 5 mL toluene. The surfactants, a range of 0.004 to 0.04 mL oleylamine or a mixture of 0.02 oleylamine and 0.010 to 0.018 mL trioctylphosphine, were added to the insert. The solution was then stirred for 10 minutes. Afterward, 0.025 mL formaldehyde solution was added to the Teflon® insert and stirred for 10 minutes at room temperature. The insert was added to the autoclave, and the system was sealed. The autoclave was added to the oven and heated to the target temperature of 100 to 130 °C. The oven stayed at the target temperature for 8 hours, and then it cooled down to room temperature with no external input. For an image of the equipment used for the autoclave synthesis, see Figure 3.1.

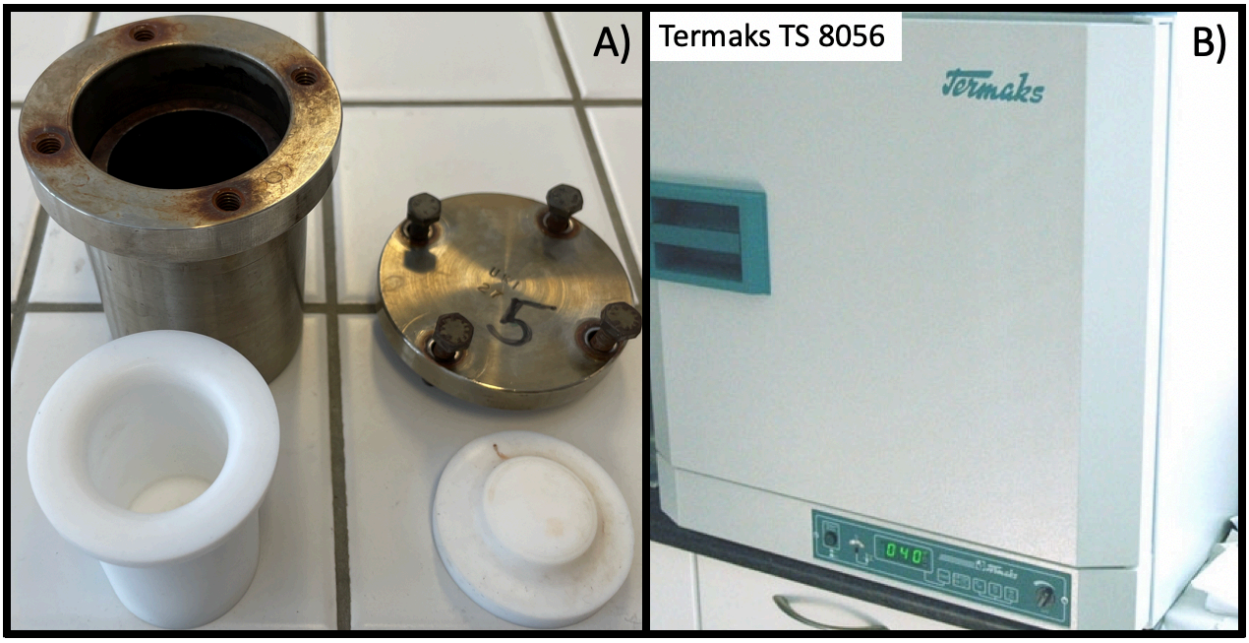

Figure 3.1: Equipment used for autoclave method. A) Steel autoclave (top) and Teflon® body (bottom); B) Termaks TS 8056 oven[102].

For washing the nanoparticles, 15 mL VWR 12.5K max polypropylene centrifuge tubes were used. The nanoparticles were washed by transferring 2.5 mL of the prepared nanoparticle suspension into a centrifuge tube with 7.5 mL of ethanol. The tube was vigorously shaken for a few seconds, followed by centrifugation at 9500 rpm for 5 minutes. After centrifugation, the supernatant was discarded. The second step was to add 0.5 mL of hexane to the centrifuge tube,

followed by 5 mL of ethanol. The centrifuge tube was vigorously shaken for a few seconds, sonicated for one minute, and centrifuged at 9500 rpm for 5 minutes. After centrifugation, the supernatant was discarded, and the second step was repeated. The nanoparticles were redispersed in 10 mL hexane and prepared for microscopy.

The sample was prepared for high-resolution SEM microscopy using Micro to Nano EMR Holey Carbon support film on copper 300 square mesh, model 22-1MHC30-25 to support the sample, and glass Pasteur pipettes. One drop of the solution containing the nanoparticles was deposited on the support using a Pasteur pipette. The support was inserted into a container with an inlet- and outlet gas valve. The container was then sealed from the atmosphere. Hexane was evaporated by Ar flow in the sealed container overnight. The next day, the gas valves of the container were closed, and the sample was kept in an Ar atmosphere until it was measured.

3.3 Heat-up using the reflux method

For the heat-up experiments, a Radleys Carousel Tech hot plate equipped with a Pt1000 external temperature sensor, a laboratory scissor jack, 50 mL three-neck round flask, a condenser, a Brooks 1355/D2A3A1C5E020 gas meter, a gas valve connected to the flask, a K-type thermocouple with a custom-made glass liner, a magnetic stir bar, a bubbler filled with silicon oil, a Fluke 54 II B thermometer, Schlenk lines, and aluminum foil were used.

All syntheses were performed in two steps. The first step consisted in dissolving all of the reagents in the solvent being used. The surfactants and precursors were added to the three-neck round flask. Afterward, the thermocouple and the gas line were connected to the round flask. The Ar flow was turned on, and it measured 20 mm on the gas meter. The surfactant and precursors were then dissolved at their target temperature. The process is detailed for each synthesis in Experimental 3.3.2 to 3.3.5.

The nanoparticles were synthesized during the second step. First, we joined the three-neck round flask to a condenser. Next, the pre-heated hotplate was lifted using a laboratory scissors jack until the round flask was in contact with the hotplate surfaces. Aluminum foil was then wrapped around the round flask. The solution was stirred at 1400 rpm during the first and second steps of the syntheses. Figure 3.2 shows how the equipment was arranged at the end of the second step.

Figure 3.2: Equipment set-up for the syntheses using the heat-up method.

3.3.1 Relative reaction kinetics of Pt- and Rh precursors

In the first step of the syntheses, 2 mmol of PVP was dissolved by stirring in 20 mL ethylene glycol at 150 °C for 15 minutes. The temperature was then lowered to 120 °C and either 0.1 mmol $Pt(acac)_2$, 0.1 mmol $Rh(acac)_3$ or 0.1 mmol $Pt(acac)_2$ + 0.1 mmol $Rh(acac)_3$ was added to the round flask. The solution was stirred until the precursors were dissolved.

For the second step, an aliquot (circa 0.5 mL) was taken before starting the reduction of the metal precursors. Then the round flask was transferred to a hotplate pre-heated to 218 °C. As soon as the transfer process was completed, a timer was started. An aliquot of the syntheses was taken every two minutes for 8 minutes. Then an aliquot was taken every five minutes for 120 minutes. After the syntheses, an image of the aliquots (0-, 2-, 4-, ... 128 minutes) was obtained for the relative kinetics determination.

3.3.2 Two-hour synthesis using $Pt(acac)_2$ and $Rh(acac)_3$ in ethylene glycol (Synthesis 9)

In the first step of the synthesis, 2 mmol of PVP was dissolved in 20 mL ethylene glycol at 150 °C for 15 minutes. The temperature was then lowered to 120 °C, and 0.3 mmol $Pt(acac)_2$ + 0.1 mmol $Rh(acac)_3$ was added to the round flask. The solution was stirred until the precursors were dissolved. For the second step, the round flask was transferred to a hotplate pre-heated to 218 °C. Once the temperature of the solution had reached 195 °C, a timer was started. The synthesis was quenched by transferring the round flask to a hotplate at room temperature.

3.3.3 Syntheses of solid solution Pt_xRh_{1-x} nanoparticles (Syntheses 10, 11, and 12)

In the first step of the syntheses, 2 mmol of PVP was dissolved in 20 mL ethylene glycol at 150 °C for 15 minutes. The temperature was then lowered to 120 °C, and the metal precursors were added to the round flask (see Results 4.1.2.3 – Table 4.4). The solution was stirred until the precursors were dissolved. For the second step, the round flask was transferred to a hotplate pre-heated to 218 °C. Once the temperature of the solution had reached 195 °C, a timer was started. The synthesis was quenched after 15 minutes by transferring the round flask to an ice water bath.

3.3.4 Syntheses for development of Pt nanoparticles supported on Al_2O_3 catalyzers (Syntheses 13 to 17)

In the first step of the syntheses, 0.75 to 20.25 mmol of PVP was dissolved in 20 to 60 mL 1,4-butanediol at 150 °C for 15 minutes. The temperature was then lowered to 120 °C, and 0.075 mmol $Pt(acac)_2$ was added to the round flask. The solution was stirred until the precursors were dissolved. For the second step, the round flask was moved to a hotplate pre-heated to 240 °C to raise the solution's temperature quickly. After transferring the flask, the hotplate temperature was lowered to 230 °C, so the solution's temperature stabilized at ~220 °C. Once the solution's temperature reached 220 °C, a timer was started. After two hours, the synthesis was stopped by transferring the reactor to a "cold" hotplate.

3.3.5 Synthesis for development of Pt_xRh_{1-x} nanoparticles supported on Al_2O_3 catalyzers (Synthesis 18)

In the first step of the syntheses, 20.25 mmol of PVP was dissolved in 60 mL ethylene glycol at 150 °C for 15 minutes. The temperature was then lowered to 120 °C, and 0.15 mmol $Pt(acac)_2$ + 0.05 mmol $Rh(acac)_3$ was added to the round flask. The solution was stirred until the

precursors were dissolved. For the second step, the round flask was transferred to a hotplate pre-heated to 230 °C. Once the temperature of the solution had reached 195 °C, a timer was started. The synthesis was quenched after 15 minutes by transferring the round flask to an ice water bath.

3.3.6 Procedures for washing, redispersion, and microscopy sample preparation

For washing the nanoparticles, 15 mL VWR 12.5K max polypropylene centrifuge tubes were used. The nanoparticles were washed by transferring 3 mL of the prepared nanoparticle suspension into a centrifuge tube with 12 mL of acetone. The tube was vigorously shaken for a few seconds, followed by centrifugation at 4500 rpm for 3 minutes. After centrifugation, the supernatant was discarded. The second step was to add 10 mL acetone. The centrifuge tube was vigorously shaken for a few seconds, sonicated for one minute, and centrifuged at 4500 rpm for 3 minutes. After centrifugation, the supernatant was discarded, and the second step was repeated. The nanoparticles were redispersed in 20 mL methanol and prepared for microscopy or Al_2O_3 support deposition.

The samples were prepared for microscopy using the Micro to Nano EMR Holey Carbon support film on copper 300 square mesh, model 22-1MHC30-25. The *in situ* STEM measurements used the Fusion Thermal E-chip SiN thermal (serial number E-FHDC-VO). One drop of the solution containing the nanoparticles was deposited on the support using a Pasteur pipette. The support was inserted into a container with an inlet- and outlet gas valve. The container was then sealed from the atmosphere. The solvent used to redisperse the nanoparticles was evaporated by Ar flow in the sealed container overnight. The next day, the gas valves of the container were closed, and the sample was kept in an Ar atmosphere until it was measured.

3.4 Preparation of Pt and $Pt_{0.50}Rh_{0.50}$ supported on Al_2O_3

3.4.1 Calcination of boehmite

As received, boehmite was added to an alumina crucible and heated using a heat rate of 5 °C min^{-1} to 900 °C using a Carbolite Gero AAF 1100 oven. The sample was kept at 900 °C for 10 hours and cooled down to room temperature with no external input.

3.4.2 Deposition of Pt and solid solution $Pt_{0.50}Rh_{0.50}$ on Al_2O_3 support aiming for 0.5 weight percent metal load

To prepare a catalyst composed of 0.5 weight percent metal load, we estimated that 70 % of Pt for the monometallic catalyst and 35 % of Rh for the solid solution $Pt_{0.50}Rh_{0.50}$ were converted from precursor to metal. For details on the calculations, see Appendix Table A.1.

The as-synthesized and washed nanoparticles were redispersed in 30 mL methanol and sonicated for a few seconds. For the $Pt_{0.50}Rh_{0.50}$, 1.06 g, and for the monometallic Pt, 2.03 g of Al_2O_3 was used. The Al_2O_3 was then added to a beaker with a magnetic stir bar and 70 mL methanol. The solution containing Al_2O_3 was stirred with the help of a magnetic stir bar and a hotplate at 250 rpm. Then, the nanoparticles were added dropwise to the Al_2O_3 solution. After the nanoparticles were mixed with Al_2O_3, one drop of the resulting suspension was deposited on a Micro to Nano EMR Holey Carbon support film on copper 300 square mesh, model 22-1MHC30-25 for SEM imaging.

The beaker containing the catalyst was then added to a container with gas valves, and the container was sealed from the atmosphere. The methanol was dried overnight under Ar flow. Once the solvent had evaporated, the gas valves were closed, and the sample was stored in Ar atmosphere until they were calcinated.

3.4.3 Calcination of the catalyst

The Pt/Al_2O_3 and the $Pt_{0.50}Rh_{0.50}/Al_2O_3$ catalysts were crushed into a fine powder using a mortar and pestle. Then, ~2 g of catalyst was added to a glass oven tube, and the tube was connected to a synthetic air gas line. The Brooks 1355/D2A3A1C5E020 gas meter was set to 20mm for the gas flow. The glass oven tube was inserted into a Eurotherm 2408 oven and heated to 400 °C with a heating rate of 5°C min^{-1}. After reaching 400 °C, the oven stayed at the target temperature for 8 hours. The programmed cooled-down temperature was 10 °C min^{-1}. After cooling down, the sample was prepared for microscopy by suspending 0.1 g in 1 mL methanol. For SEM imaging, one drop of the methanol solution was deposited onto a Micro to Nano EMR Holey Carbon support film on copper 300 square mesh, model 22-1MHC30-25.

3.5 Powder XRD measurements

PXRD patterns were recorded for the free-standing Pt_xRh_{1-x} and the boehmite sample before- and after calcination. The instrument used was a Bruker D8 Discover diffractometer with

Bragg-Brentano geometry. The system used Cu $K\alpha_1$ ($\lambda = 1.5406$ Å) X-ray radiation, a LynxEye detector, and a single crystal (Ge(111)) monochromator.

The X-ray diffractogram for nanoparticles was obtained by a series of two measurements. The first was optimized for the nanoparticles with a step size of 0.100 °. The second was optimized for the Si NIST standard, with a step size of 0.016 °. The scan range was from 30 to 90 2θ° for both measurements. The X-ray diffractogram for the alumina sample was measured at a step-size of 0.100 °, with the scan range from 10 to 90 2θ°.

Structural analysis with Rietveld refinement (Methods and Theory 2.8.3) was performed using the software TOPAS[103]. The crystallographic information files (CIF) were obtained from the Inorganic Crystal Structure Database[104]. The height displacement, background, a-axis, and zero-point error were refined. The height displacement and zero-point error parameters were kept constant, reflecting the values measured from the Si standard from the National Institute of Standards and Technology. The uncertainty was calculated using the least square approach. Phase identification was performed using the software DIFRAC.SUITE EVA[105] version 5.2.0.3 and the powder diffraction files (PDF) 4+, 2021[106] database.

3.6 Electron microscopy

3.6.1 Transmission electron microscopy

The TEM microscope used was a Monochromated Titan 60-300kV with Super-X EDS and GIF Quantum ER 965 spectrometer, probe corrected to 0.8 Å spatial resolution. The microscope was operated at 300 kV and 100 picoamperes beam current in bright-field-STEM, HAADF-STEM, and STEM-EDS maps. For the *in situ* measurements, the beam current was reduced to 50 picoamperes.

The measurements used a Micro to Nano EMR Holey Carbon support film on copper 300 square mesh, model 22-1MHC30-25, supported by a FEI double tilt holder. The samples were supported for *in situ* measurements using a Protochips® Fusion holder and the Fusion Thermal E-chip SiN thermal, serial number E-FHDC-VO. The Fusion Thermal E-chip was plasma cleaned unshielded for 5 minutes using a Fischione Plasma Cleaner before sample deposition.

The obtained TEM data were treated using Velox® version 3.3.1.19-397c043e56. When the data of the STEM-EDS-map was diffuse, the Velox's® recommended filter was applied. The kernel size used was recommended by the software (Figure 3.3).

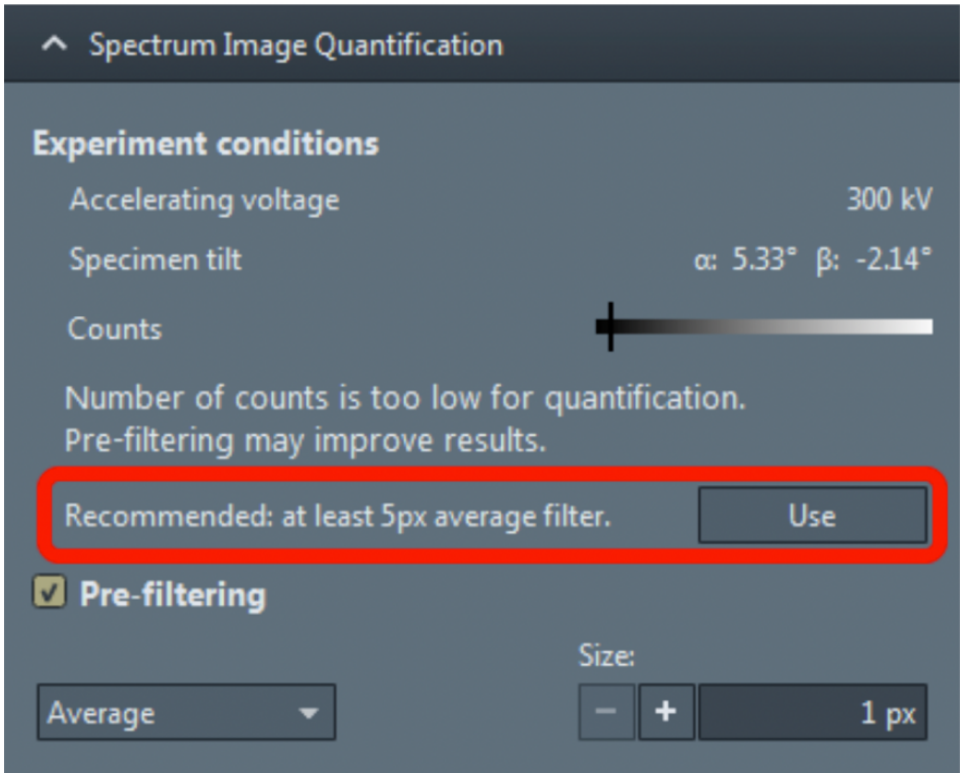

Figure 3.3: Applying the prefilter with the kernel recommended by Velox®. The image was taken from Velox® manual[107].

Accounting for beam damage during in situ experiments

To account for enhanced diffusion processes due to knock-on damage, at least 100 STEM-EDS frames were obtained with the HAADF-STEM of the first and the HAADF-STEM of the last EDS map. The *first*- and *last* 50 STEM-EDS frames were superimposed and placed side by side with the *first*- and *last* HAADF-STEM image, respectively, for direct comparison.

3.6.2 Scanning electron microscopy

A Hitachi SU8230 Ultra High-Resolution Cold FE-SEM was used to obtain high-resolution SEM images. The samples were supported by a Micro to Nano EMR Holey Carbon support film on copper 300 square mesh, model 22-1MHC30-25. The samples were measured at 25 kV using either the STEM-, the SE- or the LABE detector. When the sample contained carbon contamination during the measurements, it was plasma cleaned for 10 seconds at 15 watts.

3.6.3 Preparation of histograms from electron microscopy images

The software ImageJ version 2.3.0/1.53q was used to measure the nanoparticles' size. Firstly, the software was calibrated by measuring the scalebar of the microscopy image and obtaining a pixel nm^{-1} ratio. Then, each nanoparticle was measured from the direction it appeared to be most prominent in size. The nanoparticles that overlapped with others or were not in their entirety within the image were not measured. For an example of how the nanoparticles were measured, see Figure 3.4.

The histograms were prepared by counting 250 nanoparticles. The measured values were transferred to Origin 2020 (64 bit) SR1, and the histogram was prepared using the plot-statistical-histogram function. The number of beams used in the histogram figures was recommended by Origin. The size of the nanoparticles was reported using $\overline{D} = \pm\sigma$, where $\overline{D}$ corresponds to the average size of the nanoparticles, and $\pm\sigma$ is the standard deviation.

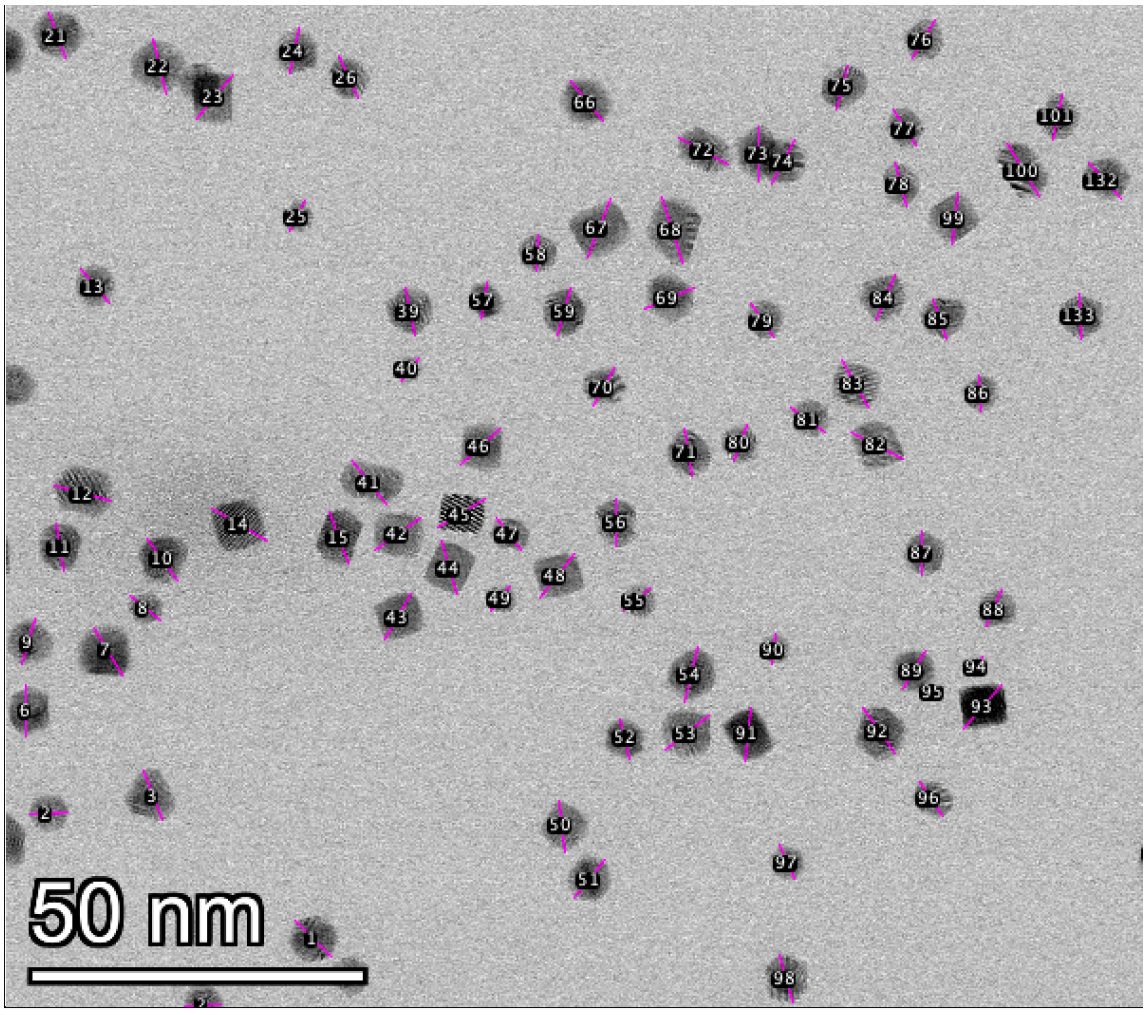

Figure 3.4: Example of how nanoparticles size was measured using the ImageJ software.

4 Results

4.1 Synthesis of solid solution Pt_xRh_{1-x} nanoparticles

Two strategies for producing bimetallic nanoparticles of Pt_xRh_{1-x} in the solid solution configurations were attempted in parallel: the autoclave method (Experimental 3.2) and heat-up using the reflux method (Experimental 3.3). The results of the two methods are described below, of which the reflux method was selected for further experimental work (Figure 4.1).

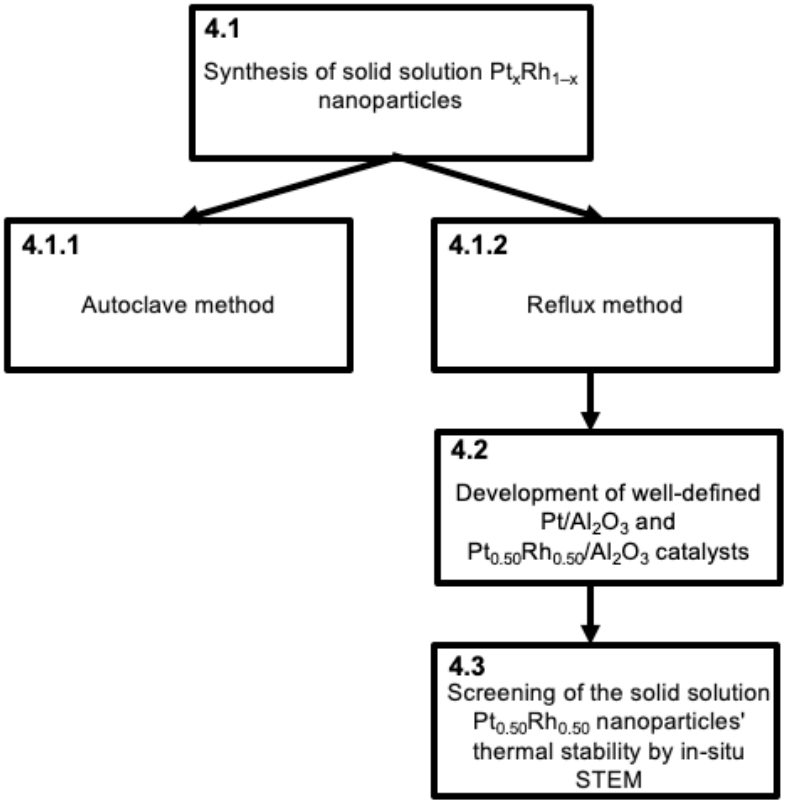

Figure 4.1: Overview of the experimental workflow.

4.1.1 Synthesis of solid solution Pt_xRh_{1-x} nanoparticles through the autoclave method

4.1.1.1 Benchmarking a Pd nanoparticle synthesis using the autoclave method

To establish a procedure to make bimetallic nanoparticles of Pt_xRh_{1-x} in the solid solution configuration, a published synthesis for Pd nanoparticles by Niu et al.[74] was used as a starting point. The synthesis route was chosen for its simplicity and because the chemistry of Pd is similar to Pt.

In Synthesis 1, 12.2 mg (0.040 mmol) of $Pd(acac)_2$ and 0.020 mL (0.061 mmol) of oleylamine were dissolved and stirred for 10 minutes in 5 mL toluene. Afterward, 0.025 mL of

formaldehyde solution was added to the system under stirring and further stirred for 10 minutes at room temperature. The next step was to heat up the solution to 100 °C in an autoclave for 8 hours and then slowly cool it down to room temperature (Table 4.1). After the synthesis, the nanoparticles were prepared for high-resolution SEM imaging (See the procedures outlined in Experimental 3.2 for the autoclave synthesis and SEM sample preparation for experimental details).

Figure 4.2A provides an overview of the nanoparticles obtained in Synthesis 1 using the SEM in bright-field STEM mode. The imaging shows that the synthesis produced agglomerated nanoparticles. Investigation of the surface of the agglomerates using the SE mode (Figure 4.2B) shows that the product was polydispersed concerning size and morphology. As the synthesis was performed with Teflon® inserts previously used in other syntheses, contamination within the pores of the insert possibly acted as nucleation sites. If more than one nucleation event occurs, the supersaturation and nucleation followed by nanoparticle growth predicted by LaMer's model[56] are no longer applicable (Methods and Theory 2.1.2)[108]. The nanoparticles from Synthesis 1 were likely formed by multiple nucleation events, causing some nanoparticles to be relatively large and others small (Methods and Theory 2.1.1).

Synthesis 2 used identical conditions to Synthesis 1 (Table 4.1) but with new Teflon® inserts. After the synthesis, the nanoparticles were prepared for high-resolution SEM imaging. When visualized using the bright-field STEM mode, the products of Synthesis 2 were still agglomerated (Figure 4.2C). The surfaces of the agglomerates were then investigated using the SE mode, revealing nanoparticles that appear to have narrow size distribution, thus solving the issue of heterogeneous nucleation (Figure 4.2D). However, the synthesis described by Niu et al. produced non-agglomerated icosahedra nanoparticles[74], while Synthesis 2 produced agglomerated nanoparticles containing various polygons. Synthesis 2 was therefore further modified in order to solve the agglomeration issue, and the products of the syntheses to follow are no longer expected to be similar to Niu et al.[74].

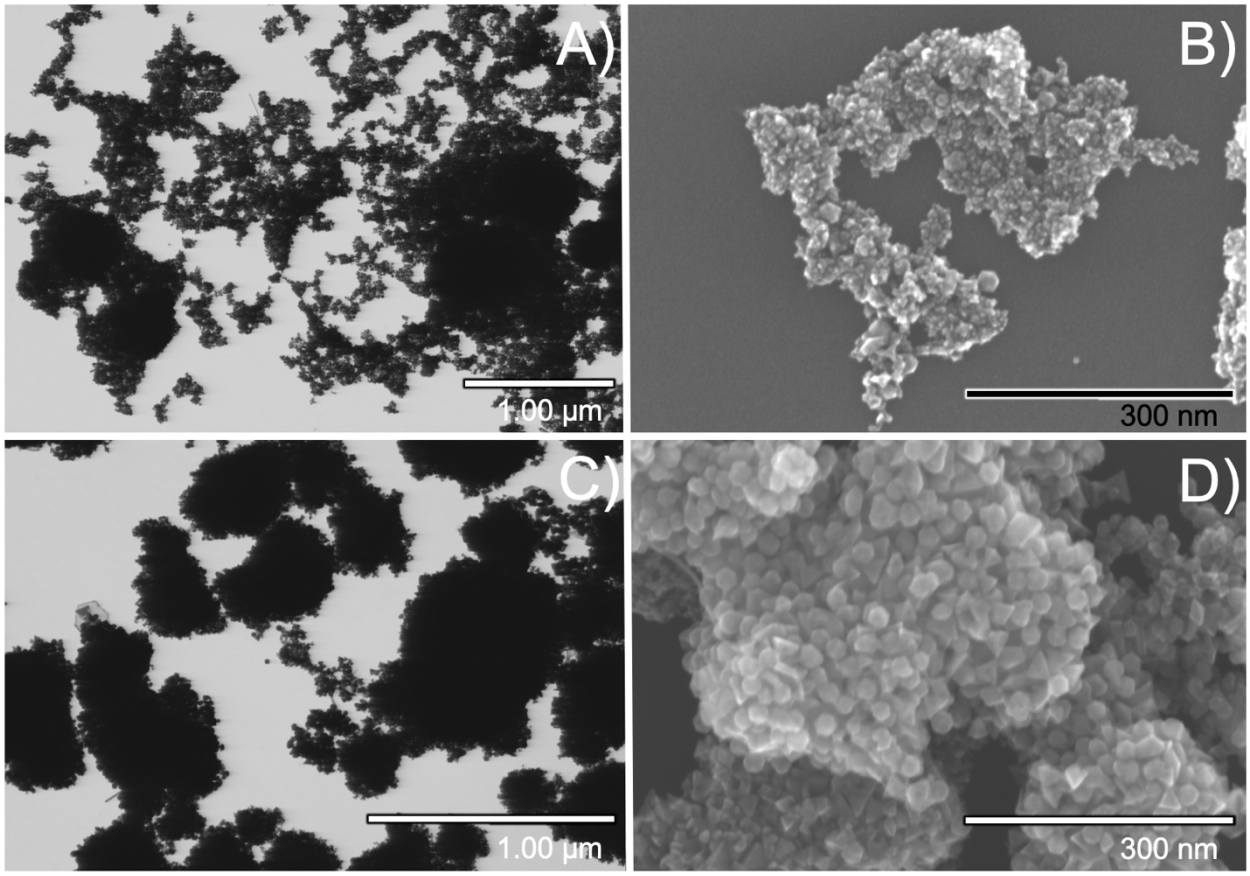

Figure 4.2: Synthesis of Pd nanoparticles through the autoclave method. A) High-resolution SEM image in bright-field STEM mode of products from Synthesis 1; B) High-resolution SEM image in SE mode of products from Synthesis 1; C) High-resolution SEM image in bright-field STEM mode of products from Synthesis 2; D) High-resolution SEM image in SE mode of products from Synthesis 2.

Nanoparticle agglomeration could occur due to either lack of, or excess of surfactant[63] (Methods and Theory 2.2). For that reason, Synthesis 3 and Synthesis 4 were performed using different amounts of oleylamine to test how surfactant concentration affects the nanoparticles' dispersion. The concentration of oleylamine was reduced by a factor of 5 (0.004 mL – 0.012 mmol used) in Synthesis 3 and increased by a factor of 2 (0.04 mL – 0.12 mmol used) in Synthesis 4 when compared to Synthesis 2 (0.020 mL – 0.061 mmol).

In Synthesis 3, the color change from light to dark indicated that a reaction occurred upon heating the solution to 100 °C (Figure 4.3A), whereas in Synthesis 4, the solution retained its original bright yellow color after heating to 100 °C (Figure 4.3B). We, therefore, concluded that no reaction happened in Synthesis 4 at 100 °C. Synthesis 3 was further prepared for high-resolution SEM imaging, and Synthesis 4 was discarded. We believe that Synthesis 4 failed due

to the complexation of Pd(II) by oleylamine[109], stabilizing the metal species against reduction by formaldehyde.

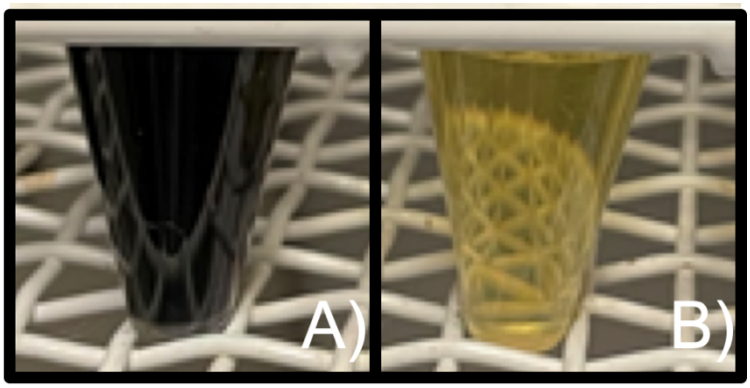

Figure 4.3: Color of Pd nanoparticles solution after completed synthesis. A) Synthesis 3; B) Synthesis 4.

Figure 4.4 shows images of the products of Synthesis 3 in bright-field STEM mode (A) and in SE mode of the surface (B). They demonstrate that the sample was composed of agglomerates (Figure 4.4A) formed of round structures of around 100 nm in size, interconnected by a neck in three dimensions (Figure 4.4B). When comparing the products of Synthesis 2 (Figure 4.3D) with the products of Synthesis 3 (Figure 4.4B), it can be noted that Synthesis 2 created agglomerated nanoparticles. In contrast, Synthesis 3 appeared to have formed nanoparticles that agglomerated and fused due to a lack of surfactant (Methods and Theory 2.2).

In a literature search for synthesis alternatives at the University of Oslo library catalog, using the search engine Oria and the keywords "monodisperse Pd nanoparticles synthesis oleylamine", an article was identified entitled "Synthesis of nearly monodisperse Pd (Pd) nanoparticles by using oleylamine and trioctylphosphine mixed ligands" by Yang et al.[110]. The authors demonstrate that when oleylamine participates in the reduction of Pd ion to metal, aggregated Pd nanoparticles form[110]. Yang et al. solved the agglomeration issue by using two surfactants for their synthesis: oleylamine and trioctylphosphine[110]. It was found that adding a molar ratio of either 0.6- or 1 trioctylphosphine to 1 $Pd(acac)_2$ leads to the formation of non-agglomerated, near monodispersed Pd nanoparticles[110]. For that reason, Syntheses 5 and 6 were performed using the same conditions as Synthesis 2, while adding a 1 to 1 molar ratio of trioctylphosphine to $Pd(acac)_2$ in Synthesis 5, and a 0.6 to 1 molar ratio of trioctylphosphine to $Pd(acac)_2$ in Synthesis 6 (Table 4.1).

Figure 4.4C and D show images in bright-field STEM mode from the products of Syntheses 5 and 6, respectively. While Synthesis 5 produced fibrillar agglomerates (Figure 4.4C), Synthesis 6 produced non-agglomerated, monodisperse nanoparticles (Figure 4.4D). The average size of the nanoparticles was 2.3 ± 0.6 nm in Synthesis 5 (Figure 4.4E) and 3.2 ± 0.5 nm in Synthesis 6 (Figure 4.4F). Synthesis 5, containing a higher concentration of trioctylphosphine, produced smaller nanoparticles than Synthesis 6, confirming the trend observed by Yang et al.[110].

Another observation was that the products of Synthesis 5 appeared to have agglomerated due to excess surfactant. When surfactants are used in excess, van der Waals attractive forces may become dominant among the nanoparticles, resulting in agglomeration[63]. In Synthesis 6, the concentration of trioctylphosphine was reduced by 55 %, resulting in dispersed nanoparticles. No further efforts were made to tune nanoparticle size for this synthesis, as Pd was only used to benchmark a synthesis for Pt. At this point, the synthesis for Pd was considered benchmarked. The next step was to transfer the new standardized procedure to produce Pt nanoparticles.

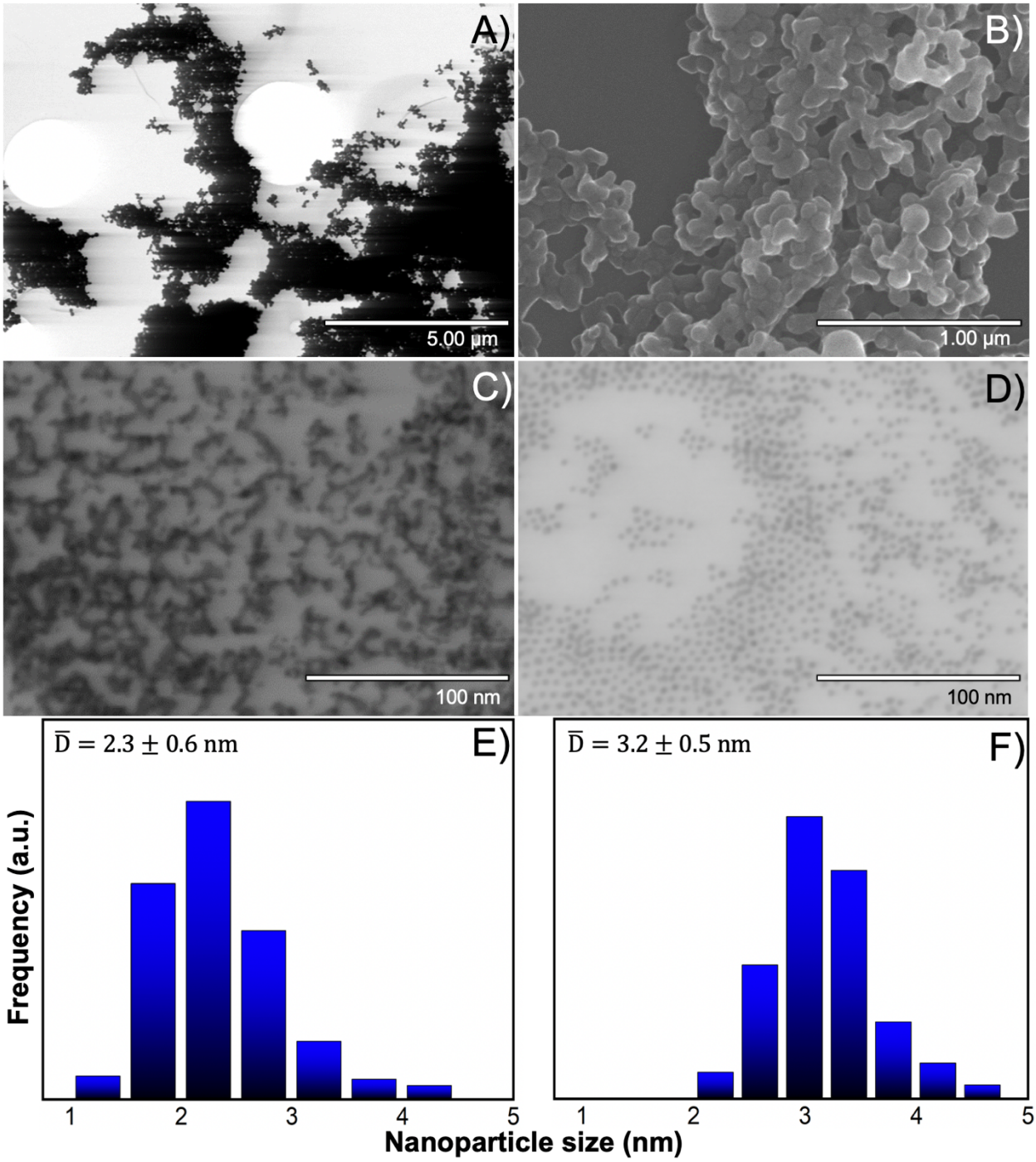

Figure 4.4: Synthesis of Pd nanoparticles through the autoclave method using two surfactants. A) High-resolution SEM image in bright-field STEM mode of the products from Synthesis 3; B) High-resolution SEM image in SE mode of the products from Synthesis 3; High-resolution SEM image in bright-field STEM mode of the products from C) Synthesis 5 and D) Synthesis 6; Histogram of the products of E) Synthesis 5 and F) Synthesis 6, prepared by counting 250 nanoparticles.

4.1.1.2 Adapting the Pd nanoparticle synthesis to produce Pt nanoparticles

For the first synthesis using Pt, Synthesis 7, the same parameters used for Synthesis 6 were used, but the $Pd(acac)_2$ precursor was substituted by the same molar amount of $Pt(acac)_2$ (Table 4.1). The first trial did not yield any product at the end of Synthesis 7, as the solution had not changed colors. Synthesis 8 was then attempted using the same parameters as Synthesis 7 but raising the temperature from 100 °C to 130 °C (Table 4.1). When the system had cooled to room temperature, Synthesis 8 was prepared for and studied using high-resolution SEM imaging.

Figure 4.5 shows an image in the bright-field STEM mode of the products from Synthesis 8, depicting successfully synthesized Pt nanoparticles. The average size based on 250 Pt nanoparticles was 2.5 ± 0.3 nm (Figure 4.5 – insert). Thus, Synthesis 8 successfully produced dispersed Pt nanoparticles with narrow size distribution (12 %).

No further experiments were performed using the autoclave method, as solid solution nanoparticles of Pt_xRh_{1-x} was achieved using the heat-up method (Results 4.1.2). However, there were several remaining steps. Products from Synthesis 8 would need to be characterized using PXRD to confirm that Pt nanoparticles were synthesized. In addition, the nanoparticles were smaller than the target of 6- to 12 nm. Thus, a strategy to increase the size of the nanoparticles would need to be implemented. More importantly, Rh would need to be incorporated, and the system adapted to create a Pt_xRh_{1-x} solid solution.

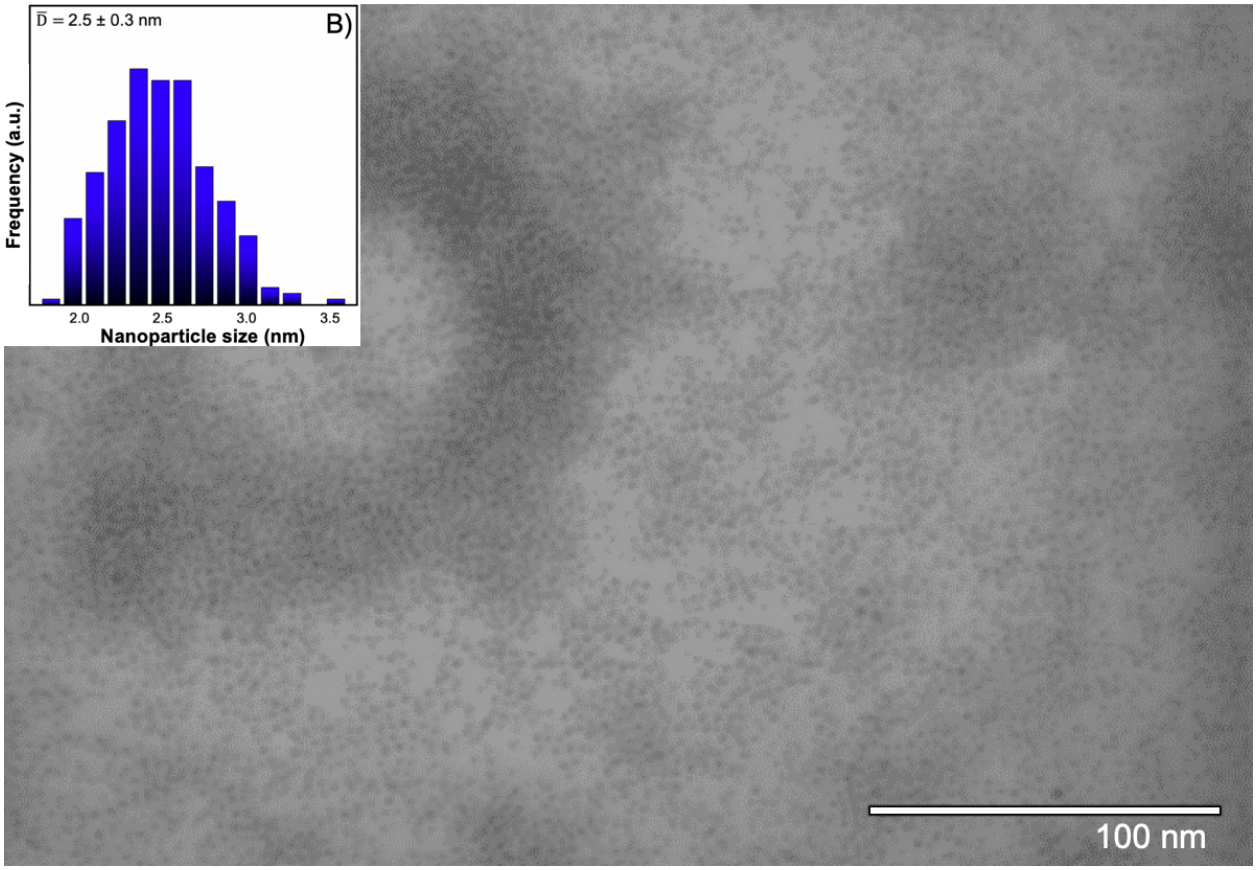

Figure 4.5: Synthesis of Pd nanoparticles through the autoclave method. High-resolution SEM image in bright-field STEM mode of the products from Synthesis 8; The insert shows a histogram of products from Synthesis 8.

Table 4.1: Syntheses parameters for benchmarking the synthesis route published by Niu et al.[74] and Yang et al.[110]. TOP, trioctylphosphine. OAm, oleylamine.

Synthesis conditions to produce Pd nanoparticles							
Synthesis	**$Pd(acac)_2$ mg mmol**	**Toluene mL**	**OAm mL mmol**	**TOP mL mmol**	**Formaldehyde mL**	**Temperature °C**	**Comments**
1	12.2 0.040	5	0.020 0.061	-	0.025	100	Reproduced procedure from Niu et al.[74] Produced agglomerated ill-defined nanoparticles.
2	12.2 0.040	5	0.020 0.061	-	0.025	100	Used new Teflon® insert. Produced agglomerated well-defined nanoparticles.
3	12.2 0.040	5	0.0040 0.012	-	0.025	100	Produced bulk material.
4	12.2 0.040	5	0.040 0.12	-	0.025	100	No reaction happened.
5	12.2 0.040	5	0.020 0.061	0.018 0.040	0.025	100	The nanoparticles were agglomerated due to excess surfactant[63].
6	12.2 0.040	5	0.020 0.061	0.010 0.023	0.025	100	The synthesis was successful.
Synthesis conditions to produce Pt nanoparticles							
Synthesis	**$Pt(acac)_2$ mg mmol**	**Toluene mL**	**OAm mL mmol**	**TOP mL mmol**	**Formaldehyde mL**	**Temperature °C**	**Comments**
7	15.8 0.040	5	0.020 0.061	0.010 0.023	0.025	100	No reaction occurred.
8	15.8 0.040	5	0.020 0.061	0.010 0.023	0.025	130	The synthesis was successful.

4.1.2 Solid solution Pt_xRh_{1-x} nanoparticles through heat-up using the reflux method

4.1.2.1 Relative reaction kinetics of Pt- and Rh precursors

As a first step to synthesizing Pt_xRh_{1-x} nanoparticles using the reflux method, we examined the relative reaction kinetics of the $Pt(acac)_2$ and $Rh(acac)_3$ metal precursors for nanoparticle formation. Three different solutions were prepared containing a) 0.1 mmol $Pt(acac)_2$ and 2 mmol PVP in 20 mL ethylene glycol, b) 0.1 mmol $Rh(acac)_3$ and 2 mmol PVP in ethylene glycol, and c) 0.1 mmol $Pt(acac)_2$, 0.1 mmol $Rh(acac)_3$, and 2 mmol PVP in ethylene glycol. First, the precursors were dissolved at 120 °C. The reaction was initiated by quickly heating the solution to 195 °C. An aliquot was taken every two minutes for eight minutes, and then every five minutes. All three solutions were allowed to react for 128 minutes (Experimental 3.3.1). In this experiment, the solution's color change from bright yellow to dark brown is interpreted as the amount of precursor reduced to Pt or Rh metal, respectively[29,35].

Figure 4.6 depicts the color change (bright yellow to dark brown) of the solutions versus time for $Rh(acac)_3$ (A), $Pt(acac)_2$ (B) and $Rh(acac)_3$ + $Pt(acac)_2$ (C). Figure 4.6A shows that the Rh-solution started turning brown after 4 minutes, and after the 23-minute mark, the solution is dark brown. In Figure 4.6B, the Pt-solution starts turning brown at the 6-minute mark, and the solution is dark brown after 113 minutes. Interestingly, the solution containing both Pt and Rh (Figure 4.6C) starts turning brown at the 4-minute mark, and after 23 minutes, the solution turned dark brown. This pattern is near identical to the Rh-solution (Figure 4.6A).

As the color of the solution containing $Rh(acac)_3$ darkens faster than the one containing $Pt(acac)_2$, it can be concluded that the Rh precursor has a higher kinetic rate constant toward the formation of nanoparticles than the Pt precursor in ethylene glycol. This result agrees with the findings of Bundli et al. for the Pt_xRh_{1-x} solid solution nanoparticles synthesized in 1,4-butanediol[29].

Figure 4.6 shows the estimated reaction windows for $Rh(acac)_3$ in red and $Pt(acac)_2$ in green. The reaction windows of $Rh(acac)_3$ and $Pt(acac)_2$ were superimposed in Figure 4.6C, and the area where the two reactants overlap is shown in blue. From Figure 4.6C, it can be hypothesized that if equimolar amounts of $Pt(acac)_2$ and $Rh(acac)_3$ were to react in ethylene glycol for 128 minutes, solid solution core – Pt-enriched shell nanoparticles should form. If so, the configuration of the nanoparticles would be equivalent to those produced by Bundli et al. in 1,4-butanediol[29].

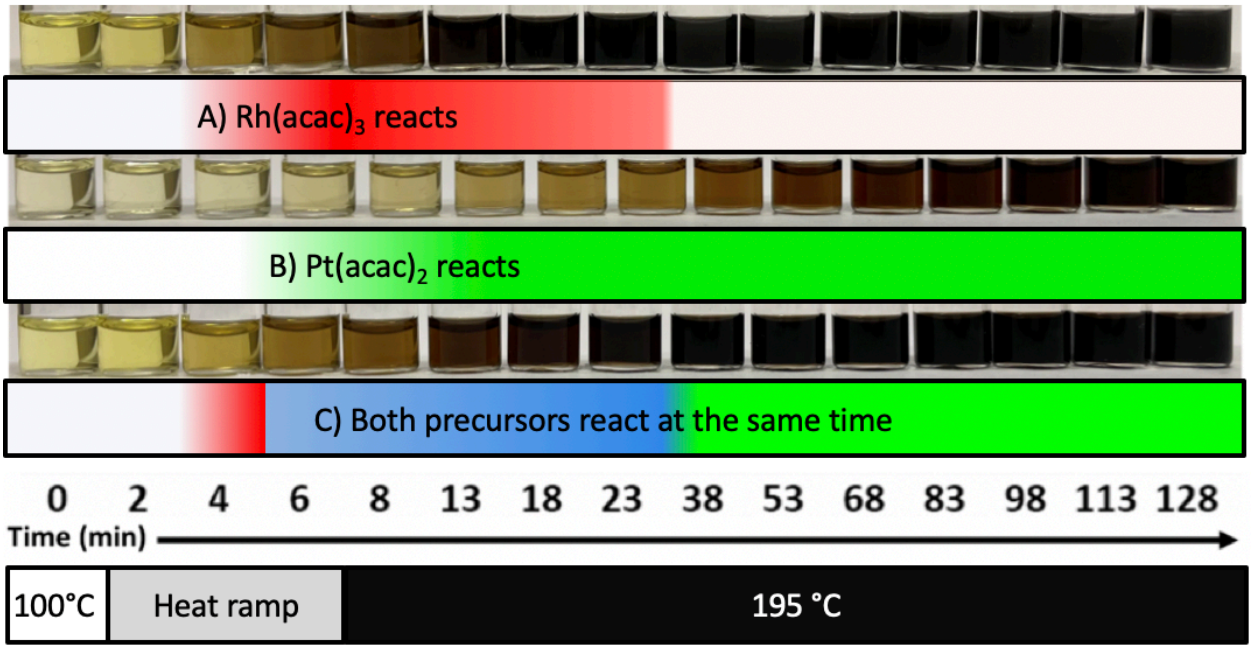

Figure 4.6: Relative reaction kinetics of Pt- and Rh precursors measured through color change. A) 0.1 mmol $Rh(acac)_3$ and 2 mmol PVP in ethylene glycol; B) 0.1 mmol $Pt(acac)_2$ and 2 mmol PVP in ethylene glycol; C) 0.1 mmol $Pt(acac)_2$ + 0.1 mmol $Rh(acac)_3$ and 2 mmol PVP in ethylene glycol. The reaction window for Rh is shown in red, for Pt in green, and for Pt and Rh are reacting simultaneously in blue.

4.1.2.2 Nanoparticles produced by a two-hour heat-up synthesis using $Pt(acac)_2$ and $Rh(acac)_3$ in ethylene glycol

Synthesis 9 was performed to test the premise that if $Pt(acac)_2$ and $Rh(acac)_3$ are allowed to react in ethylene glycol for two hours, a Pt_xRh_{1-x} core and a Pt-enriched shell would form (see Table 4.4 for details). Synthesis 9 follows the procedure outlined by Bundli et al.[29], using 0.3 mmol $Pt(acac)_2$, 0.1 mmol $Rh(acac)_3$, and 2 mmol PVP in 20 mL ethylene glycol. The reactants were dissolved at 120 °C, and the synthesis was initiated by quickly heating the solution to 195 °C. The total reaction time was two hours after the solution reached the target temperature (Experimental 3.3.2). Afterward, the obtained suspension was cooled down to room temperature, and the particles were washed and prepared for STEM measurements as outlined in Experimental (3.3.6). A large amount of $Pt(acac)_2$ compared to $Rh(acac)_3$ was used in this synthesis to easily identify the formation of the eventual Pt-enriched shell, if formed. If both reactants' reduction kinetics were equivalent, the resultant product would have been a nanoparticle having the solid solution configuration of $Pt_{0.75}Rh_{0.25}$.

In order to examine the stoichiometry of the products from Synthesis 9, an area containing over 1000 nanoparticles was measured using EDS. The measured sample contained 71 ± 2 % Pt and 29 ± 2 % Rh. The atomic error is reported as shown by Velox® (Experimental 3.6). The measurements correspond with the molar concentration of Pt and Rh added before the synthesis.

The next step was to analyze the homogeneity in element distribution of single particles from Synthesis 9 using EDS atomic-scale resolution elemental mapping (EDS map). Representative nanoparticles are depicted in Figure 4.7, where the signal for Rh is shown in red and Pt in green. As expected, the Rh signal was intense at the center and diffuse at the edges of the nanoparticle (Figure 4.7A). Conversely, the Pt signal was evenly distributed throughout the same nanoparticle (Figure 4.7B).

When examining a nanoparticle with signals from Pt and Rh superimposed, the signals of Rh and Pt appear to be evenly intense in the center, but at the edges, the Rh signal intensity wanes off compared to that of Pt (4.7C). In contrast, the Pt signal appears more intense toward the edges of the nanoparticles. Figure 4.7D plots a line scan, showing the signal for Pt and Rh for each position of the arrow in Figure 4.7C. The signal was normalized to 1 to allow the intensity of the two lines to be directly comparable. The blue box indicates the area where Pt and Rh have comparable intensities. Outside of this area, the Pt signal is higher than that of Rh, confirming the hypothesis in Results 4.1.2.1 that Pt-enriched shell nanoparticles would form in a two-hour synthesis.

To conclude, Synthesis 9 produced nanoparticles with a solid solution Pt_xRh_{1-x} core with a Pt-enriched shell. This synthesis approach and results are similar to Bundli et al., where the same strategy was applied using 1,4-butanediol as a solvent[29].

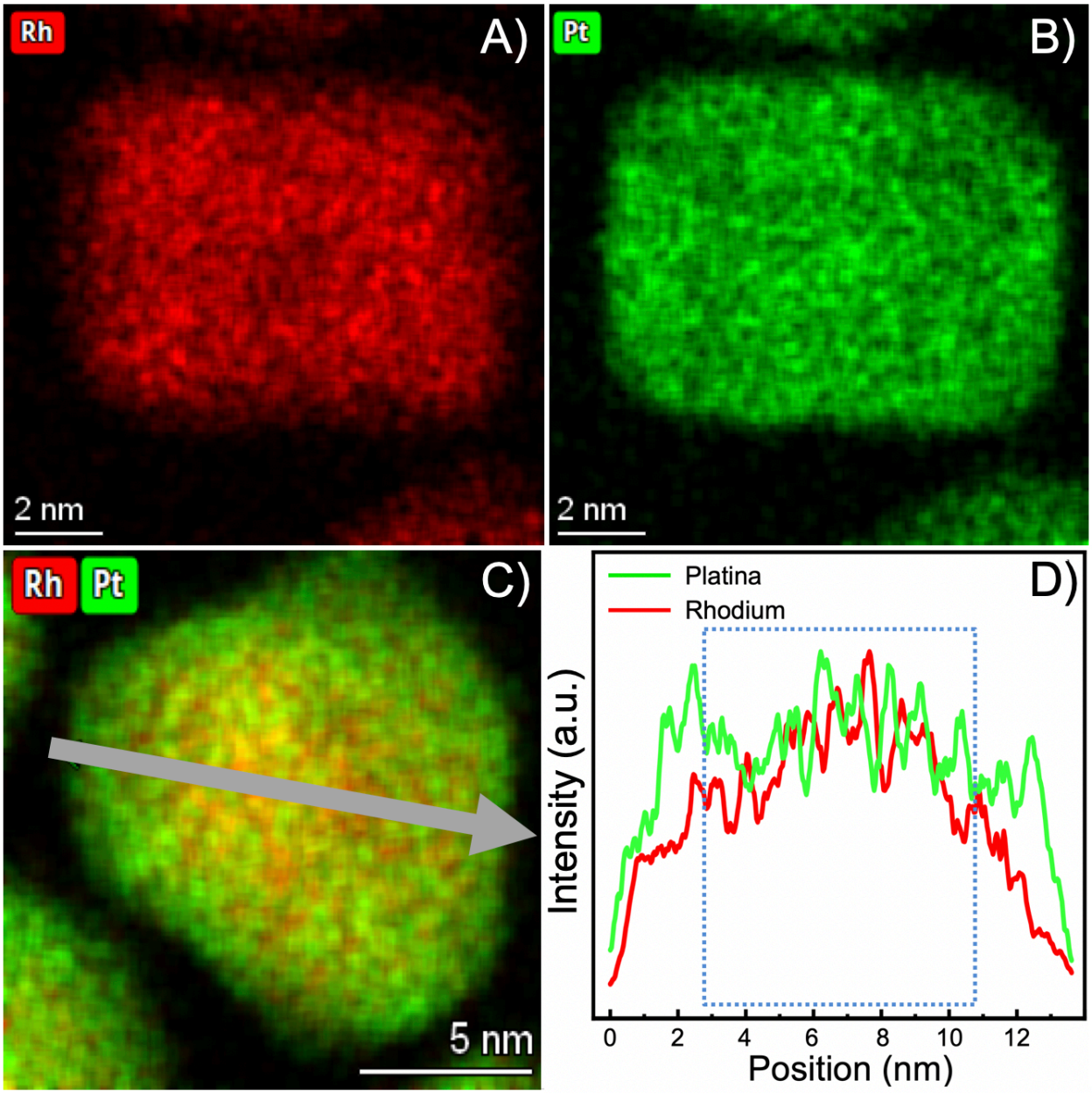

Figure 4.7: EDS map image of nanoparticles from Synthesis 9. A) Atomic distribution of Rh throughout the nanoparticle; B) Atomic distribution of Pt throughout the same nanoparticle shown in A); C) Atomic distribution of Pt and Rh throughout the nanoparticle with an arrow indicating the position and direction of the line scan; D) Line scan of the signal intensity of Pt and Rh for each position of the arrow from C). The perimeter of the blue box demarcates the area where the signal for Pt and Rh appear equivalent. The signal for Rh is shown in red and for Pt in green.

4.1.2.3 Quenching the synthesis for homogeneous element distribution in solid solution Pt_xRh_{1-x} nanoparticles

As the synthesis described in Results 4.1.2.2 produced a solid solution of Pt_xRh_{1-x} core and a Pt-enriched shell (Figure 4.7), we sought to revise the synthesis further to achieve Pt_xRh_{1-x} nanoparticles with homogeneous element distribution. By revisiting Figure 4.6, it can be noted that Rh starts reacting a little earlier than Pt. However, Figure 4.6C indicates that between 6- and 23 minutes of synthesis time, both $Pt(acac)_2$ and $Rh(acac)_3$ react simultaneously. The formation of a solid solution core in Synthesis 9 (Figure 4.7D) also strengthens the notion that initially, the two metal precursors are reacting simultaneously. Thus, as a next logical step, we wished to perform a synthesis with similar conditions as Synthesis 9, but where the reaction is quenched before all $Pt(acac)_2$ is consumed. For this purpose, the 15-minute mark was chosen because the color for the solution containing $Rh(acac)_3$ had just turned dark while most of the Pt precursor was still unreacted (Figure 4.6A, B). For that reason, we hypothesized that if the synthesis is quenched at the 15-minute mark, a Pt-enriched shell will not form.

For Synthesis 10, 0.1 mmol $Rh(acac)_3$, 0.1 mmol $Pt(acac)_2$, and 2 mmol PVP were dissolved in ethylene glycol at 120 °C (see Table 4.4 for details). The mixture was allowed to react for 15 minutes after the reactor reached 195 °C. The synthesis was then quenched by transferring the reactor to an ice bath. The product of Synthesis 10 was then washed and prepared for STEM, following the procedure outlined in Experimental (3.3.3 and 3.3.6).

In order to check the stoichiometry of the products from Synthesis 10, an area containing over 1000 nanoparticles was examined by EDS to obtain the average composition of the nanoparticles. Afterward, five single nanoparticles were measured by EDS (Table 4.2). The average composition of the nanoparticles was 24 ± 2 % Pt and 76 ± 2 % Rh. The five individual nanoparticles displayed a representative composition, with error margins overlapping with the larger sample. Notably, the EDS measurements of neither the sample of > 1000 nanoparticles nor the five single nanoparticles agreed with the synthesis' nominal composition of 50 atomic % Pt and 50 atomic % Rh.

Table 4.2: EDS elemental composition of an area containing > 1000 nanoparticles and five single nanoparticles from Synthesis 10. Nominal composition for the synthesis: 50 atomic % Pt and 50 atomic % Rh. Nominal composition refers to the amount of precursor used in the synthesis. NP, nanoparticle.

Synthesis 10	**Area with > 1000 NPs**	**NP 1**	**NP 2**	**NP 3**	**NP 4**	**NP 5**
Pt (atomic %)	24 ± 2	21 ± 3	20 ± 3	21 ± 3	25 ± 3	20 ± 3
Rh (atomic %)	76 ± 2	79 ± 10	80 ± 8	79 ± 8	75 ± 8	80 ± 8

The homogeneity in element distribution of single particles from Synthesis 10 was analyzed by an EDS map. Representative nanoparticles are depicted in Figure 4.8, where the signal for Rh is shown in red and Pt in green. Figure 4.8A shows that the Rh signal is more intense at the center of the nanoparticle, while the signal decreases steadily from the center toward the edges. Interestingly, the Pt signal for the same nanoparticle follows the pattern of Rh, with a more intense signal at the center and decreasing intensity toward the edges (Figure 4.8B). However, the overall intensity of the signal appears lower for Pt than for Rh throughout the nanoparticle (Figure 4.8A, B).

This is further investigated by superimposing the signal from Pt and Rh on a different nanoparticle (Figure 4.8C), showing that both appear to be evenly distributed, and there is no clear Pt enrichment at the edges. By plotting a line scan, showing the signal for Pt and Rh for each position of the arrow in Figure 4.8C, we see that there are a few areas where the nanoparticle is enriched in either Rh or Pt (Figure 4.8D), an expected outcome in solid solution alloys (Methods and Theory 2.5 – Figure 2.10). Moreover, the distribution of Pt and Rh appears to be uniform throughout the nanoparticle (Figure 4.8D), indicating that a solid solution system has been achieved.

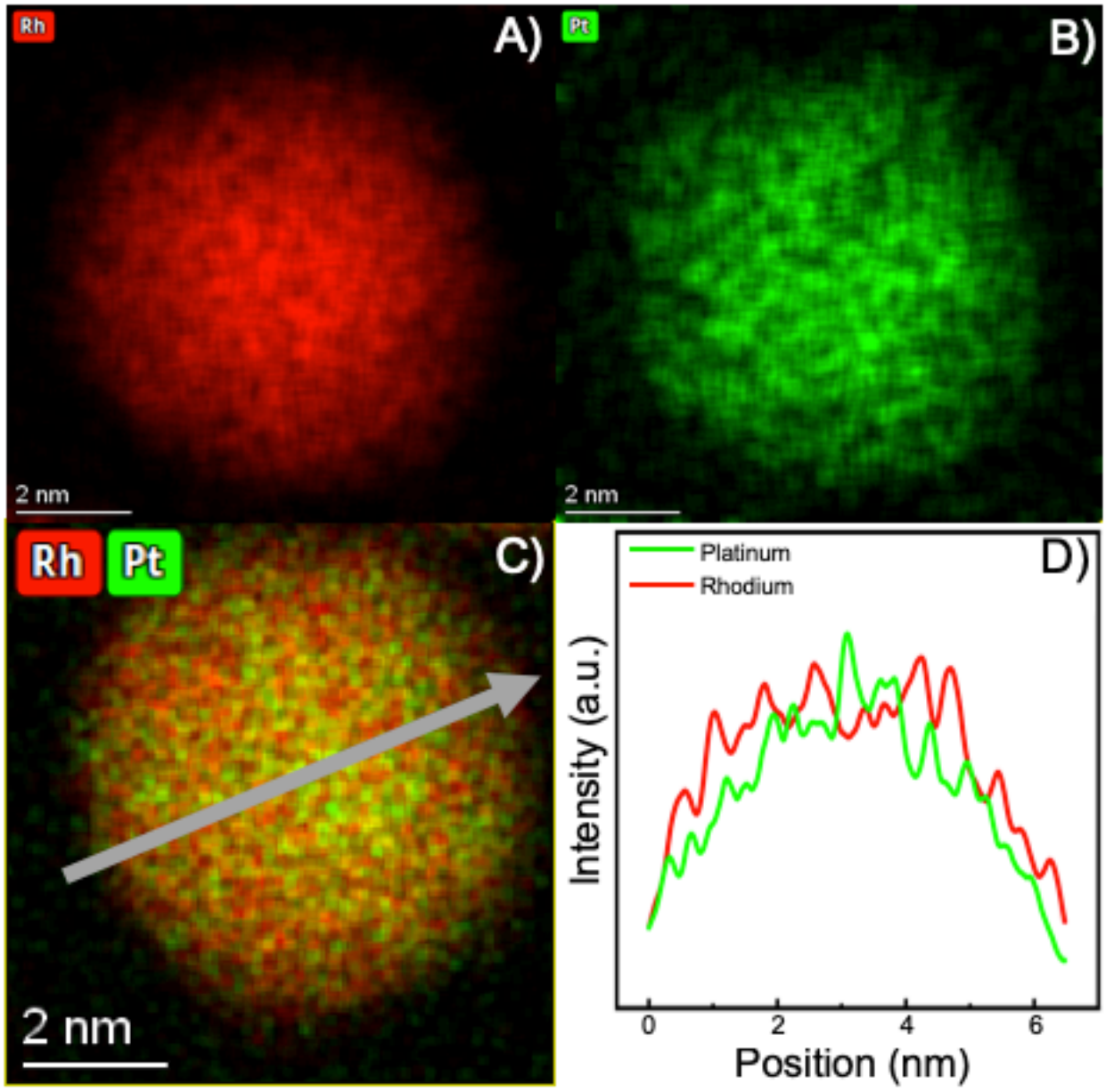

Figure 4.8: EDS map image of nanoparticles from Synthesis 10. A) Atomic distribution of Rh throughout the nanoparticle; B) Atomic distribution of Pt throughout the same nanoparticle shown in A); C) Atomic distribution of Pt and Rh throughout the nanoparticle with an arrow indicating the position and direction of the line scan; D) Line scan of the signal intensity of Pt and Rh for each position of the arrow from C). The signal for Rh is shown in red and for Pt in green.

Figure 4.9 shows a bright-field STEM image of the nanoparticles produced by Synthesis 10 (A), and a histogram of 250 nanoparticles from Synthesis 10 (B). The nanoparticles from Synthesis 10 appeared visually to have a broad size distribution (Figure 4.9A). This was confirmed upon measurement, with an average nanoparticle size of 8.4 ± 2.3 nm (Figure 4.9B).

To conclude, Synthesis 10 successfully produced homogeneous solid solution nanoparticles with a composition that approaches $Pt_{0.25}Rh_{0.75}$ (Figure 4.8 and Table 4.2). Yet, in order to study the activity and product selectivity as a function of nanoparticle stoichiometry, we needed to develop other compositions of solid solution Pt_xRh_{1-x}.

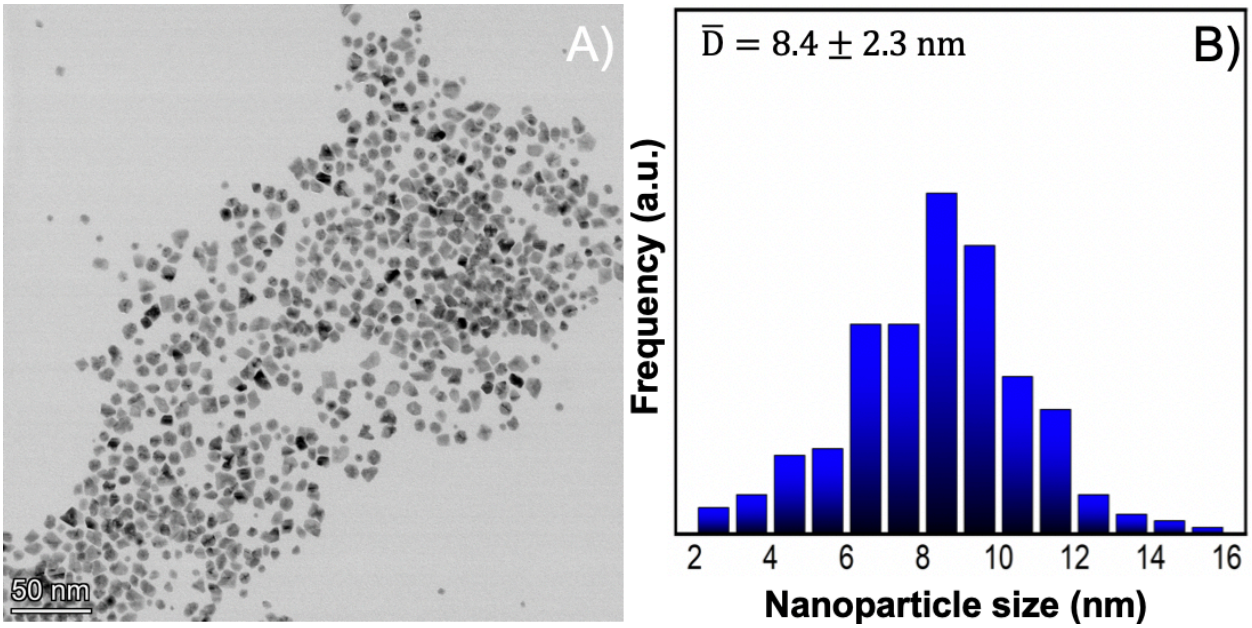

Figure 4.9: Size average and distribution for nanoparticles from Synthesis 10. A) Bright-field STEM image used for preparing histogram; B) Histogram showing the nanoparticles' size distribution.

To produce Pt_xRh_{1-x} nanoparticles with $x > 0.25$ we tried exploiting collision theory[111]. Collision theory states that reaction rates depend on the frequency of collisions from the reacting species. The frequency of collision can be increased by increasing the concentration of the reacting species. To test this theory in our system, Syntheses 11 and 12 were performed using the same experimental parameters as Synthesis 10 (Table 4.4). However, in Synthesis 11, the amount of Pt(acac)2 was increased by three-fold, and in Synthesis 12 by nine-fold. The products of the syntheses were prepared for STEM studies.

The first measurement was a composition analysis using EDS of an area containing over 1000 nanoparticles to obtain an average, followed by the measurement of five single nanoparticles. Table 4.3 is an overview of the stoichiometry of the products from Syntheses 11 and 12. The average composition for Synthesis 11 was 48 ± 3 % Pt and 52 ± 3 % Rh. For Synthesis 12, the average composition was 72 ± 13 % Pt and 28 ± 4 % Rh. The five individual nanoparticles for each synthesis appeared to display a representative composition, with error margins mostly overlapping with the larger samples (Table 4.3). However, again, the observed composition of the nanoparticles from both syntheses diverges from the nominal 75 atomic % Pt and 25 atomic % Rh for Synthesis 11 and 90 atomic % Pt and 10 atomic % Rh for Synthesis 12.

Table 4.3: EDS elemental composition of an area containing > 1000 nanoparticles and five single nanoparticles from Synthesis 11 and Synthesis 12. Nominal composition for the synthesis: 75 atomic % Pt and 25 atomic % Rh in Synthesis 11; 90 atomic % Pt and 10 atomic % Rh in Synthesis 12. Nominal composition refers to the amount of precursor used in the synthesis. NP, nanoparticle.

Synthesis 11	**Area with > 1000 NPs**	**NP 1**	**NP 2**	**NP 3**	**NP 4**	**NP 5**
Pt (atomic %)	48 ± 3	49 ± 8	45 ± 3	46 ± 3	45 ± 3	48 ± 8
Rh (atomic %)	52 ± 3	51 ± 7	55 ± 3	54 ± 3	55 ± 3	52 ± 7
Synthesis 12						
Pt (atomic %)	72 ± 13	69 ± 13	72 ± 14	73 ± 14	75 ± 2	80 ± 2
Rh (atomic %)	28 ± 4	31 ± 5	28 ± 4	27 ± 4	25 ± 2	20 ± 2

Next, we sought to analyze the homogeneity in element distribution of single particles from Syntheses 11 and 12 using an EDS map. Representative nanoparticles for Synthesis 11 are depicted in Figure 4.10 (A-C) and for Synthesis 12 (E-G), where the signal for Rh is shown in red and Pt in green. Figures 4.10A and E show that the Rh signal is most intense at the center and steadily decreases from the center toward the edges of the nanoparticles. Figure 4.10B and F depict the same nanoparticle, demonstrating that the signal for Pt follows the same pattern as that of Rh, with a more intense signal at the center and decreasing toward the edges. While for Figures 4.10A and

B, the signal for Pt and Rh appear to have comparable absolute intensities, the signal for Pt is more intense than that of Rh for E and F.

When superimposing the signal from Pt and Rh, the distribution of Pt and Rh appears to be uniform throughout the nanoparticle, and there is no clear Pt enrichment at the edges (Figure 4.10C, G). This is confirmed using a line scan displaying the signal for Pt and Rh for each position of the arrow in Figures C and G (Figure 4.10D, H). The line scan indicates a few areas where the system is rich in either Rh or Pt through the nanoparticle, an expected outcome in solid solution alloys (Methods and Theory 2.5 – Figure 2.10). Yet, the distribution of Pt and Rh appears homogeneous throughout the nanoparticle, indicating that a solid solution system has been achieved.

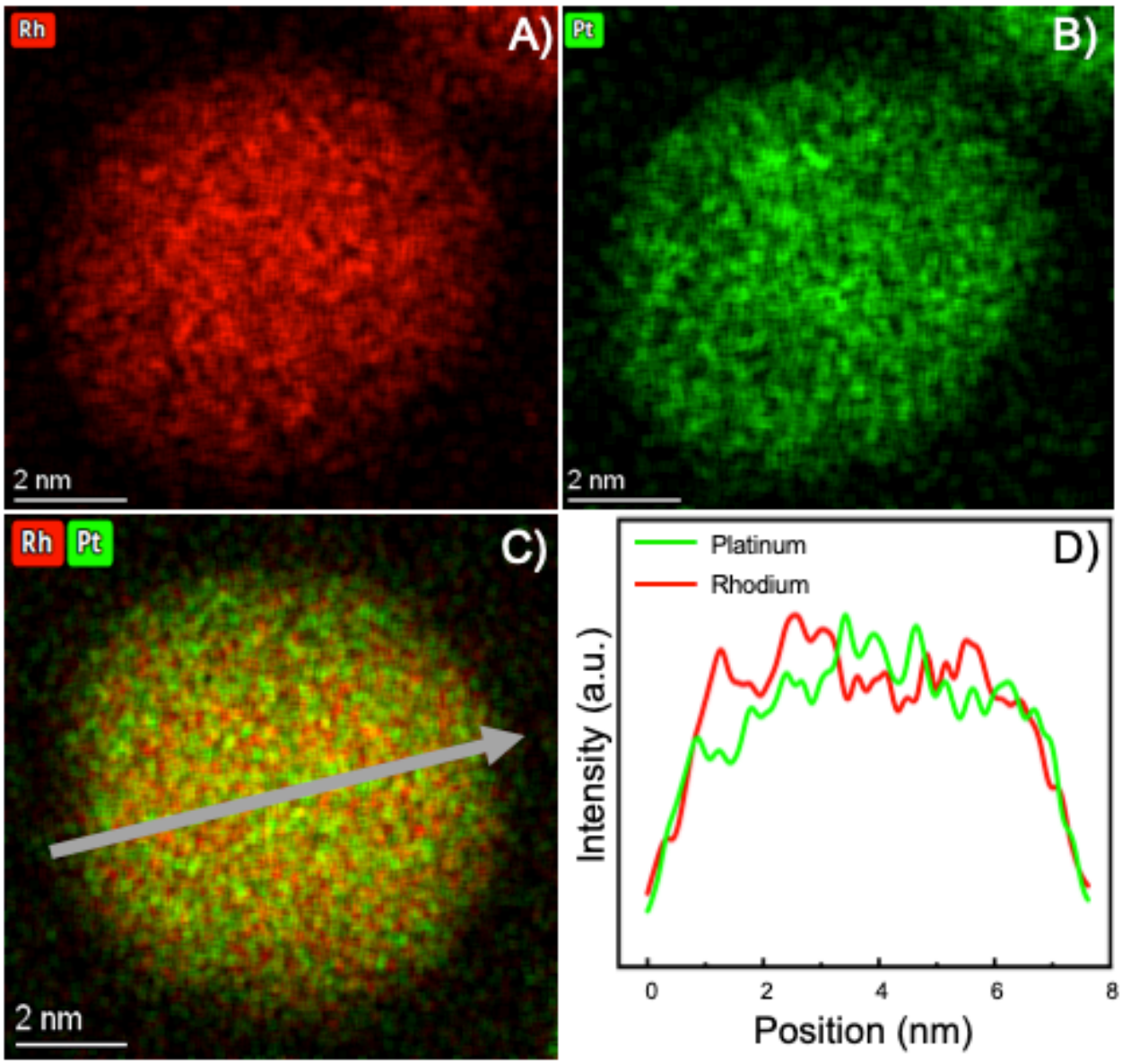

Figure 4.10: EDS map image of nanoparticles from Syntheses 11 and 12. Synthesis 11: A-D. A) Atomic distribution of Rh throughout the nanoparticle; B) Atomic distribution of Pt throughout the same nanoparticle shown in A); C) Atomic distribution of Pt and Rh throughout the nanoparticle with an arrow indicating the position and direction of the line scan; D) Line scan of the signal intensity of Pt and Rh for each position of the arrow from C). The signal for Rh is shown in red and for Pt in green.

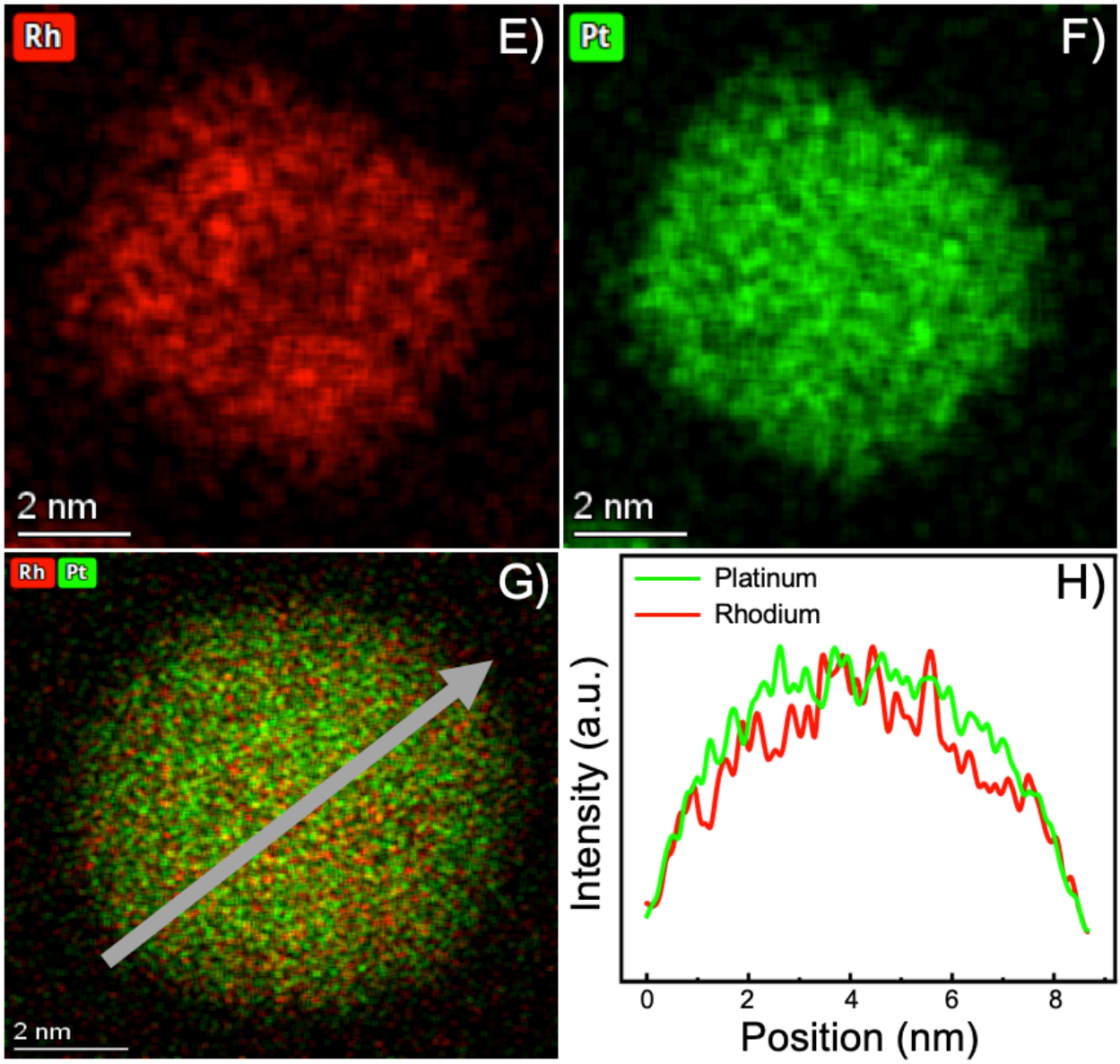

Figure 4.10 (Continuation): EDS map image of nanoparticles from Syntheses 11 and 12. Synthesis 12: E-H. E) Atomic distribution of Rh throughout the nanoparticle; F) Atomic distribution of Pt throughout the same nanoparticle shown in E); G) Atomic distribution of Pt and Rh throughout the nanoparticle with an arrow indicating the position and direction of the line scan; D) Line scan of the signal intensity of Pt and Rh for each position of the arrow from G). The signal for Rh is shown in red and for Pt in green.

Figure 4.11 shows bright-field STEM images of the nanoparticles from Syntheses 11 (A) and 12 (B), as well as histograms of 250 nanoparticles from Syntheses 11 (B) and 12 (D). The average size of the nanoparticles was 7.1 ± 1.8 nm for Synthesis 11, and 6.9 ± 1.5 nm for Synthesis 12.

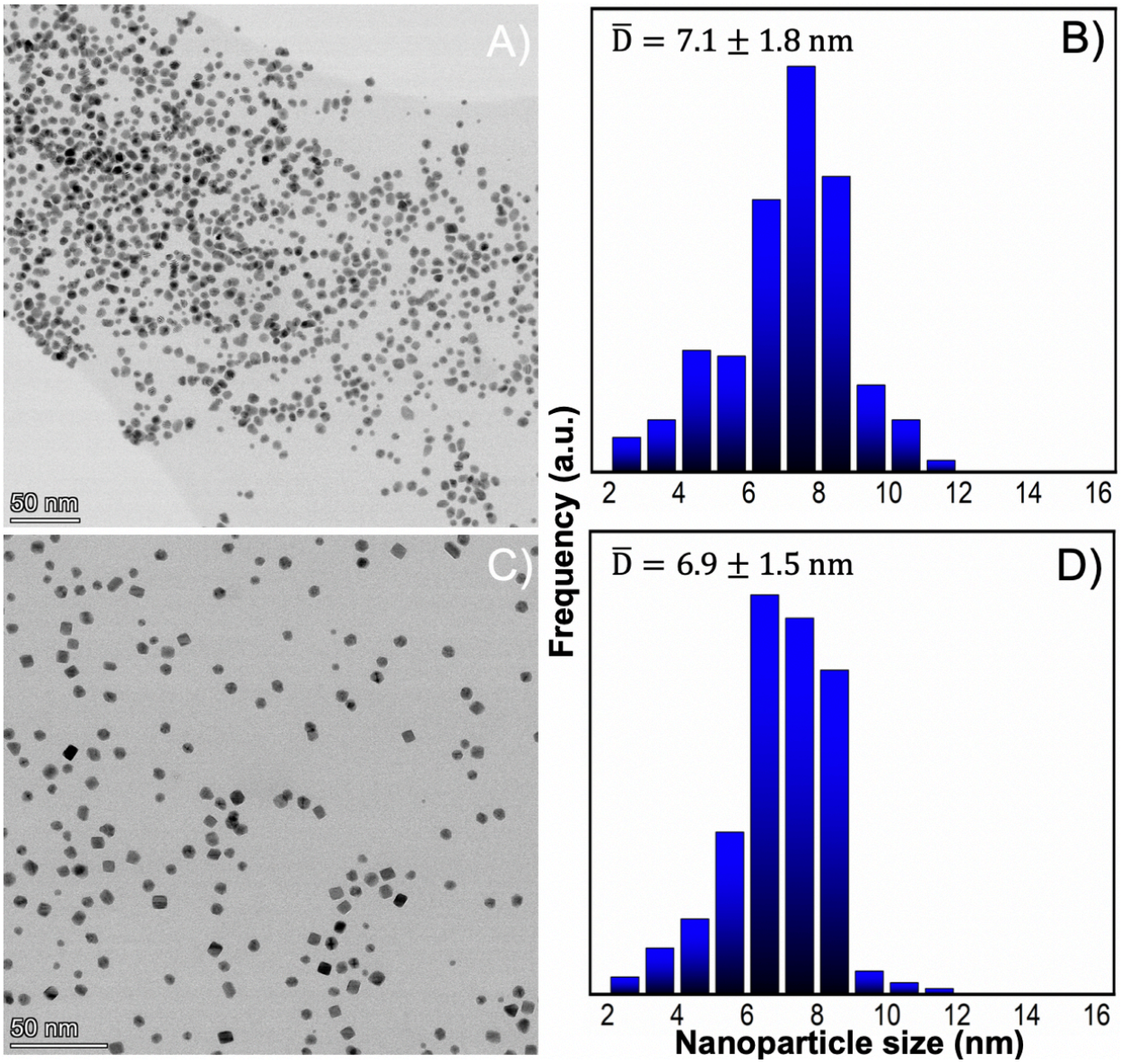

Figure 4.11: Size average and distribution for nanoparticles from Syntheses 11 and 12. A) Bright-field STEM image of nanoparticles from Synthesis 11 used for preparing histogram; B) Histogram showing the nanoparticles' size distribution from Synthesis 11; C) bright-field STEM image of nanoparticles from Synthesis 12 used for preparing histogram; D) Histogram showing the nanoparticles' size distribution from Synthesis 12.

To conclude, Syntheses 10-12 successfully produced Pt_xRh_{1-x} nanoparticles in solid solution configuration (Figure 4.8 and Figure 4.10). Quenching the reaction before the slower reacting $Pt(acac)_2$ was fully consumed avoided the formation of a Pt-enriched shell. Since the kinetics for the reduction of $Pt(acac)_2$ to Pt^0 is slower than that of $Rh(acac)_3$ to Rh^0, the relative composition

of Pt and Rh in the nanoparticles could be tuned by adjusting the ratio of the $Pt(acac)_2$ to $Rh(acac)_3$ precursors used for each synthesis. In Synthesis 10, equimolar amounts of $Pt(acac)_2$ and $Rh(acac)_3$ were used, resulting in nanoparticles with a configuration that approaches $Pt_{0.25}Rh_{0.75}$ (Table 4.2). In Syntheses 11 and 12, the concentration of $Rh(acac)_3$ was kept constant, while the concentration of $Pt(acac)_2$ was increased by three- and nine-fold, respectively. As a result, nanoparticles with solid solution configurations approaching $Pt_{0.50}Rh_{0.50}$ were produced by Synthesis 11, and $Pt_{0.75}Rh_{0.25}$ by Synthesis 12 (Table 4.3).

Yet, the EDS MAP is a technique that characterizes only a fraction of the population of nanoparticles produced. Therefore, we wanted to examine the products of Syntheses 10, 11, and 12 by inductively coupled plasma-optical emission spectrometry (ICP-OES) for composition analysis, which analyzes the entire sample. In addition, we wanted to examine the solid solution status by PXRD and extrapolate the composition of the nanoparticles using variations in unit cell dimensions extracted by PXRD and by the application of Vegard's law (Methods and Theory 2.8.3).

Table 4.4: Summary of syntheses for preparation of solid solution Pt_xRh_{1-x} nanoparticles. PVP, polyvinylpyrrolidone; EG, ethylene glycol. Nominal composition refers to the amount of precursor used in the synthesis.

Synthesis	**$Pt(acac)_2$** **mg** **mmol** **mM**	**$Rh(acac)_3$** **mg** **mmol** **mM**	**PVP** **mg** **mmol**	**EG** **mL**	$\frac{\mathbf{n(PVP)}}{\mathbf{n(precursors)}}$	**Temp** **°C**	**Duration** **minutes**	**Nominal composition**	**Measured composition**	**Solid solution**
9	117 0.30 15	40 0.10 5	222 2.0	20	5	195	120	$Pt_{0.75}Rh_{0.25}$	$Pt_{0.75}Rh_{0.25}$	No
10	39 0.10 5	40 0.10 5	222 2.0	20	10	195	15	$Pt_{0.50}Rh_{0.50}$	$Pt_{0.25}Rh_{075}$	Yes
11	117 0.30 15	40 0.10 5	222 2.0	20	5	195	15	$Pt_{0.75}Rh_{0.25}$	$Pt_{0.50}Rh_{0.50}$	Yes
12	351 0.90 45	40 0.10 5	222 2.0	20	2	195	15	$Pt_{0.90}Rh_{0.10}$	$Pt_{0.75}Rh_{0.25}$	Yes

4.1.2.4 Inductively coupled plasma - optical emission spectrometry analysis and powder X-ray diffraction of the solid solution nanoparticles

To measure the average stoichiometry of the produced Pt_xRh_{1-x} nanoparticles, in a way that was representative of the whole sample, an ICP-OES measurement was performed. The nominal and measured Pt/Rh ratio in nanoparticles obtained by Syntheses 10, 11, and 12 are presented in Table 4.5. The ICP-OES data indicates that only a fraction of the added Pt precursor reacted during the syntheses, as the nominal composition is higher than the measured composition.

Table 4.5: Nominal and measured composition of the solid solution nanoparticles measured by ICP-OES for Syntheses 10, 11, and 12. Nominal composition refers to the amount of precursor used in the synthesis.

Synthesis	**Nominal composition Pt/Rh (atomic %)**	**Measured composition Pt/Rh (atomic %)**
10	$\frac{50}{50}$	$\frac{26.6 \pm 0.1}{73.4 \pm 0.1}$
11	$\frac{75}{25}$	$\frac{52.2 \pm 0.5}{47.8 \pm 0.5}$
12	$\frac{90}{10}$	$\frac{74.6 \pm 0.4}{25.4 \pm 0.4}$

In order to further verify that the produced nanoparticles from syntheses 10, 11, and 12 were in the solid solution configuration, PXRD data were collected by following the procedure outlined in Experimental (3.5). The PXRD for the products of the three syntheses is reported in Figure 4.12, depicting diffraction patterns with broad Bragg reflections that correspond to a single ccp phase. As mentioned in Introduction (1.4), both Pt and Rh have ccp-type crystal structures. Therefore, a single ccp phase indicates the atomic mixing of Pt and Rh. In addition, a shift from higher to lower 2θ values of the Bragg reflections occurs from Synthesis 10 to Synthesis 11 and from Synthesis 11 to Synthesis 12, an expected result as Pt has a larger atomic radius that leads to a larger unit cell than Rh (Introduction 1.4 – Table 1.2 and 1.3).

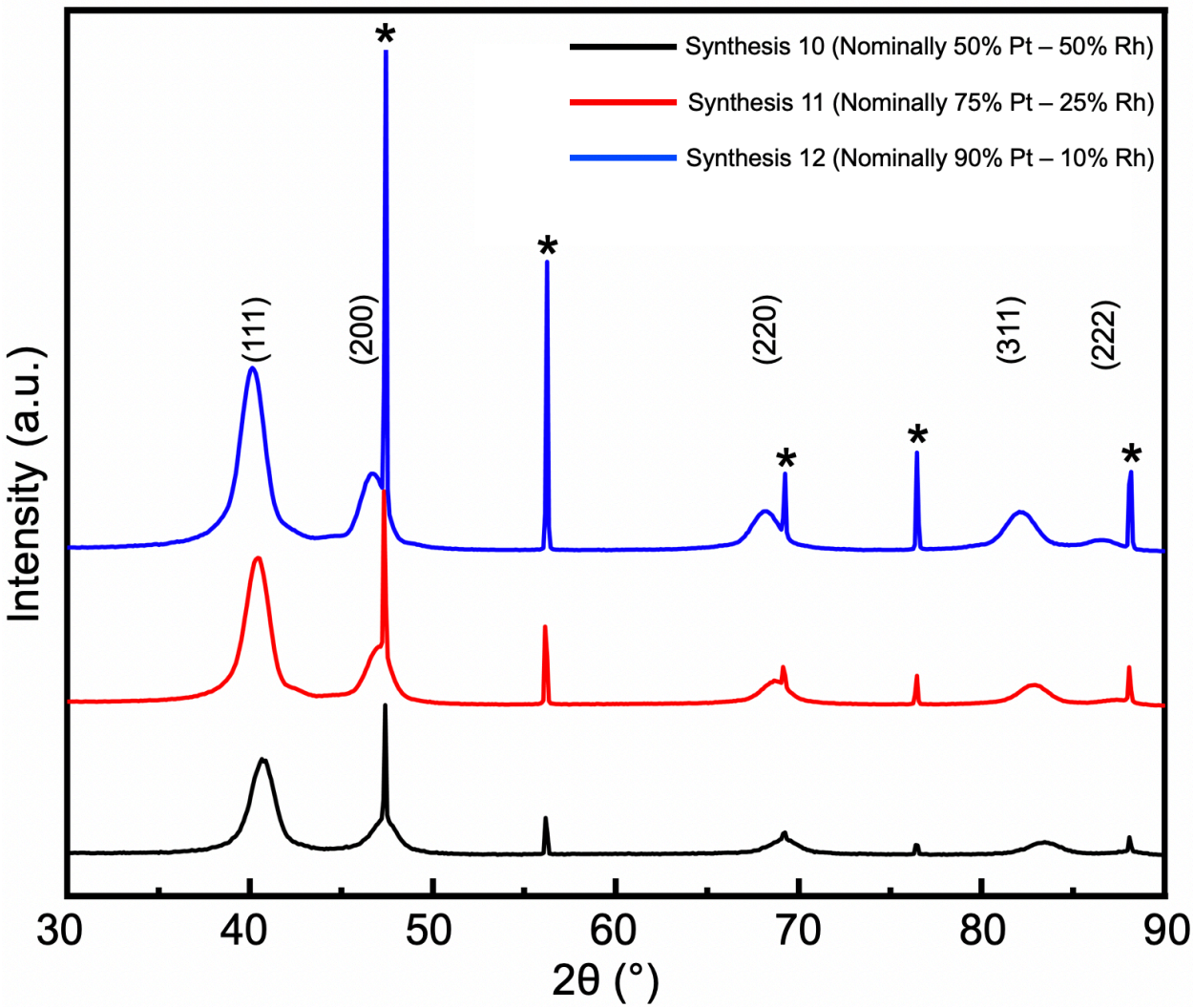

Figure 4.12: Powder X-ray diffraction patterns of the product from Synthesis 10 in (nominal composition: 50 % Pt and 50% Rh; black line), Synthesis 11 (nominal composition: 75 % Pt and 25% Rh; red line), and Synthesis 12 (nominal composition: 90 % Pt and 10% Rh; blue line). The peaks signalized with a (*) correspond to Bragg reflections from the National Institute of Standards and Technology Si standard.

Rietveld refinements of the PXRD diffractograms presented in Figure 4.12 were performed as described in the Experimental (3.5) to calculate the nanoparticles' a-axis dimension. For detailed Rietveld refinement results, refer to Appendix – Figure A.2. The a-axis of the products was 3.8467 ± 0.0009 Å for Synthesis 10, 3.8691 ± 0.0002 Å for Synthesis 11, and 3.8962 ± 0.0002 Å for Synthesis 12 (Table 4.6). The margin of error was based on theoretical calculations performed using TOPAS[103]. We observed an expansion in the unit cell dimension with increasing Pt precursor in the synthesis (Table 4.4). Using the refined a-axis values and the a-axes measured for pure Rh

and Pt nanoparticles produced using a similar technique, the ratio of Pt to Rh from each synthesis was estimated by applying Vegard's law (Methods and Theory 2.8.3). The products of Synthesis 10 were estimated at 25.95 ± 0.02 % Pt – 74.05 ± 0.02 % Rh; Synthesis 11 at 47.70 ± 0.01 % Pt – 52.30 ± 0.01 % Rh; and of Synthesis 12 at 74.00 ± 0.01 % Pt – 26.00 ± 0.01 % Rh (Table 4.6). The uncertainty was calculated using the uncertainty from the a-axis extracted by PXRD from Syntheses 10 to 12.

In Figure 4.13, the refined a-axis values of the different nanoparticle compositions were plotted against the composition of the nanoparticles obtained by ICP-OES. For monometallic Pt and Rh nanoparticles, the a-axis reported were measured from nanoparticles prepared by similar syntheses procedures[112]. A linear fit for the plot was then obtained, yielding the equation $y = -0.103x + 3.922$, and the R^2 value of the linear regression was estimated at 0.998. The high R^2 is a strong indication that the unit cell dimensions of the nanoparticles follow Vegard's law (Methods and Theory 2.8.3). From the equation of the line, the obtained a-axis by Rietveld refinement was used to calculate the percentage of Rh relative to Pt in the nanoparticles. The products of Synthesis 10 contained 26.9 % Pt and 73.1 % Rh, Synthesis 11 contained 48.7 % Pt and 51.3 % Rh, and Synthesis 12 contained 75.0 % Pt and 25.0 Rh (Table 4.6).

Table 4.6: Unit cell a-axis dimension obtained by Rietveld refinements, nanoparticle composition estimated by Vegard's law, nanoparticle composition from the equation of the line (Figure 4.13), and nominal composition for Syntheses 10, 11, and 12. Nominal composition refers to the amount of precursor used in the synthesis.

Synthesis	**Unit cell a-axis dimension from Rietveld refinement**	**Composition from Vegard's law Pt/Rh (atomic %)**	**Composition from the equation of the line (Figure 4.13) Pt/Rh (atomic %)**	**Nominal composition Pt/Rh (atomic %)**
10	3.8467 ± 0.0009 Å	$\frac{25.95 \pm 0.02}{74.05 \pm 0.02}$	$\frac{26.9}{73.1}$	$\frac{50}{50}$
11	3.8691± 0.0002 Å	$\frac{47.70 \pm 0.01}{52.30 \pm 0.01}$	$\frac{48.7}{51.3}$	$\frac{75}{25}$
12	3.8962 ± 0.0002 Å	$\frac{74.00 \pm 0.01}{26.00 \pm 0.01}$	$\frac{75.0}{25.0}$	$\frac{90}{10}$

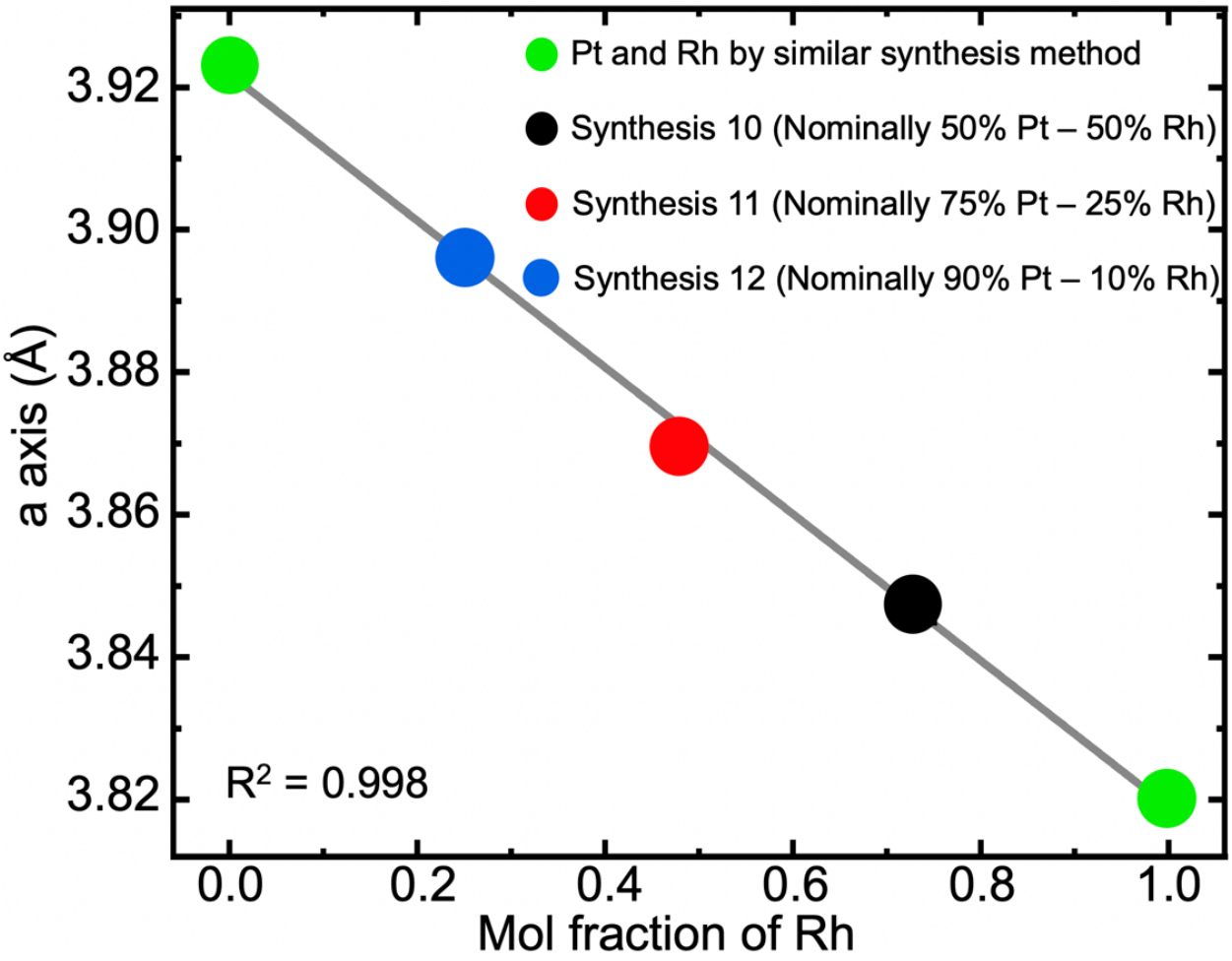

Figure 4.13: Refined a-axis values of the X-ray diffraction data of the various nanoparticle compositions (Table 4.6) plotted against the mole fraction of Rh (normalized to Pt and Rh), obtained from ICP-OES analysis. Green, monometallic Pt and Rh nanoparticles synthesized by similar methods; black, Nanoparticles from Synthesis 10 (nominal composition: 50 % Pt and 50% Rh); red, nanoparticles for synthesis 11 (nominal composition: 75 % Pt and 25% Rh; red line); blue, nanoparticles from synthesis 12 (nominal composition: 90 % Pt and 10% Rh; blue line).

4.1.3 Summary and concluding remarks

Results 4.1.2.3 presents a synthesis design for producing nanoparticles in the solid solution configuration. The design considers that $Rh(acac)_3$ reacts faster than $Pt(acac)_2$. When both reactants are allowed to react for two hours, a solid-solution core and a Pt-enriched shell form (Figure 4.7). When the reactants are quenched after 15 minutes, solid solution nanoparticles without a shell are produced (Figures 4.8 and 4.10). In addition, the composition of the

nanoparticles can be controlled by adjusting the ratio of Pt to Rh precursors. When the ratio of 50 % $Pt(acac)_2$ – 50 % $Rh(acac)_3$, 75 % $Pt(acac)_2$ – 25 % $Rh(acac)_3$, and 90 % $Pt(acac)_2$ – 10 % $Rh(acac)_3$, are used, nanoparticles with a composition that approaches $Pt_{0.25}Rh_{0.75}$, $Pt_{0.50}Rh_{0.50}$, and $Pt_{0.75}Rh_{0.25}$ were produced, respectively (Table 4.7). The composition of the nanoparticles obtained by EDS, ICP-OES, and Vegard's law are comparable (Table 4.7). The nominal mol fraction of Rh was plotted against the mol fraction of Rh in the produced nanoparticles from Syntheses 10, 11, and 12, where the end-points "0" represents a synthesis with only $Pt(acac)_2$ and "1" a synthesis with only $Rh(acac)_3$. An exponential regression produced the curve $y = 1.112(1 - e^{-2.299x})$ with an estimated R^2 of 0.999 (Figure 4.14). From the equation of the curve, one can estimate the ratio of precursors needed in order to obtain a nanoparticle's desired outcome. In summary, quenching the reaction before the slower precursor is completely consumed produces homogeneous nanoparticles in the solid solution configuration and the nanoparticle composition can be tuned by varying the ratio of precursors in the synthesis.

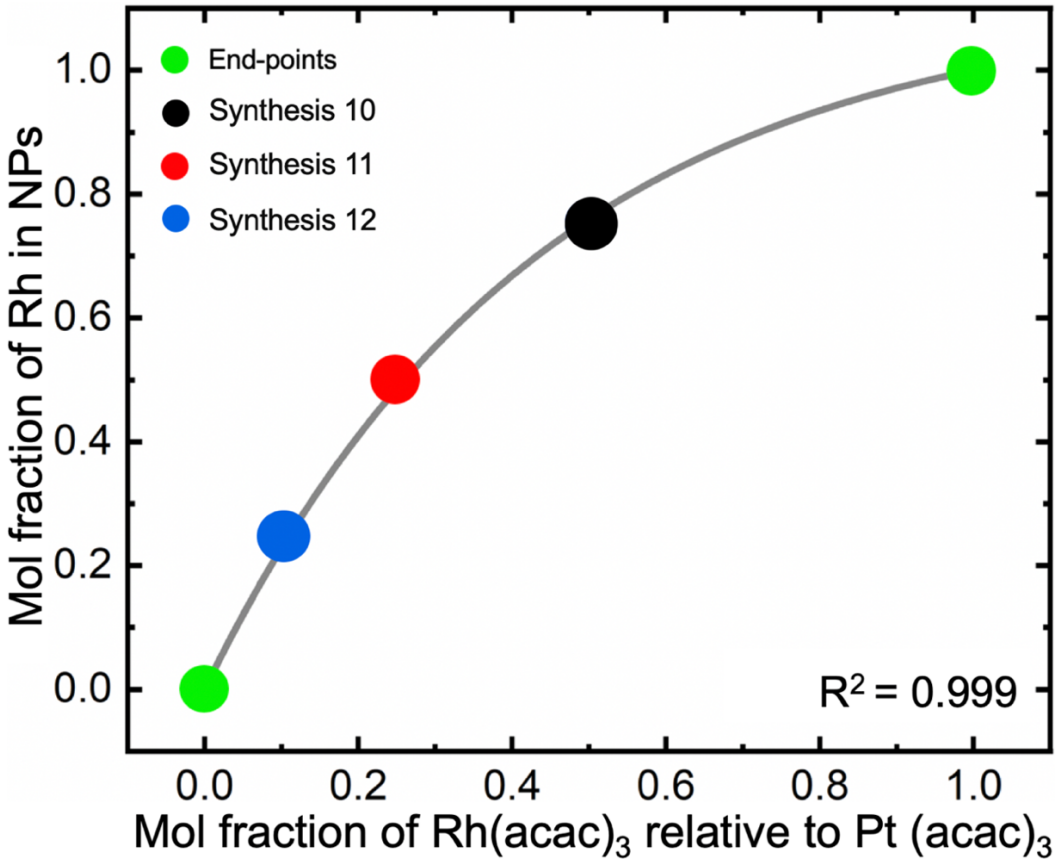

Figure 4.14: Exponential regression of the nominal mol fraction of $Rh(acac)_3$ used for syntheses versus mol fraction of Rh in the nanoparticle. The equation of the curve is $y = 1.112(1 - e^{-2.299x})$.

Table 4.7: Summary of results listing the average EDS, ICP-OES, Vegard's law, equation of the line composition, average size, and unit cell dimensions from Rietveld refinement of the produced nanoparticles. Nominal composition refers to the amount of precursor used in the synthesis. EDS, energy-dispersive X-ray spectroscopy; ICP-OES, inductively coupled plasma - optical emission spectrometry; NP, nanoparticles.

Synthesis	Nominal composition (Pt/Rh in atomic %)	EDS (Pt/Rh in atomic %)	ICP-OES (Pt/Rh in atomic %)	Vegard's law (Pt/Rh in atomic %)	Equation of the line from the plot in Figure 4.13 (Pt/Rh in atomic %)	The average size of the NPs	a-axis dimension
10	$^{50}/_{50}$	$\frac{24 \pm 2}{76 \pm 2}$	$\frac{26.6 \pm 0.1}{73.4 \pm 0.1}$	$\frac{25.95 \pm 0.02}{74.05 \pm 0.02}$	$\frac{26.9}{73.1}$	8.4 ± 2.3 nm	3.8467 ± 0.0009 Å
11	$^{75}/_{25}$	$\frac{48 \pm 3}{52 \pm 3}$	$\frac{52.2 \pm 0.5}{47.8 \pm 0.5}$	$\frac{47.70 \pm 0.01}{52.30 \pm 0.01}$	$\frac{48.7}{51.3}$	7.1 ± 1.8 nm	3.8691± 0.0002 Å
12	$^{90}/_{10}$	$\frac{72 \pm 13}{28 \pm 4}$	$\frac{74.6 \pm 0.4}{25.4 \pm 0.4}$	$\frac{74.00 \pm 0.01}{26.00 \pm 0.01}$	$\frac{75.0}{25.0}$	6.9 ± 1.5 nm	3.8962 ± 0.0002 Å

4.2 Development of well-defined Pt/Al_2O_3 and $Pt_{0.50}Rh_{0.50}/Al_2O_3$ catalysts

4.2.1 Preparation of Al_2O_3 as support for colloidally synthesized nanoparticles

The dynamics between reactants, intermediate species, and product(s) in catalyzed chemical reactions can only be understood through well-defined model catalyst systems. Thus, we sought to develop metal-on-support catalysts by first synthesizing free-standing metallic nanoparticles and subsequently depositing them onto Al_2O_3 support, following the concept outlined in Methods and Theory 2.7.

The first step for preparing the support component of the catalyst was to calcinate alumina (boehmite) powder at 900 °C for 10 hours (Experimental 3.4.1), as performed by Muri[28]. After calcination, a powder X-ray diffractogram of the product was collected according to the procedure in Experimental 3.5.

Figure 4.15 reports the obtained PXRD of the boehmite before and after calcination. By inspecting the obtained PXRD in the EVA software in combination with a database[106], it was established that the starting material contained boehmite (COD 9012275), whereas, in the calcined sample, a mixture of the crystalline phases of γ- (COD 2015530), η-Al_2O_3 (COD 2107301), and the θ-Al_2O_3 (COD 2107302) were detected. The γ- and η-Al_2O_3 phases were detected as they have nearly identical peak positions. On the other hand, when boehmite is calcinated at 900 °C, a mixture of gamma γ- and θ-crystalline phases of Al_2O_3 form[113]. In contrast, the formation of η-Al_2O_3 can be ruled out as it comes from the calcination of bayerite[113]. Therefore, it can be concluded that the calcinated powder contained γ- and θ-Al_2O_3.

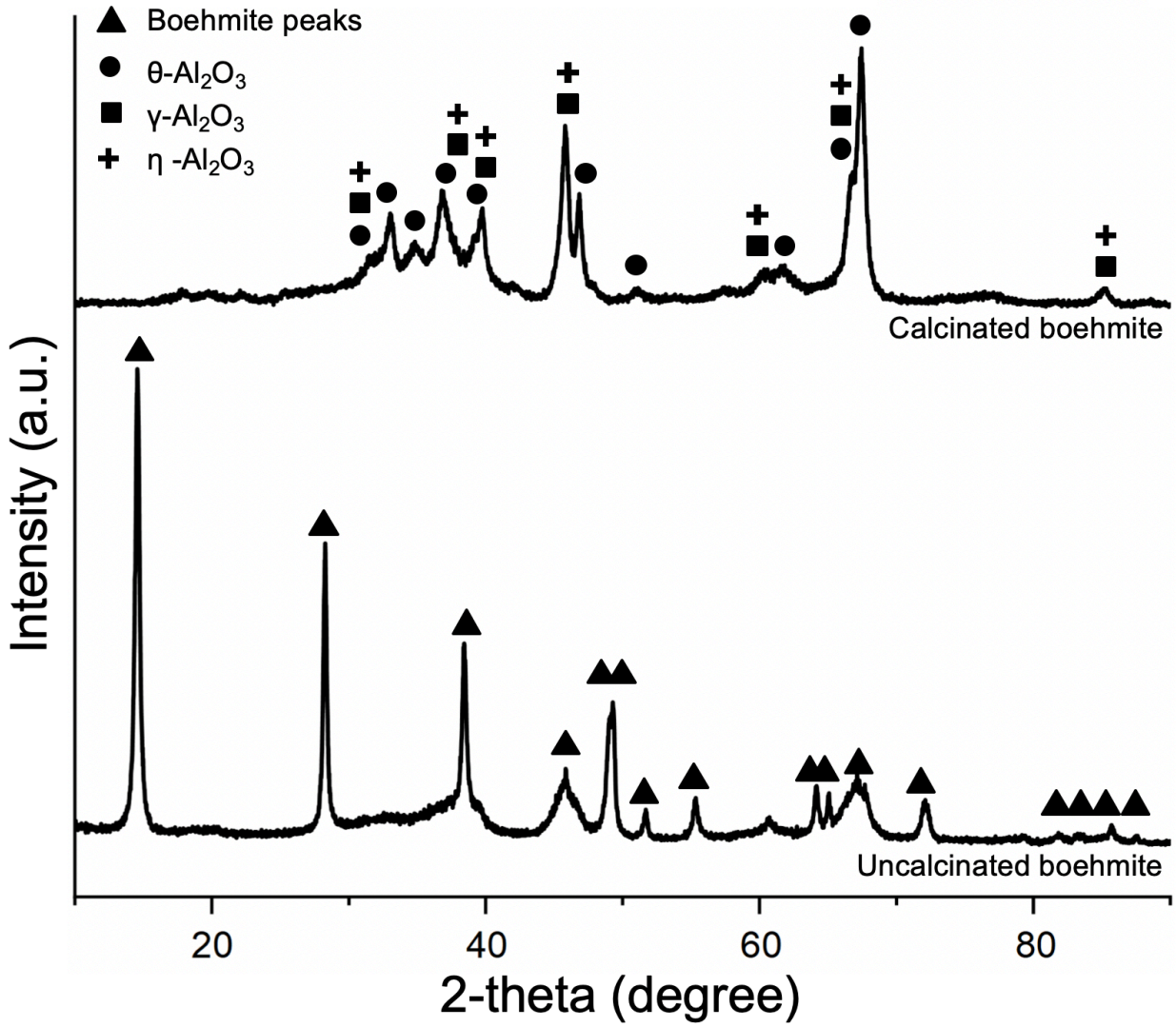

Figure 4.15: Powder XRD diffraction patterns before and after the boehmite Al_2O_3 powder calcination at 900 °C for 12 hours. Triangle is the signal for boehmite, circle for θ-, square for γ-, and cross for η-Al_2O_3. The η-Al_2O_3 phase was detected as it has nearly identical peak positions to γ- Al_2O_3, but its presence in the sample has been ruled out.

4.2.2 Benchmarking the deposition of Pt nanoparticles on Al_2O_3 support

In order to prepare the well-defined catalyst systems, Pt nanoparticles were synthesized by following a procedure developed by Muri[28]. In Synthesis 13, 0.75 mmol of PVP and 0.075 mmol of $Pt(acac)_2$ were dissolved in 20 mL 1,4-butanediol. The synthesis was initiated by raising the temperature of the solution to 220 °C. The synthesis duration was two hours. For more details regarding the synthesis, see Experimental 3.3.4 and Table 4.9.

Synthesis 13 was washed to separate the nanoparticles from 1,4-butanediol by following the procedure described in Experimental 3.3.6. The nanoparticles were then redispersed in 30 mL methanol. Aiming for 0.5 weight % Pt/Al_2O_3 and assuming 70% Pt yield as achieved by Eirini et al.[114], 2.03 g of Al_2O_3 support was dispersed in 70 mL methanol in a beaker under magnetic stirring. Then, the methanol solution containing the Pt nanoparticles was transferred dropwise into the beaker containing the Al_2O_3 support under stirring. Upon completion, a sample for high-resolution SEM imaging was collected. For a detailed description of the deposition, see Experimental 3.4.2.

Figure 4.16 presents representative high-resolution SEM images using low angle backscattered electron mode of Pt nanoparticles from Synthesis 13 deposited on Al_2O_3 support. As a note, backscattered electron imaging makes heavier elements appear brighter as they scatter more electrons than light atoms (Methods and Theory 2.8.1). Figure 4.16A shows an overview of the sample, revealing bright clusters in the alumina matrix indicated by red arrows. Upon magnification, the clusters appear to be composed of agglomerated nanoparticles (Figure 4.16B). Thus, the production of the catalyst systems was halted for troubleshooting.

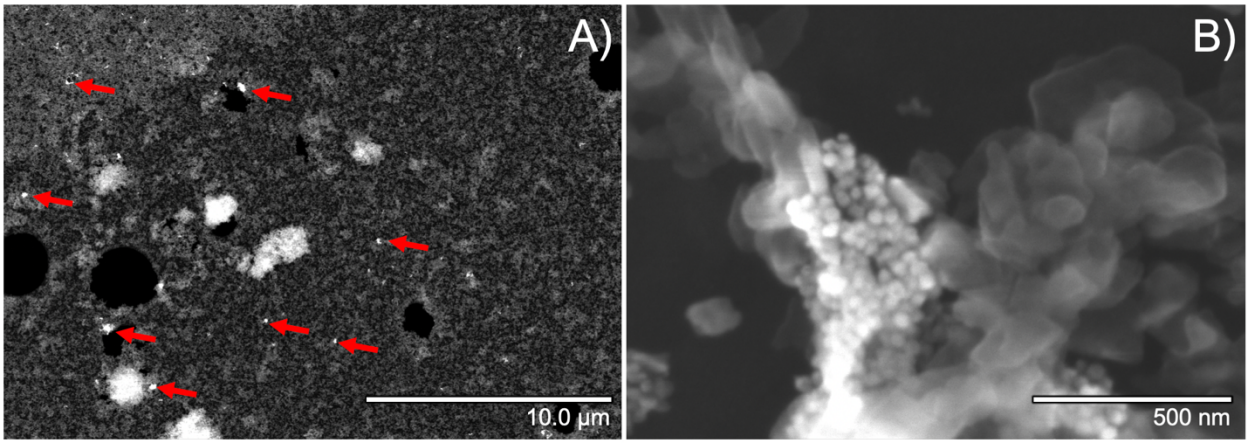

Figure 4.16: High-resolution SEM images using low angle backscattered electron mode for imaging the Pt nanoparticles deposited on Al_2O_3 for Synthesis 13. A) Overview of the sample, red arrows indicating bright clusters; B) Magnified image of one cluster from A).

4.2.3 Defining optimal deposition conditions for well-dispersed Pt nanoparticles on Al_2O_3

As the procedure produced agglomerated nanoparticles on the support[28], the focus turned to developing a new approach for producing well-dispersed Pt and solid solution $Pt_{0.50}Rh_{0.50}$

nanoparticles supported onto Al_2O_3. The solid-solution nanoparticles were included in the development program as a change in the metal composition and solvent may alter the chemistry of the particle's surface. Furthermore, we sought to develop a method that could be applied to any composition of bimetallic Pt-Rh nanoparticles.

We had two hypotheses for the agglomeration of the nanoparticles: 1) The nanoparticles agglomerated during the washing-, redispersion-, and deposition procedure. 2) The nanoparticles agglomerated during synthesis.

4.2.3.1 Testing hypothesis 1: "The nanoparticles agglomerate during the washing-, redispersion-, and deposition procedure," using replicates of Synthesis 13

In order to test the first hypothesis, certain variables were tested, such as the sonication method, the addition of extra surfactant during redispersion, sonication time, and solvents. Other variables, such as solvent volume and the amount of Al_2O_3, were kept constant. Table 4.8 describes the parameters used for deposition of the nanoparticles after the washing procedure. After deposition, the Pt on Al_2O_3 was prepared for high-resolution SEM following the procedure outlined in Experimental 3.4.2. Figure 4.17 presents high-resolution SEM images using low angle backscattered electron mode of Pt nanoparticles deposited on Al_2O_3 for each trial parameter described in Table 4.8.

In Experiment 1, we sought to test whether sonication would help the redispersion of the nanoparticles (Table 4.8). The products of Synthesis 13 were sonicated for 1 hour, and the Al_2O_3 powder was sonicated for 30 minutes. The nanoparticles were added to the Al_2O_3 suspension dropwise under constant stirring. A sample of the catalyst was then prepared for high-resolution SEM. Figure 4.17A shows that the produced Pt nanoparticles were agglomerated in micrometer-sized clumps.

We concluded that a possible reason for the agglomeration was insufficient strength from the sonication bath to redisperse the nanoparticles after being flocculated during the washing procedure. Therefore, experiment 2 used the same parameters as Experiment 1, except that the sonication bath was substituted with a sonication probe at max strength for five minutes for both nanoparticles and Al_2O_3 (Table 4.8). The nanoparticles were added to the Al_2O_3 suspension under sonication. The sonication probe has higher power than the sonication bath, as the source of the

ultrasonic waves is in direct contact with the methanol solution containing the nanoparticles. However, upon high-resolution SEM imaging, the deposited nanoparticles were still agglomerated in micrometer-sized clumps (Figure 4.17B).

We concluded that a possible reason for the persistent agglomeration is that the surfactant may be washing out from the nanoparticles' surface during the washing procedure. To address this issue, Experiment 3 used the same parameters as Experiment 2, but 84 mg PVP, the same amount of PVP used for Synthesis 13 (Table 4.9), was added to the suspension of nanoparticles before sonication (Table 4.8). However, the deposited nanoparticles were still agglomerated in micrometer-sized clumps upon high-resolution SEM imaging (Figure 4.17C).

We then sought to examine whether the agglomeration was due to insufficient sonication time to break the nanoparticles loose. Thus, for Experiment 4, the same parameters as Experiment 3 were used, but the sonication time for the nanoparticle suspension was increased from 5- to 30 minutes (Table 4.8). Figure 4.17D shows that the deposited nanoparticles were still agglomerated in micrometer size clumps upon high-resolution SEM imaging, but the aggregates appeared smaller than in Figure 4.17A-C.

As a consequence, we decided to further increase the sonication time. For Experiment 5, the same parameters as Experiment 4 were used, but the sonication time for the nanoparticle suspension was increased from 30 minutes to 120 minutes (Table 4.8). However, the deposited nanoparticles were still agglomerated in micrometer size clumps upon high-resolution SEM imaging (Figure 4.17E). In fact, the increase in sonication time from 30 to 120 minutes appeared to have no effect on agglomeration.

As a last attempt at testing hypothesis 1, we sought to use a different solvent in order to examine whether methanol was causing the nanoparticles to agglomerate. For Experiment 6, the same parameters as Experiment 4 were used, but isopropanol was used as a solvent for redispersion of the nanoparticles (Table 4.8). As is shown in Figure 4.17F, the nanoparticles remained agglomerated upon high-resolution SEM imaging. After testing key variables from the washing, redispersion, and deposition procedure, the nanoparticles were still agglomerated. For that reason, we moved on to testing the hypothesis that the nanoparticles were agglomerating during the synthesis.

Table 4.8: Redispersion and deposition parameters tested to obtain well-dispersed Pt nanoparticles on Al_2O_3 using the products of Synthesis 13[5]. NP, nanoparticles; RPM, rotations per minute.

Experiment	**Deposition conditions**	**a) Sonication method** **b) Sonication time for nanoparticles** **c) Sonication time for Al_2O_3**	**Mixing conditions**	**Result**
1	Nanoparticles: redispersed in 30 mL methanol Al_2O_3: dispersed in 70 mL methanol	a) Sonication bath b) 60 min at max strength c) 30 min at max strength	Under stirring at 250 RPM	Figure 4.17A Agglomerated NPs.
2	Same as Experiment 1	a) Sonication probe b) 5 min at max strength c) 5 min at max strength	Under sonication	Figure 4.17B Agglomerated NPs.
3	Nanoparticles: redispersed in 30 mL methanol containing 0.75 mmol PVP Al_2O_3: Same as Experiment 1	Same as Experiment 2	Same as Experiment 2	Figure 4.17C Agglomerated NPs.
4	Same as Experiment 1	a) and c) same as Experiment 2 b) 30 min at max strength	Same as Experiment 2	Figure 4.17D Agglomerated NPs.
5	Same as Experiment 1	a) and c) same as Experiment 2 b) 120 min at max strength	Same as Experiment 2	Figure 4.17E Agglomerated NPs.
6	Nanoparticles: redispersed in 30 mL isopropanol Al_2O_3: dispersed in 70 mL isopropanol	Same as Experiment 4	Same as Experiment 2	Figure 4.17F Agglomerated NPs.

[5] Experiments 1-6 use replicates of **Synthesis 13,** outlined in Table 4.9. The variables modified were type of sonication, sonication time and type of solvent used to test whether the listed parameters would affect the dispersion of the nanoparticles.

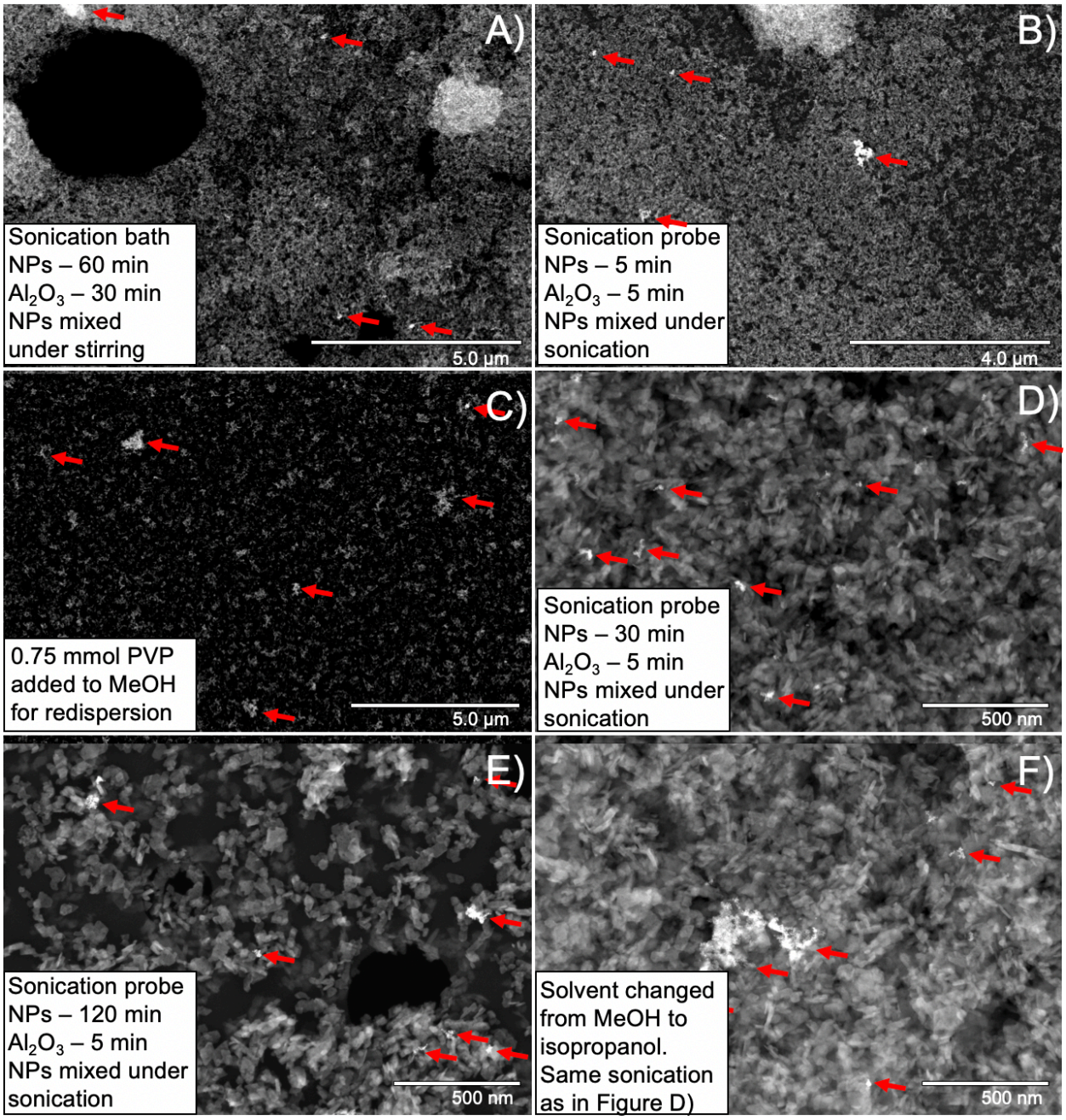

Figure 4.17 High-resolution SEM images using low angle backscattered electron mode of Pt nanoparticles deposited on Al_2O_3 to test whether the nanoparticles agglomerated during the washing-, redispersion-, and deposition procedure. A) Experiment 1; B) Experiment 2; C) Experiment 3; D) Experiment 4; E) Experiment 5; F) Experiment 6.

4.2.3.2 Testing hypothesis 2: "The nanoparticles agglomerate during the synthesis"

Experiments 1-6 did not resolve the agglomeration issue (Table 4.8). Therefore, we carried out an experiment to follow the products of a replicate of Synthesis 13 as a function of reaction time (Table 4.9). For the experiment, an aliquot of the products from Synthesis 13 was removed every five minutes from 0 to 55 minutes. The aliquots were then directly deposited on a TEM grid.

The results from the SEM imaging taken in bright-field STEM mode are presented in Figure 4.18. Before Synthesis 13 started (at 0 minutes), no particles were present in the TEM grid. During the first 15 minutes of the synthesis, we observed no agglomeration. Then, from 20 to 25 minutes, we began to observe some agglomerates and dispersed nanoparticles, and after 25 min, there was widespread agglomeration of the nanoparticles (Figure 4.18).

Notably, the agglomeration process occurred in parallel with nanoparticle growth, which increases the total surface area of metal in solution. Thus, we believed that the agglomeration could have occurred due to low steric hindrance because of insufficient surfactant (PVP) in the solution to adequately cover the surface of the nanoparticles (Methods and Theory 2.2).

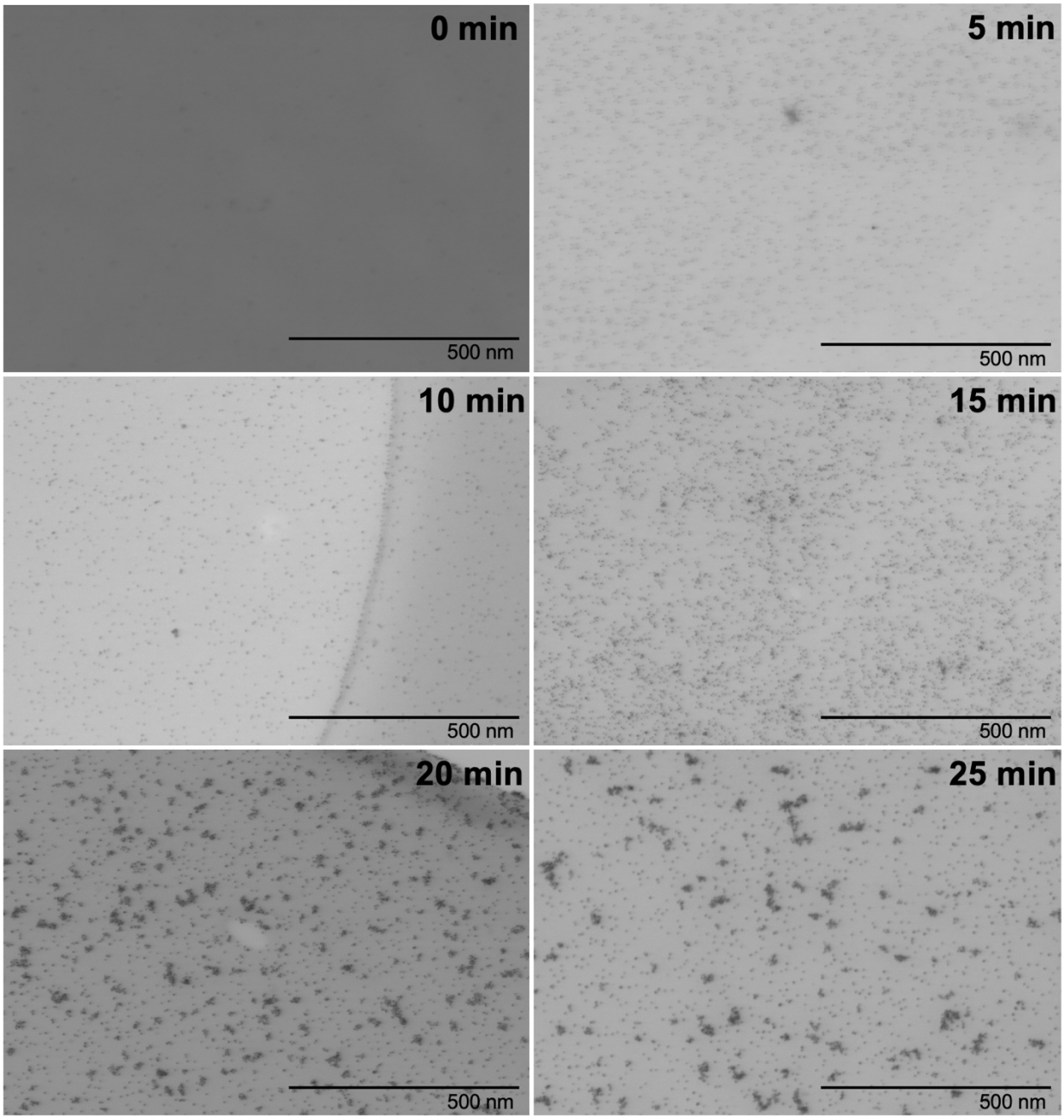

Figure 4.18: High-resolution SEM images in bright-field STEM mode of the products of a replicate of Synthesis 13 with 5-minute intervals.

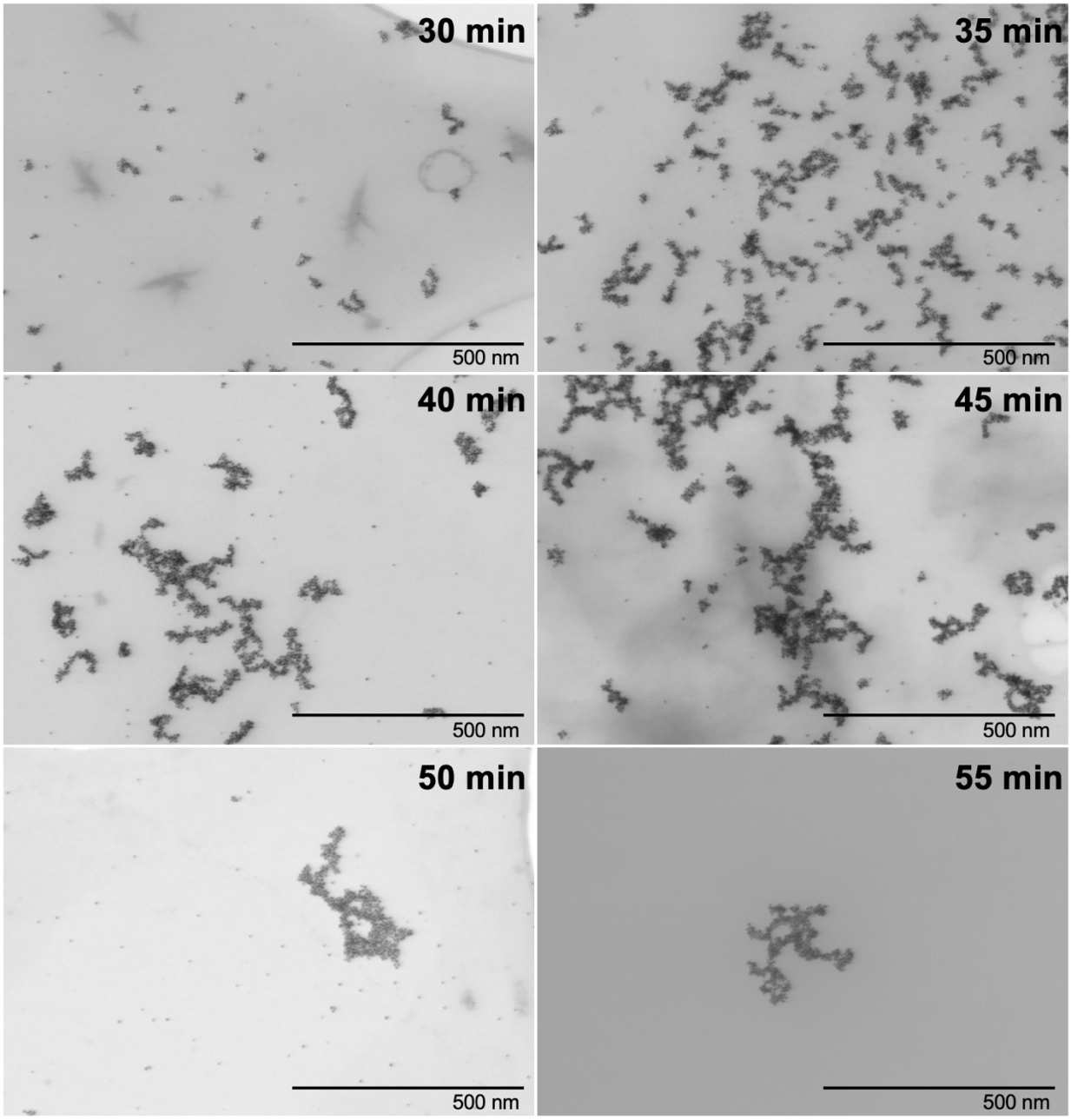

Figure 4.18 (Continuation): High-resolution SEM images in bright-field STEM mode of the products of a replicate of Synthesis 13 with 5-minute intervals.

In order to test whether the nanoparticles were aggregating due to lack of surfactant (PVP), we performed Synthesis 14 with three-fold, and Synthesis 15 with nine-fold, the original amount of PVP (Table 4.9). After the syntheses, the nanoparticles were imaged using high-resolution SEM (Figure 4.19A, B).

Upon SEM imaging analysis in the bright-field STEM mode, Synthesis 14 appeared to produce a few non-agglomerated nanoparticles with small, scattered agglomerates in between (Figure 4.19A). However, Synthesis 15 did not produce any agglomerates (Figure 4.19B). Thus, we concluded that the nanoparticles were agglomerating during synthesis due to low steric hindrance (Methods and Theory 2.2), and that hypothesis 2 was correct.

Before continuing with the production of the catalysts, it was essential to test whether the critical parameter for producing non-agglomerated Pt nanoparticles is the PVP/metal ratio or the molar concentration of PVP in 1,4-butanediol solution. We, therefore, performed Syntheses 16 and 17 (Table 4.9). In Synthesis 16, the amount of $Pt(acac)_2$ and PVP were the same as in Synthesis 15, keeping the same n(PVP)/n(precursor) ratio, while the volume of 1,4-butanediol was increased three-fold. For Synthesis 17, the amount of $Pt(acac)_2$ and the PVP concentration in the solution were kept the same as in Synthesis 15 by increasing the volume of 1,4-butanediol together with the amount of PVP by three-fold (Table 4.9). After the syntheses, the nanoparticles were studied using high-resolution SEM (Figure 4.19C, D).

Figure 4.19C is an image in the bright-field STEM mode of the products of Synthesis 16, displaying agglomerated nanoparticles. Synthesis 17, however, did not produce any agglomerates (Figure 4.19D), thus demonstrating that the molar concentration of PVP in 1,4-butanediol is the crucial parameter for producing non-agglomerated nanoparticles. If the solution contains 338 mM PVP (Table 4.9), the nanoparticles will not agglomerate.

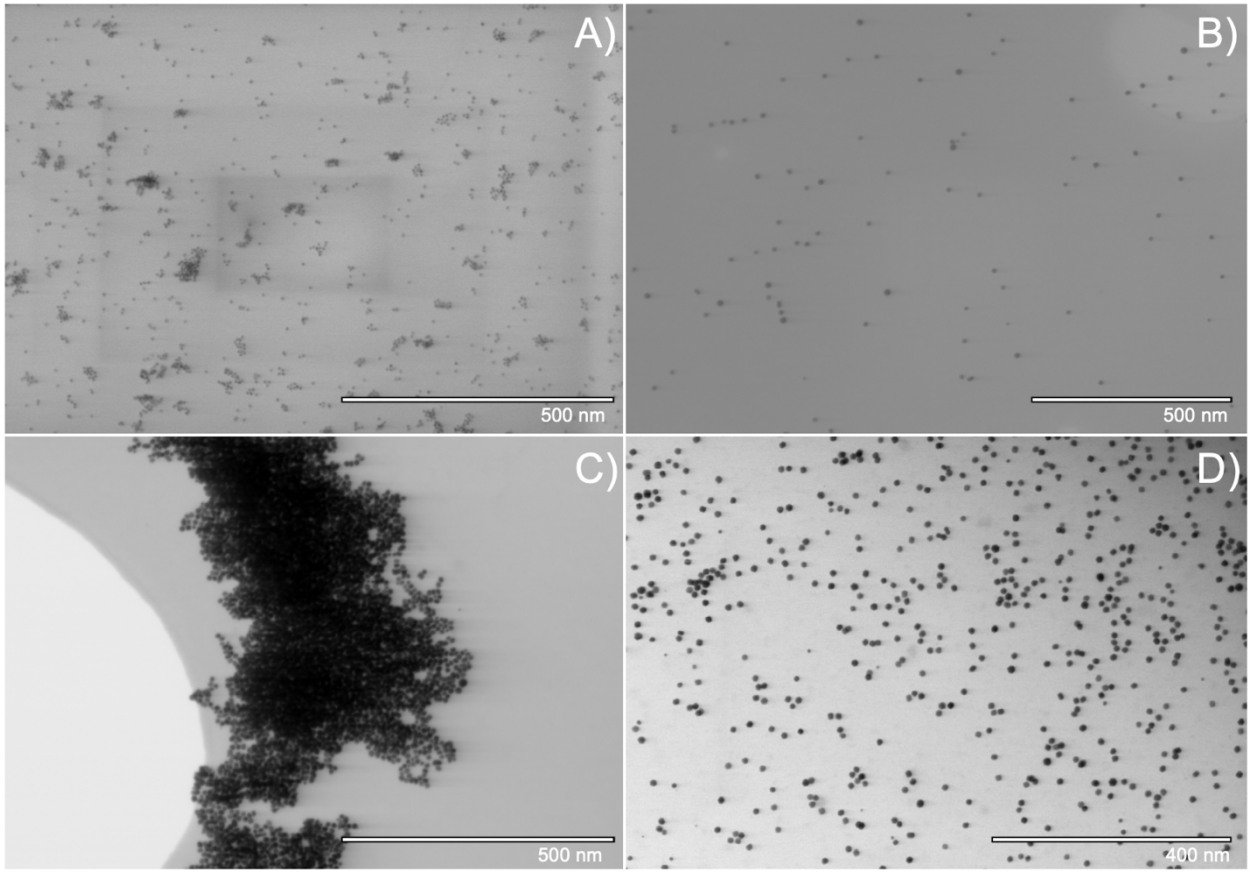

Figure 4.19: High-resolution SEM images in the bright-field STEM mode of products from Syntheses 14-17. A) Synthesis 14; B) Synthesis 15; C) Synthesis 16; D) Synthesis 17.

4.2.4 Preparation of well-defined Pt and $Pt_{0.50}Rh_{0.50}$ catalysts

Next, we sought to test whether the new synthesis strategy could be applied to the $Pt_{0.50}Rh_{0.50}$ solid solution nanoparticles. The synthesis is performed in a different solvent, ethylene glycol, so there's a change in the chemical environment. In addition, the change in the metal composition could alter the chemistry of the nanoparticle's surface.

It must be noted that Synthesis 18 parameters are different from Synthesis 11 from Results 4.1.2. For Synthesis 18, the amount of PVP was adjusted to 338 mM to produce non-agglomerated nanoparticles, and the concentration of $Pt(acac)_2$ and $Rh(acac)_3$ was reduced when compared to Synthesis 11 (Results 4.1.2 – Table 4.4). The concentration of metal was reduced to produce nanoparticles having a narrower size distribution by avoiding multiple nucleation events during the synthesis (Methods and Theory 2.1.2 and 2.1.3). After the synthesis, the nanoparticles were washed as described in Experimental 3.3.6 and redispersed in 30 mL methanol. A sample was then

taken for high-resolution SEM imaging, and Synthesis 18 was taken for EDS map studies in a transmission electron microscope.

In order to produce the catalysts, the pure Pt nanoparticles were prepared using the parameters outlined for Synthesis 15 and the solid solution nanoparticles as outlined for Synthesis 18 (Table 4.9). Aiming for 0.5 weight % metal/Al_2O_3 and assuming 70 % Pt yield as achieved by Eirini et al.[114], 2.03 g of Al_2O_3 was used for depositing the products of Synthesis 15. For Synthesis 18, the synthesis was quenched after 15 minutes to avoid the formation of a Pt-rich shell. Because the reaction time was relatively short, 35 % Rh reduction and an equimolar amount of Pt were assumed, and 1.06 g of Al_2O_3 was used to deposit the nanoparticles. The particles were deposited to Al_2O_3 using the procedure described in Results 4.2.2. The system was then calcinated at 400 °C for 8 hours under synthetic airflow, and then a sample was taken for high-resolution SEM microscopy. Figure 4.20 contains high-resolution SEM images using the bright-field STEM mode of the Pt nanoparticles from Synthesis 15 (A) and the solid solution $Pt_{0.50}Rh_{0.50}$ nanoparticles from Synthesis 18 (B). Neither synthesis produced agglomerated nanoparticles. The nanoparticles from Synthesis 18 were in a solid solution, despite the modifications in the synthesis method (Figure A.1 - Appendix), containing 51 ± 3 atomic % Pt and 49 ± 3 atomic % Rh as measured by EDS.

To explore the dispersion of the nanoparticles after deposition onto Al_2O_3, the synthesized products were analyzed using high-resolution SEM images on low angle backscattered electron mode. After calcination at 400 °C, neither Pt nanoparticles (Figure 4.20C), nor the solid solution $Pt_{0.50}Rh_{0.50}$ nanoparticles (Figure 4.20D), displayed agglomerated or sintered nanoparticles. Next, we measured nanoparticle size and found that the average size was 7.5 ± 0.8 nm for the Pt nanoparticles (Figure 4.20E), and 7.4 ± 1.6 nm the solid solution $Pt_{0.50}Rh_{0.50}$ nanoparticles (Figure 4.20F). Thus, the average size was similar, but the solid solution $Pt_{0.50}Rh_{0.50}$ nanoparticles had a broader size distribution. Lastly, the metal loading of the catalysts was analyzed using ICP-OES, as metal loading is an important indicator of catalyst activity. We found that the metal loading was 0.56 % for the Pt nanoparticles and 0.61 % for the solid solution $Pt_{0.50}Rh_{0.50}$. The obtained metal loading was 11% higher for the Pt nanoparticles than that obtained by Muri (ref) and 18% higher than estimated for the solid solution $Pt_{0.50}Rh_{0.50}$ (Table A.1 – Appendix). However, as the measurement was only performed once, we don't know if the metal loading results are reproducible.

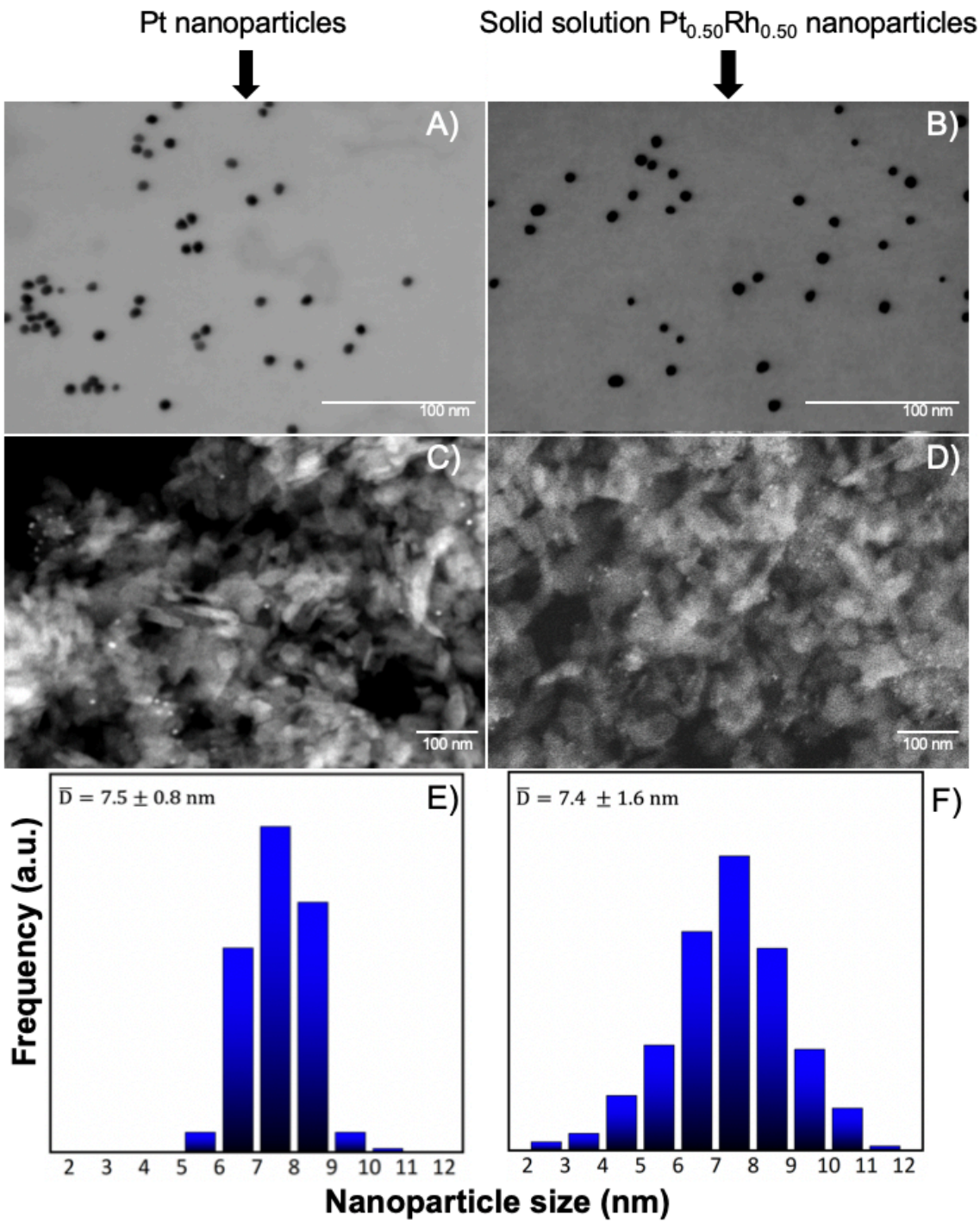

Figure 4.20: Qualitative and quantitative analyses of Syntheses 15 and 18. High-resolution SEM images in the bright-field STEM mode of A) Pt nanoparticles and B) solid solution $Pt_{0.50}Rh_{0.50}$ nanoparticles; High-resolution SEM picture on low angle backscattered electron mode of calcinated C) Pt nanoparticles deposited on Al_2O_3 and D) solid solution $Pt_{0.50}Rh_{0.50}$ nanoparticles deposited on Al_2O_3; Size and size distribution of E) Pt nanoparticles and F) solid solution $Pt_{0.50}Rh_{0.50}$ nanoparticles.

Table 4.9 Synthesis parameters for developing non-agglomerated Pt nanoparticles (Syntheses 13-17). Syntheses 15 and 18 were used for producing the Pt and solid solution $Pt_{0.50}Rh_{0.50}$ nanoparticles supported on Al_2O_3, respectively. PVP, polyvinylpyrrolidone).

Synthesis	**$Pt(acac)_2$ (mg) (mmol)**	**$Rh(acac)_3$ (mg) (mmol)**	**PVP (mg) (mmol)**	**Solvent (mL)**	$\frac{\mathbf{n(PVP)}}{\mathbf{n(precursors)}}$	**[PVP] (mM)**	$\sum(Pt + Rh)$ **(mM)**	**Temp (°C)**	**Duration (hours)**	**Metal loading (weight %)**[6]
13[7]	29.4 0.075	-	84 0.75	1,4-butanediol 20	10	38	3.75	220	2	N/A
14	29.4 0.075	-	252 2.25	1,4-butanediol 20	30	113	3.75	220	2	N/A
15	29.4 0.075	-	756 6.75	1,4-butanediol 20	90	338	3.75	220	2	N/A
16	29.4 0.075	-	756 6.75	1,4-butanediol 60	90	113	1.25	220	2	N/A
17	29.4 0.075	-	2268 20.25	1,4-butanediol 60	270	338	1.25	220	2	0.56
18	59 0.15	20 0.05	2268 20.25	ethylene glycol 60	101	338	3.33	195	2	0.61

[6] Measured by inductively coupled plasma atomic emission spectroscopy

[7] After the first synthesis (Results 4.2.2), six replicates of Synthesis 13 were prepared for testing whether the nanoparticles were agglomerating due the washing-, redispersion- and deposition procedure (Table 4.8). A seventh replicate was prepared to study the products of the reaction as a function of time (Results 4.2.2).

4.3 Measuring the thermal stability of the solid solution $Pt_{0.50}Rh_{0.50}$ nanoparticles by in situ scanning transmission electron microscopy

The phase diagram for the Pt and Rh system (Introduction 1.3 and Figure 1.6) predicts that when in bulk, an alloy that contains 50 atomic % Pt and 50 atomic % Rh exist in two segregated phases up to 760 °C[30]. However, in this thesis we report the synthesis of $Pt_{1-x}Rh_x$ solid solution nanoparticles (Results 4.1.2). Based on this finding, we sought to find the thermodynamically stable configuration of the as-synthesized Pt_xRh_{1-x} (x = 0.5) nanoparticles as function of temperature in UHV. We limit the temperature variations to the range from 25 to 600 ºC, as these nanoparticles are intended to be used as catalysts in the selective catalytic oxidation of ammonia to nitrogen gas (Introduction 1.3)[15].

To study whether and how these solid solution nanoparticles change as a function of temperature and time in a vacuum, a pre-screening was done by *in situ* STEM using the Protochips® Fusion system (Experimental 3.6.1). In the context of this experiment, *in situ* refers to measurements done while the sample is at the target temperature. When interpreting the data performed *in situ* at high temperatures, it is important to take the beam effects into account (Methods and Theory 2.8.2). For that reason, we firstly studied the beam effect as a function of the temperature (Results 4.3.1) and then the temperature effect on the element distribution dynamics of the nanoparticles (Results 4.3.2). The nanoparticles were synthesized by replicating Synthesis 11 (Table 4.4 – Results 4.1.2.3). After the synthesis, the sample was pre-evaluated by SEM. The nanoparticles had the expected morphology and size distribution (confirmed by STEM, Figure 4.23 (*left)*). The sample was prepared for *in situ* STEM by drop casting a colloidal dispersion of the sample in methanol onto the fusion heating chip (Experimental 3.3.6). Before the measurements, no attempts were made to remove PVP from the nanoparticles' surface. It has been previously established that surfactants are removed from the nanoparticle's surface at high temperature *in situ* TEM experiments in UHV[46]. Thus, it was assumed that PVP would not change the experiment's outcome.

4.3.1 The role of the electron dosage as a function of temperature in the solid solution $Pt_{0.50}Rh_{0.50}$ nanoparticles

The electron beam may damage the sample when bimetallic nanoparticles are studied *in situ* at high temperatures using electron microscopes (Methods and Theory 2.8.2). The beam effect might also be a function of temperature itself[95]. For that reason, the effect of beam exposure must be *decoupled* from the temperature effect in the dynamics of element distribution. We, therefore, established a protocol for the *in situ* STEM experiment for interpreting dynamics in the element distribution as a function of time, temperature, and beam exposure. The beam dosage is measured qualitatively, where a small beam dosage is defined as the *first*-, and a large beam dosage as the *las*t 50 EDS frames. The effect of beam exposure is shown by superimposing the images of the *first*- and *last* 50 EDS maps frames. The HAADF image of the *first*- and *last* EDS frame was also obtained to support the EDS map. Importantly, the contrast in HAADF images is sensitive to the atomic number, causing heavier elements to appear brighter (Methods and Theory 2.8.2)

The experiment measured the nanoparticles' atomic distribution at room temperature to establish a baseline. The temperature was instantly raised to 600 °C, and the atomic distribution of the nanoparticles was measured *in situ*. Finally, the sample was cooled down to 300 °C, and the atomic distribution of the nanoparticles was measured *in situ*. The nanoparticles had not been exposed to the electron beam prior to measurement.

Figure 4.21 shows representative nanoparticles from at least ten different measurements at A) 25 °C before heating, B) 90 minutes at 600 °C, C) 210 minutes at 600 °C, D) 30 minutes at 300 °C, and E) 60 min at 300 °C. The signal for Rh is presented in red and for Pt in green. The top left images of Figure 4.21A-E display the first 50 superimposed EDS map frames, which show that the signal for Pt and Rh are well distributed within the nanoparticles. The top right images display the HAADF image of the first EDS map frame and support the EDS result, showing a gradual contrast transition from the edges (less bright) to the center (brightest) of the nanoparticles.

The bottom left images display the *last* 50 superimposed EDS map frames, and the bottom right images display the HAADF image of the *last* EDS frame. For the nanoparticles in Figure 4.21A, D, and E, the signal for Pt and Rh appear evenly distributed as a solid solution in the nanoparticles. Moreover, the HAADF image of the *last* EDS frame shows a smooth transition of contrast from the edges to the center of the nanoparticles. In contrast, the EDS map indicates that the signal for

Pt and Rh is segregated in disparate areas for the nanoparticles in Figure 4.21B and C. This is confirmed by the HAADF images of the *last* EDS frame, as the signal for Pt is predominant in the bright areas of the EDS map.

We also measured the nanoparticles' size and composition (atomic %; Figure 4.21). In images containing more than one nanoparticle, the reported data is from the nanoparticle with an arrow crossing its perimeter. The size of the nanoparticles was measured based on the HAADF image and the composition reported from the *first* and *last* 50 frames were within the margins of error. Notably, the nanoparticles measured *in situ* at both 300- and 600 °C increased in size (Figure 4.21B, C, D).

To conclude, we found that beam damage of the sample occurs at 300 °C, resulting in nanoparticle growth, and at 600 °C resulting in both nanoparticle growth and element segregation. The first 50 frames of all nanoparticles measured *in situ STEM*, independent of exposure time to the target temperature, have the same configuration as the baseline. The goal of the *in situ* STEM experiments is to extract information about the temperature dependence on elemental distribution dynamics without influence from the electron beam. We found that a suitable method for analyzing the data is to use only the first 50 frames of the HAADF and EDS map images during the *in situ* STEM experiments at 300 and 600 °C. If executed accordingly, the measurements will not show changes in the sample caused by beam damage.

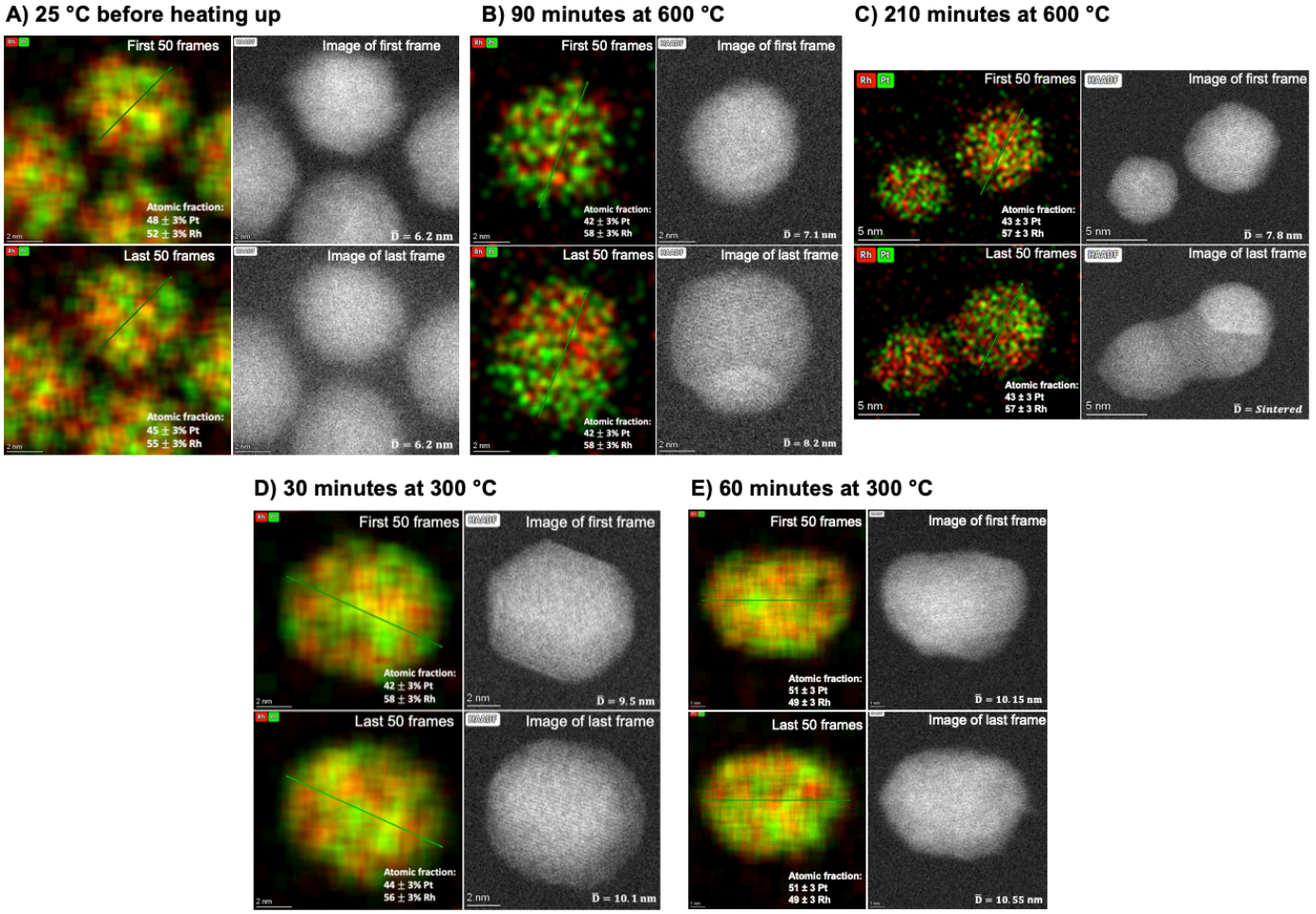

Figure 4.21: Effect of electron dosage as a function of temperature in representative nanoparticles from Synthesis 11. A) 25 °C; B) 90 minutes at 600°C; C) 210 minutes at 600°C; D) 30 minutes at 300 °C; E) 60 minutes at 300 °C. Top left: EDS map of the first 50 frames; Top right: HAADF image of the first EDS map frame; Bottom left: EDS map of the last 50 frames; HAADF image of the last EDS map frame. The signal for Rh is shown in red and for Pt in green. The reported size and atomic fraction are for nanoparticles with a green arrow. The size was measured in the direction of the arrow. The measurements were performed by in situ STEM at the target temperature.

4.3.2 Screening the thermodynamic stability of the solid solution $Pt_{0.50}Rh_{0.50}$ nanoparticles as a function of size and temperature

Next, we wanted to explore if the $Pt_{0.50}Rh_{0.50.}$ nanoparticles change from solid solution to segregated nanoparticles as a function of thermal energy and nanoparticle size in a vacuum. Three representative nanoparticles, ranging from 5 nm to 14 nm, were reported for each target temperature. The nanoparticles had never been exposed to the electron beam before the measurement. Figure 4.22 is a graphical representation of the *in situ* STEM experimental procedure. Each time the temperature was changed, an unexposed hole in the Fusion Thermal E-Chip window was used (Figure 4.22 – far right insert). The EDS maps, followed by the HAADF image of three representative nanoparticles of different sizes, were obtained at each target temperature. The nanoparticle diameter was measured in the direction it appeared to be largest. For the nanoparticles measured at 25 °C, at least 100 EDS frames were superimposed to create the nanoparticles' EDS maps. For the measurements *in situ* at 300 and 600 °C, only the first 50 EDS frames were used. The HAADF image of the first frame was used as a support for the EDS map.

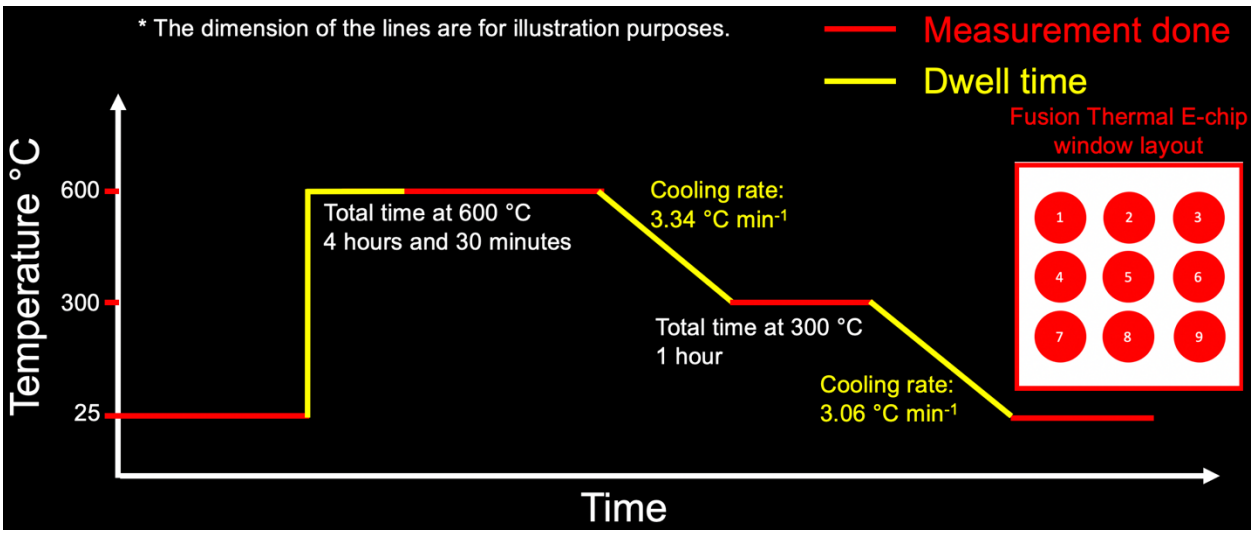

Figure 4.22: Graphical representation for the *in situ* STEM measurements of the solid solution $Pt_{0.50}Rh_{0.50}$ nanoparticles. The insert shows a graphical representation of the Fusion Thermal E-chip window layout.

The nanoparticle size and element distribution were analyzed at 25 °C before starting the *in situ* STEM measurements to check the status of the as-synthesized sample and create a baseline of the atomic distribution in the nanoparticles (Figure 4.22). Figure 4.23 (*left*) shows a HAADF image with an overview of the sample before heating. The sample contained well-defined nanoparticles.

The insert displays a histogram of 250 nanoparticles. The average size of the as-synthesized nanoparticles was 6.3 ± 1.2 nm. The size of the replicate of synthesis 11 was similar with overlapping margins of error with Synthesis 11 in Results 4.1.2.3 (7.1 ± 1.8 nm). Figure 4.23 (*right*) shows the EDS map followed by the HAADF image of Nanoparticles 1, 2, and 3. All three nanoparticles were in a solid solution configuration based on the evenly distributed EDS signal for Pt and Rh. The smooth change of contrast from the border to the center of the nanoparticles in the HAADF image support the finding.

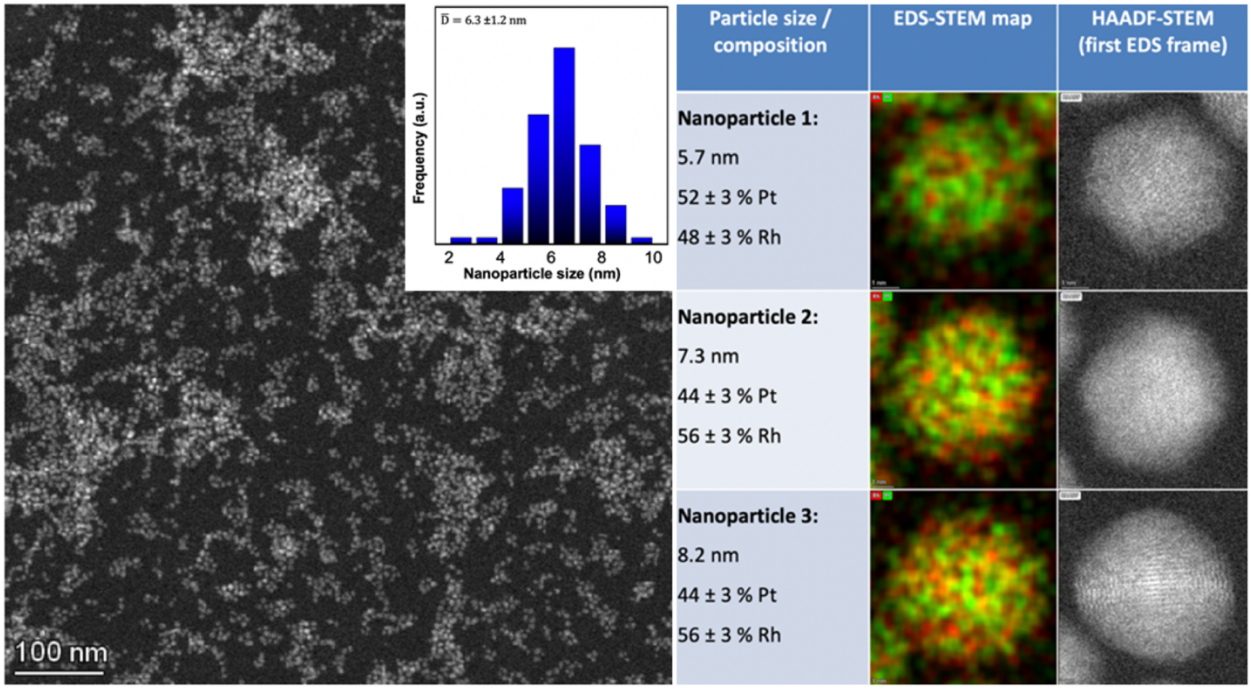

Figure 4.23: Screening of products from Synthesis 11 before heating. Left: HAADF image with an overview of products from Synthesis 11 before heating. The insert shows the nanoparticle size distribution. Right: Particle size/composition, EDS map and HAADF images of three representative nanoparticles of different sizes at 25 °C before heating. The signal for Rh is shown in red and for Pt in green.

The sample was instantly heated to 600 °C for a total of 4.5 hours (Figure 4.22), and after 1.5 hours of dwell time to allow the system to reach equilibrium, it was characterized *in situ* to explore how the sample changed due to temperature and time. Figure 4.24 *(left)* shows a HAADF image with an overview of the sample measured *in situ* at 600 °C after 1.5 hours of heat exposure, demonstrating that most nanoparticles sintered into structures of ~100 nm. Yet, the single *(non-sintered)* nanoparticles left in the sample were good candidates for *in situ* STEM measurements, and the experiment proceeded. The EDS map of Nanoparticles 4, 5, and 6 shows that they remained

in a solid configuration after heating (Figure 4.24 – *right*). The smooth change of contrast from the border to the center of the nanoparticles in the HAADF image support the finding. The EDS map of Nanoparticle 4 has a poor signal-to-noise ratio and gives a false impression of elemental segregation, but if the elements were segregated, the HAADF image would have shown an abrupt shift in contrast within the perimeter of the nanoparticles (see Figure 4.21B, C).

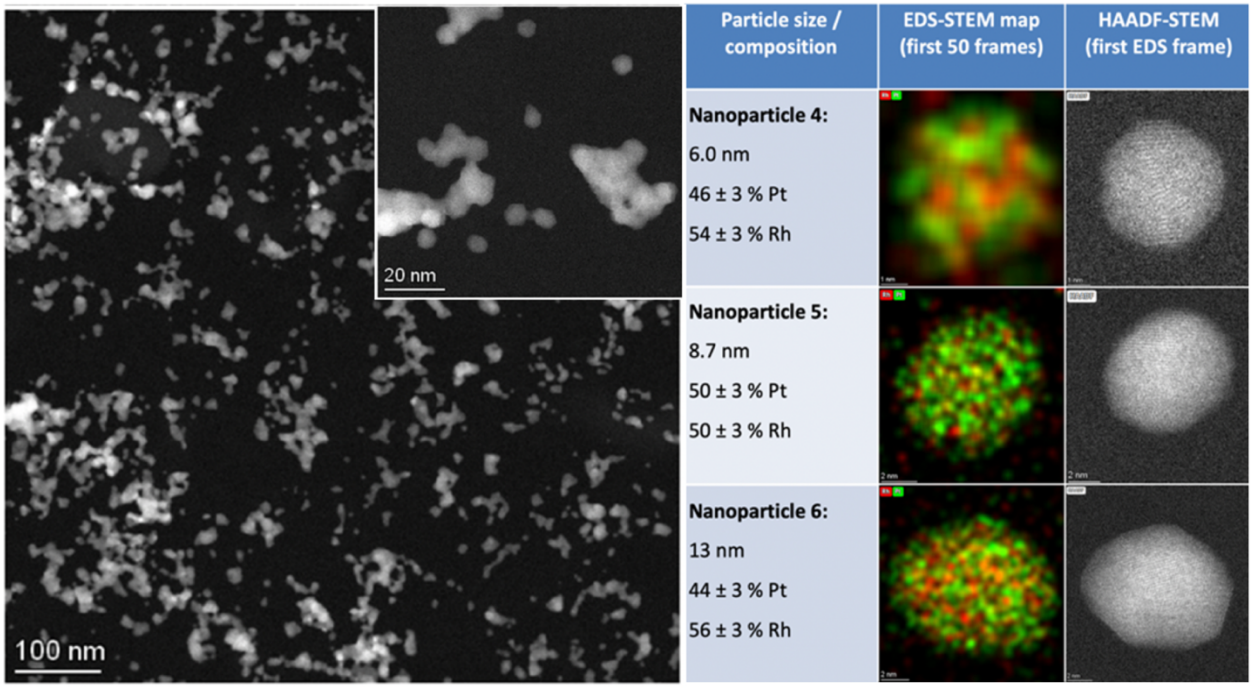

Figure 4.24: Screening of products from Synthesis 11 by in situ STEM at 600 °C. Left: HAADF image with an overview of products from Synthesis 11 measured in situ after 90 minutes at 600 °C; Right: Particle size/composition, EDS map and HAADF images of three representative nanoparticles of different sizes measured at 600 °C. The EDS signal for Rh is shown in red and for Pt in Green.

In all, the system was exposed to 600 °C for 4.5 hours. The sample was then cooled to 300 °C (3.34 °C min^{-1} – 1.5 hours) and characterized *in situ* (Figure 4.22). The cooling was done gradually to allow the system to reach equilibrium. The EDS maps show that Nanoparticles 7, 8 and 9 were in a solid solution configuration (Figure 4.25A). The smooth change of contrast from the border to the center of the nanoparticles in the HAADF image support the finding (Figure 4.25A). The system remained at 300 °C for one hour (Figure 4.22).

Finally, the sample was cooled to 25 °C (3.06 °C min^{-1} - 1.5 hours) and characterized (Figure 4.22). The EDS maps of Nanoparticles 10, 11, and 12 show that they were in a solid solution

configuration (Figure 4.25B). The smooth change of contrast from the border to the center of the nanoparticles in the HAADF image support the finding (Figure 4.25B).

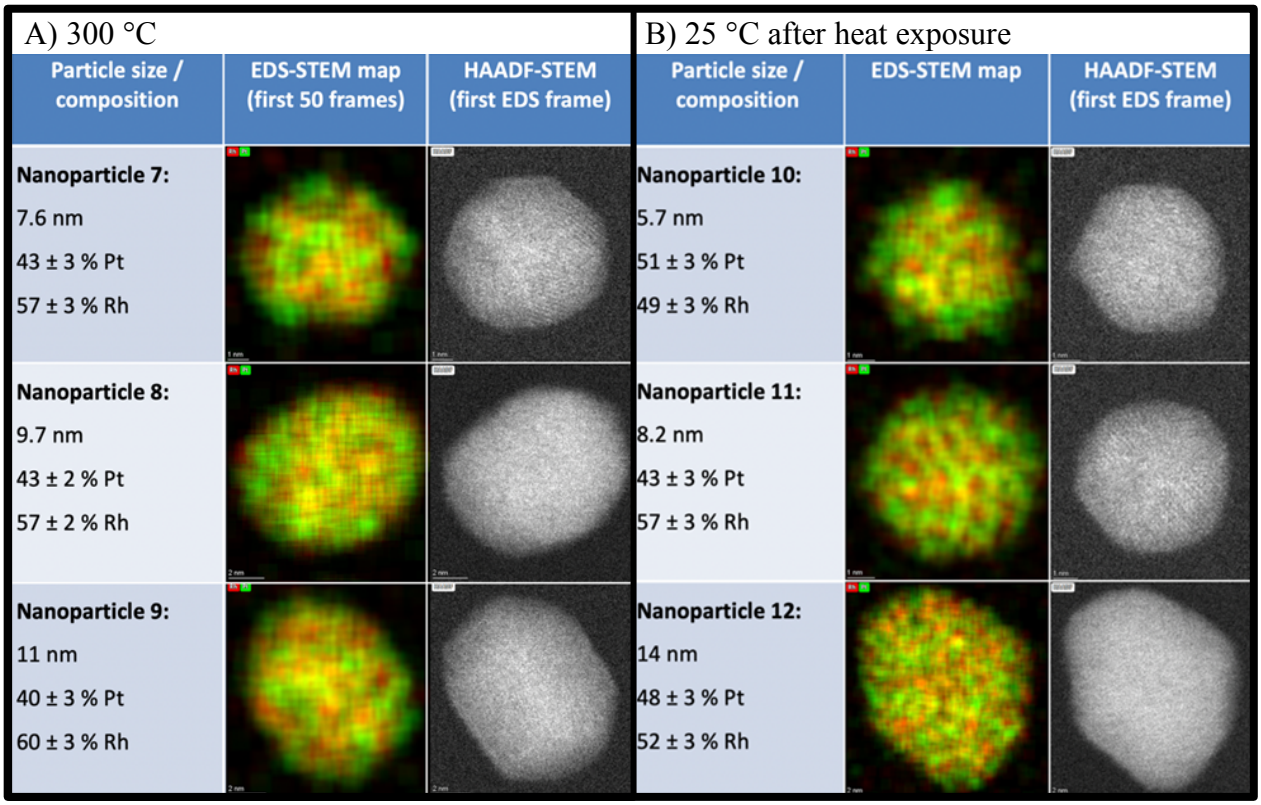

Figure 4.25: *Screening of products from Synthesis 11 during and after exposure to heat. Particle size/composition, EDS map and HAADF images of three representative nanoparticles of different sizes measured A) 300 °C and B) 25 °C, after exposure to heat. The EDS signal for Rh is shown in red and for Pt in Green.*

To conclude, that solid solution Pt_xRh_{1-x} nanoparticles, where x ranged from 0.40 ± 0.03 to 0.52 ± 0.03 within the size range of 5.7 to 14 nm were in a solid solution before they were heated (Figure 4.23 *right)* during the *in situ* STEM measurements (Figures 4.24 *right* and 4.25A), and after the *in situ* measurements (Figure 4.25B). As a result, it can be assumed that the solid solution configuration did not change by exposure to 600 °C for 4.5 hours, and 300 °C for one hour in a vacuum. To the best of our knowledge, there are no *in situ* STEM experiments reported in the literature to contextualize our findings. For a global discussion considering the bulk phase diagram and other similar systems, see Discussion 5.3.

5 Discussion

At least 60 % of chemicals produced today are synthesized through catalytic processes, and about 90 % of chemical processes are performed using a catalyst[1]. Accordingly, there is a need to study and develop catalysts that are energy efficient and have a high selectivity for the desired product. Catalyst development requires the production of well-defined model catalysts. The goal of this master's thesis was to develop well-defined model catalysts through synthesis of Pt_xRh_{1-x} solid solution nanoparticles and deposition of the nanoparticles on Al_2O_3 support. In addition, the thermal stability of the produced solid solution $Pt_{0.50}Rh_{0.50}$ nanoparticles was tested by *in situ* STEM.

5.1 Synthesis of solid solution Pt_xRh_{1-x} nanoparticles

Several research groups have employed the heat-up method to produce solid solution Pt_xRh_{1-x} nanoparticles using different precursors and solvents [19,24,26–29,42]. Nevertheless, because the Pt and Rh precursors tend to have different reduction rates due to their reaction kinetics[42], the produced nanoparticles contained either an Rh enriched[26]- or a Pt enriched[29] shell depending on the combination of precursors used. In this master's thesis, concurrent trials for preparing shell-free solid solution Pt_xRh_{1-x} were performed through the heat-up method using the autoclave- and the reflux approaches. The autoclave technique was used with the aim of tuning the reaction kinetics of Pt and Rh precursors by applying pressure. The reflux route was used in order to quench the reaction before the formation of a shell.

Synthesis of solid solution Pt_xRh_{1-x} nanoparticles through the autoclave method

The autoclave method successfully synthesized monodispersed Pd and Pt nanoparticles. We concluded the synthesis strategy to be reproducible, the nanoparticles were non-agglomerated and had a narrow size distribution (Results 4.1.1.1 – Figure 4.4 and Results 4.1.1.2 – Figure 4.5). However, the method still needs size optimization and the addition of Rh precursor to attempt alloying by simultaneous reduction. The autoclave trial was discontinued as the goal of producing shell-free solid solution Pt_xRh_{1-x} nanoparticles had been achieved through the reflux method.

Synthesis of solid solution PtxRh1–x nanoparticles through the reflux method

The starting point for synthesizing shell-free solid solution Pt_xRh_{1-x} were the procedures developed by Muri[28] and modified by Bundli[42] and Bundli *et al*.[29]. Bundli[42] studied the synthesis of Pt_xRh_{1-x} nanoparticles using both 1,4-butanediol and ethylene glycol. For this master's thesis, we chose ethylene glycol as solvent for synthesizing shell-free solid solution Pt_xRh_{1-x} nanoparticles because it does not have the same toxicity effects as 1,4-butanediol.

In order to achieve the solid solution nanoparticles, the first step was to perform a qualitative study of the relative kinetics of $Pt(acac)_2$, $Rh(acac)_3$, and an equimolar mixture of the two precursors. In the master's thesis, the formation of metallic nanoparticles is interpreted as the solution's color change from yellow to dark brown (Results 4.1.2.1 – Figure 4.6). Figure 4.18 in the Results 4.2.3 supports the postulation, as it shows that before the synthesis started, no nanoparticles were present in the solution and after the synthesis started, the nanoparticles nucleated and grew as a function of time. Nanoparticle growth can thus be interpreted as the transformation of Pt^{2+} into Pt^0. The reason for only using qualitative outcome measures was that a comprehensive analysis of the reaction kinetics of these precursors would be an extensive study in itself.

The kinetics experiment indicated that the synthesis could be broken down into two *reaction windows*: The Pt and Rh precursor react simultaneously in the first, forming a solid solution. The second window starts when the faster reacting Rh precursor is depleted, causing the formation of the Pt-rich shell. In this new strategy, the synthesis was stopped before the end of the first reaction window. As a result, the shell formation observed by Bundli *et al*.[29], replicated in Synthesis 9 (Results 4.1.2.2 – Figure 4.7), was avoided (Results 4.1.2.3 – Figures 4.8 and 4.10).

Because the relative reaction kinetics of Rh is faster than Pt, when equimolar amounts of precursors were used, the nanoparticles contained ~75 % Rh (Figure 5.1). We found, however, that the stoichiometry of the Pt_xRh_{1-x} could be controlled by exploiting collision theory. According to collision theory, the reaction rate depends on the frequency of collisions from the reacting specimen. One way of increasing the collision frequency is by increasing the concentration of reactants. For that reason, the ratio of Pt- relative to Rh precursor was increased to tune the final concentration of the nanoparticles. The stoichiometry of the nanoparticle can thus be controlled by

applying the equation of the curve from Figure 4.14, and we document that the entire solid solution range can be obtained (Pt_xRh_{1-x}, $0 \leq x \leq 1$). For details, see Results 4.1.2.6.

The compositions of the nanoparticles from Syntheses 10 to 12 (Results 4.1.2.4 – Table 4.7) were determined by EDS, ICP-OES and calculated using variations in unit cell dimensions extracted by PXRD and application of Vegard's law. The percentage of Rh detected by each analytical method was within the margin of error (Figure 5.1). Notably, both EDS and ICP-OES give the gross composition of the nanoparticles, whereas Vegard's law adds the information that the elements are distributed throughout the particle as a solid solution. In addition, the EDS atomic-scale resolution elemental mapping (Results 4.1.2.3 – Figures 4.8 and 4.10) support the results from PXRD.

Both Syntheses 11 and 18 contained the nominal composition of 75 % Pt and 25 % Rh, but the metal precursor concentration of Synthesis 18 was six-fold lower (Results 4.2.4 – Table 4.9), and the concentration of PVP was three-fold higher than in Synthesis 11 (Results 4.1.2.3 – Table 4.4). In Syntheses 11 and 18, the detected percentage of Rh in the nanoparticles was ~50 %. As a consequence, it can be deduced that the critical parameter for tuning the stoichiometry of the nanoparticle is the Pt- to Rh precursor ratio.

The nanoparticles from Syntheses 10, 11, and 12 had a size distribution slightly wider than the one reported by Bundli *et al.*[29]. For instance, while Synthesis 11 produced solid solution $Pt_{0.50}Rh_{0.50}$ nanoparticles averaging 7.1 ± 1.8 nm (insert in Figure 5.1) the synthesis for solid solution $Pt_{0.50}Rh_{0.50}$ nanoparticles reported by Bundli *et al.*[29] produced nanoparticles averaging 6.9 ± 0.7 nm. A possible reason for the discrepancy is a high precursor concentration in Syntheses 10, 11, and 12. If the precursor concentration is too high, the system might supersaturate with new nucleation events for too long (Methods and Theory 2.1.2). In addition, because the synthesis time is relatively short, there was not enough time for *size focusing* to occur (Methods and Theory 2.1.3). In contrast, the synthesis reported by Bundli *et al.*[29] was performed over two hours. A possible remedy for the wide size distribution is to lower the concentration of metal precursors in the solution. By doing so, the period where the system is supersaturated could be shortened.

Another interesting observation is that the nanoparticles' average size and size distribution from Syntheses 11 and 18 are virtually the same, even though Synthesis 18 had a lower concentration of precursor than Synthesis 11 (Figure 5.1). The kinetics of particle formation is also a function of

PVP concentration, which can act as a reduction agent[115]. Thus, even though the concentration of precursors was lower, the higher PVP concentration could have led the system's overall reactivity to remain similar. Moreover, Hei *et al*.[16] (Introduction 1.4 – Table 1.1) reported that increasing the PVP-to-metal ratio in solution leads to an increase in the average size of the nanoparticles. Synthesis 11 had a 10 to 1 PVP-to-metal ratio, and Synthesis 18 had a 101 to 1 PVP-to-metal ratio. Therefore, the nanoparticle size stayed the same even though the precursor concentration was reduced. The observed result is in-line with the results reported by Hei *et al*.[16].

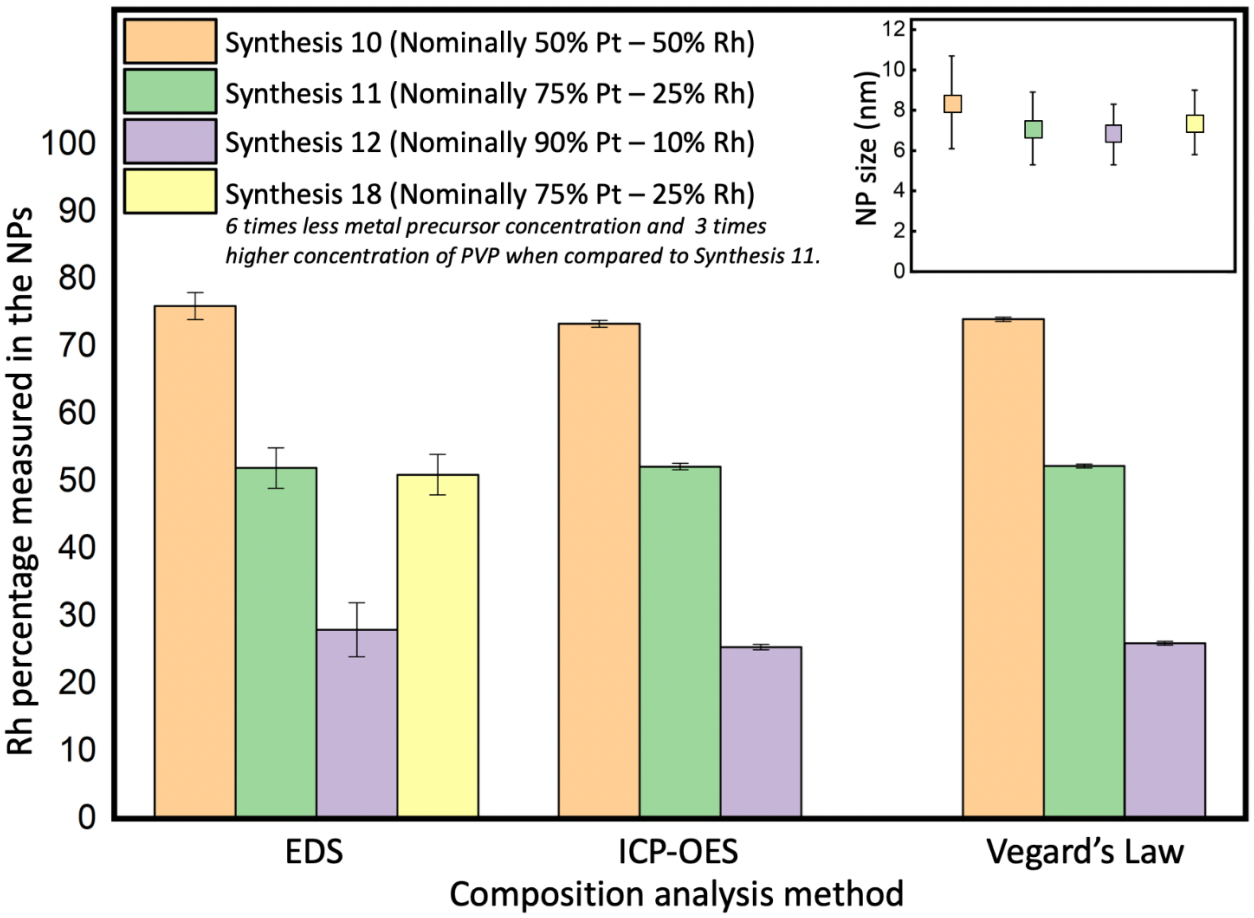

Figure 5.1: Nanoparticle composition using different analytical methods. Measured percentage of Rh for Syntheses 10 (orange), 11 (green), 12 (purple), and 18(yellow). The insert shows the average nanoparticle size for each synthesis. For details about Syntheses 10 to 13, see Table 4.4 in Results 4.1.2.3; for Synthesis 18, see Table 4.9 in Results 4.2.4.

Quenching the reaction before all precursor is consumed makes the synthesis strategy expensive as the slower reacting noble metal precursor is not consumed. Nevertheless, the strategy is suitable/acceptable for preparing model catalysts, as they are only produced in small quantities. Yet, if the non-used precursors could be recycled, the strategy could be employed for large-scale production of solid solution nanoparticles.

To our knowledge, quenching the synthesis before the slow reactant is consumed is a novel synthesis strategy. By applying this method, shell-free solid solution Pt_xRh_{1-x} nanoparticles could be produced by the heat-up method. The strategy appears promising for preparing bimetallic solid solution nanoparticles of various metals. The only requirement is a *reaction window* overlap of the metal precursors. The experimental method sets the stage for future in-situ and operando measurements using the temperatures and atmospheric conditions in which ammonia oxidation and for measurements of other chemical reactions that such nanoparticles could serve as catalysts.

5.2 Development of well-defined Pt/Al_2O_3 and $Pt_{0.50}Rh_{0.50}/Al_2O_3$ catalysts

Two commonly used methods to prepare model catalysts are wet impregnation and direct colloidal deposition (Methods and Theory 2.7.1). The wet impregnation method is easy to implement, but control over nanoparticle size and size distribution is elusive. For this master's thesis, the colloidal deposition method was chosen for producing the Pt and solid solution $Pt_{0.50}Rh_{0.50}$ nanoparticles supported on Al_2O_3. The goal was to produce well-defined nanoparticles in terms of their size, size distribution, and alloying. The nanoparticles would then be deposited to Al_2O_3 support and calcinated for activation of the catalyst. For the latter step, the dispersion of the nanoparticles on the support was a point of focus.

The Pt nanoparticles were synthesized and deposited on Al_2O_3 support using the method reported by Muri[28] (Results 4.2.3 – Synthesis 13). Yet, after synthesis and deposition of the Pt nanoparticles, we noticed that the nanoparticles were agglomerated onto the support (Results 4.2.2 – Figure 4.16). As a consequence, the agglomerated nanoparticles would sinter during the calcination, and the system would no longer remain well-defined. We, therefore, needed to design a protocol to produce non-agglomerated Pt nanoparticles on Al_2O_3.

Our first hypothesis was that the agglomeration occurred during the washing-, redispersion-, and deposition procedures, as the nanoparticles are introduced to chemical environments that promote

flocculation and redispersion during these procedures. We believed that the nanoparticles may have been flocculating but not dispersing again. A range of strategies, such as changes in the sonication method, the addition of PVP during redispersion, and the use different solvents for redispersion failed to produce non-agglomerated Pt nanoparticles deposited on Al_2O_3 (Results 4.2.3 – Table 4.8 and Figure 4.17).

Our second hypothesis was that the nanoparticles were synthesized as agglomerates. Figure 4.18 in Results 4.2.3 contains SEM images depicting the morphology of the nanoparticles as a function of time during the synthesis. We observed that the nanoparticles were not agglomerated during the first 15 minutes. However, 20 minutes into the experiment, loose and agglomerated nanoparticles began to appear, and after 30 minutes, the system was composed primarily of agglomerates. The conclusion was that the Pt nanoparticles were agglomerating during synthesis.

The synthesis of non-agglomerated Pt nanoparticles require coating by capping agents. When non-coated Pt nanoparticles approach each other, van der Waals forces may lead to irreversible aggregation (Methods and Theory 2.2). Another critical parameter for producing dispersed nanoparticles is the concentration of surfactant used in the synthesis. When too little- or too much surfactant is used, the nanoparticles agglomerate by bridging or depleting flocculation[62], respectively. Figure 4.18 in Results 4.2.3 shows that the Pt nanoparticles were not agglomerated during the first 15 minutes of Synthesis 13. As the nanoparticles continued to grow, the amount of PVP in the system appeared insufficient to cover the nanoparticles' surface adequately, and therefore agglomeration started to occur. For that reason, we believed that the nanoparticles were agglomerating due lack of surfactant in the solution.

Results 4.2.4 shows that the critical parameter for producing dispersed nanoparticles was the molar concentration of PVP in 1,4-butanediol solution. Agglomerated nanoparticles were produced when the PVP concentration was lower than 338 mM. The new concentration of PVP could also be applied to the synthesis of the solid solution $Pt_{0.50}Rh_{0.50}$ nanoparticles in ethylene glycol (Results 4.2.4 – Synthesis 18). To our knowledge, it is the first systematic study of the role of PVP in the dispersion of Pt and $Pt_{0.50}Rh_{0.50}$. The obtained results are in line with Li *et al*. who reported an optimal concentration of PVP in solution to produce dispersed nanoparticles of $BaTiO_3$[63].

The amount of PVP used for synthesizing Pt and Pt-Rh alloys is commonly reported in the literature as the PVP-to-metal ratio in the synthesis[16,20,22,24,27–29]. Hei *et al*. systematically studied how the concentration of PVP-to-metal ratio influences the nanoparticle size [16]. However, only Papa *et al*. used a molar concentration of PVP (380 mM; Table 5.1) equivalent to what we used for preparing non-agglomerated nanoparticles (338 mM; Table 5.1) and were successfully able to produce non-agglomerated nanoparticles[18] (Introduction 1.3 – Figure 1.5C). The other syntheses referred to in Introduction 1.3 display agglomerated nanoparticles (Figures 1.5A, B, D-N). Moreover, all of the reported syntheses used a PVP-to-metal ratio between 2.5 to 1 and 12 to 1 (Table 5.1). In contrast, we successfully produced nanoparticles using the PVP-to-metal ratio up to 270 to 1.

The concentration of 338 mM PVP successfully produced dispersed Pt and solid solution $Pt_{0.50}Rh_{0.50}$ nanoparticles on support using the procedure reported by Muri[28]. The surfactant was removed to activate the catalyst by calcinating the nanoparticles at 400 °C under synthetic airflow. Even if the monometallic Pt nanoparticles were to oxidize, they could easily be reduced again by calcination in a hydrogen gas atmosphere[116]. Zacharki *et al*. demonstrated that Ni nanoparticles supported on Al_2O_3 oxidize and suffer severe reconstruction during calcination in synthetic gas, but get readily reduced if calcinated in a hydrogen gas atmosphere[116]. However, if the nanoparticles were composed of alloys, for instance Pt_xRh_{1-x}, the two elements would respond differently to the oxidation/reduction cycle used[116]. In another study of nanoparticles of Pt and Rh, Tomoya *et al*. demonstrated that heating solid solutions $Pt_{2/3}Rh_{1/3}$ nanoparticles in an atmosphere containing oxygen gas created a Rh_2O_3 shell on the nanoparticle[117]. After the oxidation step, they heated the same particles in hydrogen gas, resulting in a nanoparticle with an Rh-rich shell[117].

In conclusion, we have successfully produced well-defined Pt/Al_2O_3 and $Pt_{0.50}Rh_{0.50}/Al_2O_3$ nanoparticle catalysts. Now, the catalytic activity of Pt can be measured and directly compared to the catalytic activity of the solid solution $Pt_{0.50}Rh_{0.50}$ nanoparticles. Lastly, the method for synthesizing well-dispersed nanoparticles developed in Results 4.2.3 should apply to all polyol synthesis for Pt, Rh, $Pt_xRh_{1-x,}$ as well as the core-shell Pt@Rh and Rh@Pt configurations used at the NAFUMA research group.

Table 5.1: PVP-to-metal ratio and molar concentration of PVP in solution for previously reported syntheses of Pt or Pt_xRh_{1-x} solid solution nanoparticles and some selected syntheses from this master's thesis. The syntheses with agglomerated nanoparticles are shown in red, and dispersed nanoparticles in green. PVP, polyvinylpyrrolidone.

Authors	**Hei *et al.*[16]**	**Long *et al.*[17]**	**Papa *et al.*[18]**	**Han *et al.*[19]**	**Song *et al.*[20]**	**Herricks *et al.*[21]**	**Koebel *et al.*[22]**
$\frac{[PVP]}{[Metal]}$	5/1 to 40/1	6/1	10/1	9/1	12/1	2.6/1	9/1
[PVP] (mM)	1 to 48	250	380	9	156	26	12.7 to 71.1
Authors	**Safo *et al.*[23]**	**Park *et al.*[24]**	**Alayoglu *et al.*[25]**	**Musselwhite *et al.*[26]**	**Park *et al.*[27]**	**Muri[28]**	**Bundli *et al.*[29]**
$\frac{[PVP]}{[Metal]}$	3/1 to 12/1	10/1	2.5/1	2.5/1	10/1	10/1	10/1
[PVP] (mM)	7.8 to 31.2	12.5 to 50	25	25	6.25 to 100	100	100
This thesis	**Synthesis 12**	**Synthesis 13**	**Synthesis 14**	**Synthesis 15**	**Synthesis 16**	**Synthesis 17**	**Synthesis 18**
$\frac{[PVP]}{[Metal]}$	2	10	30	90	90	270	101
[PVP] (mM)	100	38	113	338	113	338	338

5.3 Screening of the thermal stability of solid solution $Pt_{0.50}Rh_{0.50}$ nanoparticles' by *in situ* scanning transmission electron microscopy

Evaluation of the stable configuration of the Pt_xRh_{1-x} nanoparticles

In Results 4.3 we measured the thermal stability at 300 and 600 °C of solid solution Pt_xRh_{1-x} nanoparticles, where x ranged from 0.40 ± 0.03 to 0.52 ± 0.03, by *in situ* STEM in UHV. In the experiment, EDS near atomic scale resolution elemental mapping and HAADF images were extracted from nanoparticles within the size of 5.7 to 14 nm before they were heated, *in situ* at 300 and 600 °C, and after heat exposure. From the results, we concluded that all of the measured nanoparticles were in a solid solution before they were heated (Results 4.3.2 – Figure 4.23), during the *in situ* STEM measurements (Results 4.3.2 – Figures 4.24 and 4.25A), and after the *in situ* measurements (Results 4.3.2 – Figure 4.25B). This contradicts the predicted miscibility dome in the bulk binary phase diagram for Pt and Rh, which predicts that Pt_xRh_{1-x} with x ranging from 0.40 ± 0.03 and 0.52 ± 0.03 only exist as solid solution at temperatures above ~760 °C (Introduction 1.3 – Figure 1.6). To our knowledge, it is the first time the thermodynamic stability of solid solution Pt_xRh_{1-x} nanoparticles has been explored by *in situ* STEM in UHV. As will be discussed, our observations are insufficient to fully draw conclusions regarding their thermodynamic stability, but we believe it is a good starting point for more thorough investigations.

In order to evaluate the thermal stability of nanoparticles using *in situ* STEM, beam damages need to be considered. In Results 4.3.1, we evaluated how the *in situ* STEM experiments had to be carried out not to create artifacts related to beam damage. By solely using the 50 first frames in each EDS map, the effect of the electron dose was suppressed and did not affect the results with respect to element distribution. Notably, it is also documented that the thermal heating associated with such experiments are in the range of 1 °C[95]. Therefore, an important conclusion is that our thermal stability evaluations were not influenced by beam damage.

The bulk Pt-Rh binary phase diagram published by ASM international[30] is based on theoretical calculations proposed by Raub[38] (Introduction 1.3 – Figure 1.6). Several other studies have also produced results that conflict with their Pt-Rh binary phase diagram predictions. Interestingly, Steiner *et al*. used neutron scattering to study the ordering in the bulk $Pt_{0.47}Rh_{0.53}$ alloy and found

that it formed a solid solution[118]. The study was a result of a long discussion on the topic of whether the Pt-Rh alloys formed ordered alloys or solid solutions (disordered alloys)[118–121]. In addition, Maisel *et al*. used simulations to conclude that there is no miscibility gap in the bulk Pt–Rh binary phase diagram[122]. Although the existence of the miscibility gap is debated, the bulk phase diagram in Figure 1.6 is still largely acknowledged[122], and it is used as basis for this master's thesis. Additionally, we are aware that the phase diagram only describes the situation in bulk, and not necessarily represents the situation at the nanoscale.

It has previously been reported that the phase diagrams of nanoalloys can diverge from their bulk counterpart[31]. In bulk, the surface and interfacial contribution to the total Gibbs energy is so small that they are usually neglected[31]. On the other hand, as nanoalloys get smaller, the contributions from surface- and interfacial energies becomes significant to the total Gibbs energy of the system[31]. That may result in a shift in the equilibrium solubility lines from the original bulk phase diagram. This shift leads to changes in the phase stability of the material when it enters the nano-regime[31]. For instance, the miscibility dome shown in the bulk binary Pt-Rh phase diagram could be suppressed to much lower temperatures. This implies that, if the *in situ* STEM findings of the Pt_xRh_{1-x} nanoparticles reflect their thermodynamic equilibrium, an alloy with x ranging from 0.40 ± 0.03 to 0.52 ± 0.03 Pt-Rh will form a solid solution in the temperature interval from room temperature to 600 °C, and particle sizes in the range from 5.7 to 14 nm in UHV.

An unanswered question is whether the experiment was performed using conditions that allowed the system to reach equilibrium. If not, one could foresee a scenario where the stable configuration was a segregated particle with respect to composition. For that to happen, a phase transformation would need to occur, and kinetics would need to be overcome to obtain segregation[123]. The solid solution nanoparticles of Pt_xRh_{1-x}, where x ranged from 0.40 ± 0.03 to 0.52 ± 0.03, and size ranged from 5.7 to 14 nm, were exposed to 600 °C for 4.5 hours, cooled down to 300 °C at the rate of 3.34 °C min^{-1} (1.5 hours), exposed to 300 °C for one hour, and cooled down to 25 °C at the rate of 3.06 °C min^{-1} (1.5 hour). If the bulk phase diagram for Pt_xRh_{1-x} is valid at the nanoscale, one possible explanation for the lack of nanoparticle segregation could be that the system was not exposed to the target temperature for long enough to overcome the kinetics and reach the stable configuration.

In 2019, Kumar *et al.* published a Pt-Rh diffusion coefficient in bulk at 1000 °C; $D^{Rh\rightarrow Pt\,(100)} = 18\ \frac{nm^2}{s}$, $D^{Rh\rightarrow Pt\,(110)} = 8\ \frac{nm^2}{s}$, $D^{Rh\rightarrow Pt\,(111)} = 18\ \frac{nm^2}{s}$, and $D^{Pt\rightarrow Rh\,(100,110,111)} = 0.16\ \frac{nm^2}{s}$, showing that there is diffusion at high temperatures[124]. In addition, it has been previously reported that materials at the nanoscale have enhanced diffusion effects relative to their bulk counterparts[125]. The diffusion of Cu in Au nanocrystals ensemble with an average size of 10 nm at room temperature is higher by at least nine orders of magnitude when compared to their bulk counterpart[126]. Au in semiconductor Ag_2S nanocrystal ensemble[127] and Ag in Au nanocrystal ensemble[128] have diffusion coefficients up to 16 orders of magnitude higher than their bulk counterpart. All these factors indicate that the solid solution Pt_xRh_{1-x} nanoparticles, where x ranged from 0.40 ± 0.03 to 0.52 ± 0.03, and size ranged from 5.7 to 14 nm, should have had sufficient time to reach equilibrium within the timeframe of the experiment. In addition, it can be noted that in the areas where there was nanoparticle agglomeration, the sample had sintered after being exposed to 600 °C for 4.5 hours (Results 4.3.2 – Figure 4.24 *left*). Sintering is an indication that there was mobility in the system, and that the solid solution could be the thermodynamic stable configuration of the nanoparticle size regime measured at the actual conditions (UHV, temperatures up to 600 ºC).

For the measurements at 300 °C we expected mobility to be lower than at 600 °C. Consequently, one hour at 300 °C might not have been sufficient for the system to reach equilibrium, i.e., it is still an open question if the kinetics has been to slow or if we have identified the stable configuration of the alloy.

Notably, we may have insufficiently considered the fact that the nanoparticles were coated with PVP. Before the *in situ* STEM measurements in UHV, no attempts were made to remove the PVP capping from the nanoparticles. Wang *et al*. reported that the surfactant polyacrylate could sublime during *in situ* TEM experiments in UHV at the temperature range of 180-250 °C[46]. The conditions of *in situ* STEM and *in situ* TEM are nearly identical, the main difference being how the beam illuminates the sample[95] (Methods and Theory 2.8.2). To our knowledge, no such observations have been reported for PVP at the same conditions. In addition, PVP gets converted into a thin layer of amorphous carbon when calcinated in H_2 and O_2 atmospheres at temperatures between 300-350 °C[129]. Carbon impurities on the surface of the nanoparticles can complicate data analysis.

For instance, it has been previously reported that carbon depresses the melting point of rhodium by 11.9% and platinum by 1.6 %[130]. For that reason, a procedure to remove PVP prior to such measurements needs to be considered and developed, and new *in situ* STEM experiments where PVP is removed from the nanoparticles should be used to draw conclusions on what may be the stable configuration of the Pt_xRh_{1-x} nanoparticles. This is a fruitful topic for further work.

The importance of in situ STEM experiments

Although *ex situ* STEM experiments provide an idea of the bimetallic nanoparticles overall stability[50], it comes short of showing their morphology and elemental distribution within the nanoparticles' at the temperature range of interest. A first step to observe the nanoparticles at realistic conditions is to heat them in UHV to the target temperature, and follow their morphological changes and possible elemental re-arrangement during the heat treatment. The experiment undertaken in this work is of such a character, and we have preliminarily concluded that Pt_xRh_{1-x} nanoparticles are stable as solid solution up to 600 °C.

The consequence of these results is that if the nanoparticles were synthesized in a core-shell configuration rather than a solid-solution, an elemental re-arrangement would take place upon heating if we assume that a solid solution is the stable configuration. However, in order to know the stable configuration of the nanoparticle in the conditions in which they are used, for instance within catalysts, the effect the gas atmosphere has on the nanoparticles also needs to be accounted for.

To the best of our knowledge, *in situ* ambient pressure STEM studies are still to be conducted for Pt_xRh_{1-x} nanoparticles. However, we are aware of one *in situ* Bragg coherent diffraction imaging experiment on a solid solution $Pt_{2/3}Rh_{1/3}$ nanoparticle larger than 200 nm. Tomoya *et al.*[117] performed their study by exposing one nanoparticle to 2.7-5 % O_2 in He and 3.8 % H_2 in He at 550 and 700 °C. They observed the growth of a layer of Rh_2O_3 on the nanoparticles during the O_2 atmosphere measurements. When exposed to temperature and H_2 atmospheres, Rh got reduced to metal, leaving a Rh shell on the alloy[117]. This experiment demonstrates that temperature alone is not the only factor influencing the elemental distribution of the nanoparticle, but the choice of gas atmosphere can lead to segregation of solid solution systems into core-shell structures. Such in

situ experiments are indispensable in order to correlate the performance of the catalyst to the chemical composition of the nanoparticle surface, where the catalysis reaction takes place.

In conclusion, *in situ* STEM experiments are crucial because they stretch the measurements toward realistic operational process conditions. By doing so, they provide direct input on the materials' characteristics in the conditions in which they are used. The use of *in situ* techniques and well-defined model catalysts, prepared by careful deposition routes as described in this work, is crucial for development of optimal catalysts with high activity and selectivity to the targeted product.

6 Conclusions

The main focus of this master's thesis was the synthesis and characterization of solid solution Pt_xRh_{1-x} nanoparticles, their deposition onto Al_2O_3 support to prepare well-defined model catalysts for the selective oxidation of NH_3 into N_2, and testing of the thermal stability of the solid solution nanoparticles $Pt_{0.5}Rh_{0.5}$ as a function of temperature at UHV by means of *in situ* STEM.

Taken together, in this master's thesis, we have:

- Developed an autoclave synthesis route for Pt, that appears promising for preparing nanoparticle alloys.
- Synthesized solid solution Pt_xRh_{1-x}, where x = 0.25, 0.50. and 0.75, introducing the novel step of having information on the metal precursors' relative reaction kinetics, and halting the synthesis at a point where the faster reacting metal precursor is not fully consumed. Formation of true solid solution nanoparticles, using this approach, is documented by combining STEM-EDS, XRD and unit cell determinations with ICP-OES elemental analysis.
- Prepared well-defined Pt/Al_2O_3 and solid solution $Pt_{0.50}Rh_{0.50}/Al_2O_3$ model catalysts with highly dispersed nanoparticles, documented by SEM using the low angle backscattered electron mode. Successful preparation only became possible after correcting the existing preparation protocols to use significantly higher surfactant concentrations during the nanoparticle synthesis step. ICP-OES confirmed metal loading of the catalysts to be close to the targeted value of 0.5 weight % (Pt: 0.56 weight %; $Pt_{0.50}Rh_{0.50}$: 0.61 weight %).
- Carried out the first *in situ* STEM study at UHV and shown that the solid solution elemental distribution of the as-synthesized Pt_xRh_{1-x}, where x ranged from 0.40 ± 0.03 to 0.52 ± 0.03, and nanoparticle size ranged from 5.7 to 14 nm, did not change after a 4.5 hour exposure to 600 °C and one hour exposure to 300 °C in UHV. The results indicate that the nanoparticles are stable in the solid solution configuration, without displaying element segregation. The experiments were not hampered by beam damage effects. The influence of the surfactant on the stability of the nanoparticles is currently not accounted for and requires further investigations.

7 Perspectives

In this master's thesis we developed model catalysts of monometallic Pt nanoparticles and solid solution Pt_xRh_{1-x} nanoparticles deposited on Al_2O_3. The nanoparticles were monodispersed with similar average sizes, were not agglomerated, and did not sinter during calcination for removal of PVP. Therefore, they are apt for being tested for the selectivity toward N_2 in the ammonia oxidation reaction as model catalysts. The catalytic activity of Pt can be measured and directly compared to the catalytic activity of the solid solution $Pt_{0.50}Rh_{0.50}$ nanoparticles.

We have also developed an autoclave synthesis for Pt nanoparticles, with the aim of developing Pt_xRh_{1-x} solid solution nanoparticles. The synthesis was halted because the goal of synthesizing solid solution Pt_xRh_{1-x} nanoparticles with homogeneous elemental distribution had been achieved using the reflux approach. Thus, synthesis of nanoparticles using an autoclave remains largely unexplored in the NAFUMA research group. We aim to pursue this method further by developing a procedure to attain control of nanoparticle size and morphology, then adding a step to introduce Rh to promote alloying. Such work would be valuable to the group by making a new synthesis method available.

The *in situ* experiments showed that solid solution Pt_xRh_{1-x} nanoparticles, where x ranged from 0.40 ± 0.03 to 0.52 ± 0.03, and nanoparticle sizes in the ranged from 5.7 to 14 nm, maintained their solid solution configuration when heated to 300 and 600 °C. The results are in conflict with the bulk Pt-Rh binary phase diagram published by ASM international, which predicts that the system should exist as a Pt- and a Rh-rich phase. However, the fact that PVP had not been removed from the surface prior to the measurement prevents us from fully concluding whether the nanoparticles tested were in a thermodynamically stable configuration. Further experiments are, therefore, needed to evaluate the influence of PVP on the stability of the nanoparticles. By performing *in situ* XPS heating studies in UHV, we could learn whether PVP is fully removed, or alternatively, whether it decomposes into carbon biproducts on the surface of the nanoparticles at 300 and 600 °C. In addition, we need to develop a procedure to fully remove PVP in UHV. This could also be performed by *in situ* XPS analysis. The *in situ* XPS analysis would additionally provide data on the chemical state of the Pt_xRh_{1-x} nanoparticles, thus allowing us to investigate whether the alloy would remain in solid solution configuration when PVP is fully removed from the nanoparticles'

surface. Preferably, the same nanoparticles should be used for both the PVP removal experiment by *in-situ* XPS and for the *in situ* STEM studies. That way, the data measured by *in situ* STEM could be directly correlated to nanoparticles without PVP on their surface.

Key information regarding the thermodynamic stable configuration of Pt-Rh nanoparticles could also be obtained by *in situ* STEM studies of phase segregated Pt@Rh, and Rh@Pt core-shell nanoparticles. The study could be performed by obtaining an EDS map of a segregated Pt@Rh core shell nanoparticle before it was heated, and then obtain an EDS map of the same nanoparticle after 1.5 hours at 600 °C. That way, the element distribution change within the nanoparticle would be directly correlated to the effect of the exposure to 600 °C. In addition, if there is elemental diffusion in the system, and solid solution is the thermodynamically stable configuration of Pt-Rh nanoparticles, the segregated Pt@Rh core-shell configuration will undergo a phase transformation to solid solution when exposed to 600 °C as a function of time. This phase transformation could also be determined by EDS maps concurrently with HAADF images of the nanoparticles. However, procedures to produce segregated Pt@Rh, and Rh@Pt core-shell nanoparticles that are between 5.7 to 14 nm in size and contain between 40 ± 3 % and 52 ± 3 % Pt relative to Rh need to be established for the experiments to be performed.

8 References

(1) *Catalytic Process Technology*; National Academies Press: Washington, D.C., 2000. https://doi.org/10.17226/10038.

(2) Xia, Y. Are We Entering the Nano Era? *Angew. Chemie - Int. Ed.* **2014**, *53* (46), 12268–12271. https://doi.org/10.1002/anie.20140674.

(3) Cotton, F. A.; Wilkinson, G. *Advanced Inorganic Chemistry*, 5th ed.; 1988.

(4) Frenken, J. W. M.; Veen, J. F. van der. Observation of Surface Melting. *Phys. Rev. Lett.* **1985**, *54* (2), 134–137. https://doi.org/10.1103/PhysRevLett.54.134.

(5) Buffat, P.; Borel, J. P. Size Effect on the Melting Temperature of Gold Particles. *Phys. Rev. A* **1976**, *13* (6), 2287–2298. https://doi.org/10.1103/PhysRevA.13.2287.

(6) Rogers, B.; Pennathur, S.; Adams, J. *Nanotechnology: Understanding Small Systems, Second Edition (Mechanical and Aerospace Engineering Series)*, 2nd ed.; CRC Press, 2011.

(7) Samrot, A. V.; Sahithya, C. S.; Selvarani A, J.; Purayil, S. K.; Ponnaiah, P. A Review on Synthesis, Characterization and Potential Biological Applications of Superparamagnetic Iron Oxide Nanoparticles. *Curr. Res. Green Sustain. Chem.* **2021**, *4*, 100042. https://doi.org/10.1016/j.crgsc.2020.100042.

(8) Thompson, D. A.; Best, J. S. The Future of Magnetic Data Storage Techology. *IBM J. Res. Dev.* **2000**, *44* (3), 311–322. https://doi.org/10.1147/rd.443.0311.

(9) Kim, Y. K. Magnetic iron oxide nanoparticles for MR contrast agents https://bme240.eng.uci.edu/students/08s/ykim30/02.htm (accessed May 23, 2022).

(10) Quantum dots https://www.sigmaaldrich.com/NO/en/technical-documents/technical-article/materials-science-and-engineering/biosensors-and-imaging/quantum-dots (accessed May 19, 2022).

(11) Schlögl, R. Heterogeneous Catalysis. *Angew. Chemie Int. Ed.* **2015**, *54* (11), 3465–3520. https://doi.org/10.1002/anie.201410738.

(12) Xiong, Y.; Lu, X. *Metallic Nanostructures*; 2015. https://doi.org/10.1007/978-3-319-11304-3.

(13) Fjellvåg, A. S.; Waller, D.; Skjelstad, J.; Sjåstad, A. O. Grain Reconstruction of Palladium and Palladium-Nickel Alloys for Platinum Catchment. *Johnson Matthey Technol. Rev.* **2019**, *63* (4), 236–246. https://doi.org/10.1595/205651319X15597236291099.

(14) Sjåstad, A. O. Inorganic Chemistry (KJM 1121) Lecture. Oslo, Norway 2022.

(15) Ivashenko, O.; Johansson, N.; Pettersen, C.; Jensen, M.; Zheng, J.; Schnadt, J.; Sjåstad, A. O. How Surface Species Drive Product Distribution during Ammonia Oxidation: An STM and Operando APXPS Study. *ACS Catal.* **2021**, *11*, 8261–8273. https://doi.org/10.1021/acscatal.1c00956.

(16) Hei, H.; Wang, R.; Liu, X.; He, L.; Zhang, G. Controlled Synthesis and Characterization of Nobel Metal Nanoparticles. *Soft Nanosci. Lett.* **2012**, *02* (03), 34–40. https://doi.org/10.4236/snl.2012.23007.

(17) Long, N. V.; Ohtaki, M.; Nogami, M.; Hien, T. D. Effects of Heat Treatment and Poly(Vinylpyrrolidone) (PVP) Polymer on Electrocatalytic Activity of Polyhedral Pt Nanoparticles towards Their Methanol Oxidation. *Colloid Polym. Sci.* **2011**, *289* (12), 1373–1386. https://doi.org/10.1007/s00396-011-2460-6.

(18) Papa, F.; Negrila, C.; Miyazaki, A.; Balint, I. Morphology and Chemical State of PVP-Protected Pt, Pt-Cu, and Pt-Ag Nanoparticles Prepared by Alkaline Polyol Method. *J. Nanoparticle Res.* **2011**, *13* (10), 5057–5064. https://doi.org/10.1007/s11051-011-0486-9.

(19) Han, S. B.; Song, Y. J.; Lee, J. M.; Kim, J. Y.; Park, K. W. Platinum Nanocube Catalysts for Methanol and Ethanol Electrooxidation. *Electrochem. commun.* **2008**, *10* (7), 1044–1047. https://doi.org/10.1016/j.elecom.2008.04.034.

(20) Song, H.; Kim, F.; Connor, S.; Somorjai, G. A.; Yang, P. Pt Nanocrystals: Shape Control and Langmuir-Blodgett Monolayer Formation. *J. Phys. Chem. B* **2005**. https://doi.org/10.1021/jp0464775.

(21) Herricks, T.; Chen, J.; Xia, Y. Polyol Synthesis of Platinum Nanoparticles: Control of

Morphology with Sodium Nitrate. *Nano Lett.* **2004**, *4* (12), 2367–2371. https://doi.org/10.1021/nl048570a.

(22) Koebel, M. M.; Jones, L. C.; Somorjai, G. A. Preparation of Size-Tunable, Highly Monodisperse PVP-Protected Pt-Nanoparticles by Seed-Mediated Growth. *J. Nanoparticle Res.* **2008**, *10* (6), 1063–1069. https://doi.org/10.1007/s11051-008-9370-7.

(23) Safo, I. A.; Werheid, M.; Dosche, C.; Oezaslan, M. The Role of Polyvinylpyrrolidone (PVP) as a Capping and Structure-Directing Agent in the Formation of Pt Nanocubes. *Nanoscale Adv.* **2019**, *1* (8), 3095–3106. https://doi.org/10.1039/c9na00186g.

(24) Park, J. Y.; Zhang, Y.; Grass, M.; Zhang, T.; Somorjai, G. A. Tuning of Catalytic CO Oxidation by Changing Composition of Rh-Pt Bimetallic Nanoparticles. *Nano Lett.* **2008**, *8* (2), 673–677. https://doi.org/10.1021/nl073195i.

(25) Alayoglu, S.; Eichhorn, B. Rh−Pt Bimetallic Catalysts: Synthesis, Characterization, and Catalysis of Core−Shell, Alloy, and Monometallic Nanoparticles. *J. Am. Chem. Soc.* **2008**, *51*, 17479–17486. https://doi.org/10.1021/ja8061425.

(26) Musselwhite, N.; Alayoglu, S.; Melaet, G.; Pushkarev, V. V.; Lindeman, A. E.; An, K.; Somorjai, G. A. Isomerization of N-Hexane Catalyzed by Supported Monodisperse PtRh Bimetallic Nanoparticles. *Catal. Letters* **2013**, *143* (9), 907–911. https://doi.org/10.1007/s10562-013-1068-5.

(27) Park, J. Y.; Zhang, Y.; Joo, S. H.; Jung, Y.; Somorjai, G. A. Size Effect of RhPt Bimetallic Nanoparticles in Catalytic Activity of CO Oxidation: Role of Surface Segregation. *Catal. Today* **2012**. https://doi.org/10.1016/j.cattod.2011.05.031.

(28) Muri, M. E. Synthesis and Characterization of Free Standing Pt-Rh Nanoparticles, and 2 Wt. % Pt0.70Rh0.30/Al2O3 and 20 Wt. % Co1-x/Al2O3 ($0.00 \leq x \leq 0.15$) Metal-on-Support Catalysts, University of Oslo, 2015.

(29) Bundli, S.; Dhak, P.; Jensen, M.; Gunnæs, A. E.; Nguyen, P. D.; Fjellvåg, H.; Sjåstad, A. O. Controlled Alloying of Pt-Rh Nanoparticles by the Polyol Approach. *J. Alloys Compd.* **2019**, *779*, 879–885. https://doi.org/10.1016/j.jallcom.2018.11.301.

(30) ASM International. *ASM Handbook Volume 3: Alloy Phase Diagrams*; 1998.

(31) Tiwari, K.; Manolata Devi, M.; Biswas, K.; Chattopadhyay, K. Phase Transformation Behavior in Nanoalloys. *Prog. Mater. Sci.* **2021**, *121* (January), 100794. https://doi.org/10.1016/j.pmatsci.2021.100794.

(32) Kusada, K.; Kobayashi, H.; Ikeda, R.; Kubota, Y.; Takata, M.; Toh, S.; Yamamoto, T.; Matsumura, S.; Sumi, N.; Sato, K.; et al. Solid Solution Alloy Nanoparticles of Immiscible Pd and Ru Elements Neighboring on Rh: Changeover of the Thermodynamic Behavior for Hydrogen Storage and Enhanced CO-Oxidizing Ability. *J. Am. Chem. Soc.* **2014**, *136* (5), 1864–1871. https://doi.org/10.1021/ja409464g.

(33) Zhang, Y.; Ahn, J.; Liu, J.; Qin, D. Syntheses, Plasmonic Properties, and Catalytic Applications of Ag-Rh Core-Frame Nanocubes and Rh Nanoboxes with Highly Porous Walls. *Chem. Mater.* **2018**, *30* (6), 2151–2159. https://doi.org/10.1021/acs.chemmater.8b00602.

(34) Zhang, Q.; Kusada, K.; Wu, D.; Ogiwara, N.; Yamamoto, T.; Toriyama, T.; Matsumura, S.; Kawaguchi, S.; Kubota, Y.; Honma, T.; et al. Solid-Solution Alloy Nanoparticles of a Combination of Immiscible Au and Ru with a Large Gap of Reduction Potential and Their Enhanced Oxygen Evolution Reaction Performance. *Chem. Sci.* **2019**, *10* (19), 5133–5137. https://doi.org/10.1039/c9sc00496c.

(35) Huang, B.; Kobayashi, H.; Yamamoto, T.; Matsumura, S.; Nishida, Y.; Sato, K.; Nagaoka, K.; Haneda, M.; Kawaguchi, S.; Kubota, Y.; et al. Coreduction Methodology for Immiscible Alloys of CuRu Solid-Solution Nanoparticles with High Thermal Stability and Versatile Exhaust Purification Ability. *Chem. Sci.* **2020**, *11* (42), 11413–11418. https://doi.org/10.1039/d0sc03373a.

(36) Nuding, M.; Ellner, M. Influence of the Isotypical A9, A10 and B11 Solvents on the Partial Atomic Volume of Tin. *J. Alloys Compd.* **1997**, *252* (1–2), 184–191. https://doi.org/10.1016/S0925-8388(96)02733-8.

(37) Arblaster, J. W. Crystallographic Properties of Rhodium. *Platin. Met. Rev.* **1997**, *41* (4), 184–189.

(38) Raub, E. Metals and Alloys of the Platinum Group. *J. Less Common Met.* **1959**, *1* (1), 3–18. https://doi.org/https://doi.org/10.1016/0022-5088(59)90014-1.

(39) Raub, E.; Falkenburg, G. Das System Gold-Platin-Rhodium Und Die Binären Randsysteme. *Int. J. Mater. Res.* **1964**, *55* (7), 392–397. https://doi.org/doi:10.1515/ijmr-1964-550708.

(40) Arblaster, J. Crystallographic Properties of Platinum. *Platin. Met. Rev.* **1997**, *41* (1), 12–21.

(41) Gibaud, A.; Topić, M.; Corbel, G.; Lang, C. I. An X-Ray Scattering Study of Pt1−xVx Alloys. *J. Alloys Compd.* **2009**, *484* (1–2), 168–171. https://doi.org/10.1016/j.jallcom.2009.05.050.

(42) Bundli, S. A. Syntese Og Karakterisering Av Pt1-XRhx Nanopartikler, University of Oslo, 2016.

(43) Kalyva, M.; Wragg, D. S.; Fjellvåg, H.; Sjåstad, A. O. Engineering Functions into Platinum and Platinum–Rhodium Nanoparticles in a One-Step Microwave Irradiation Synthesis. *ChemistryOpen* **2017**, *6* (2), 273–281. https://doi.org/10.1002/open.201600163.

(44) Song, C.; Yang, A.; Sakata, O.; Kumara, L. S. R.; Hiroi, S.; Cui, Y.-T.; Kusada, K.; Kobayashi, H.; Kitagawa, H. Size Effects on Rhodium Nanoparticles Related to Hydrogen-Storage Capability. *Phys. Chem. Chem. Phys.* **2018**, *20* (22), 15183–15191. https://doi.org/10.1039/C8CP01678J.

(45) Salgado, J. R. C.; Quintana, J. J.; Calvillo, L.; Lázaro, M. J.; Cabot, P. L.; Esparbé, I.; Pastor, E. Carbon Monoxide and Methanol Oxidation at Platinum Catalysts Supported on Ordered Mesoporous Carbon: The Influence of Functionalization of the Support. *Phys. Chem. Chem. Phys.* **2008**, *10* (45), 6796. https://doi.org/10.1039/b809227c.

(46) Wang, Z. L.; Petroski, J. M.; Green, T. C.; El-Sayed, M. A. Shape Transformation and Surface Melting of Cubic and Tetrahedral Platinum Nanocrystals. *J. Phys. Chem. B* **1998**, *102* (32), 6145–6151. https://doi.org/10.1021/jp981594j.

(47) Yu, R.; Song, H.; Zhang, X.-F.; Yang, P. Thermal Wetting of Platinum Nanocrystals on Silica Surface. *J. Phys. Chem. B* **2005**, *109* (15), 6940–6943. https://doi.org/10.1021/jp050973r.

(48) Kirchhoff, M.; Specht, U.; Veser, G. Engineering High-Temperature Stable Nanocomposite Materials. *Nanotechnology* **2005**, *16* (7). https://doi.org/10.1088/0957-4484/16/7/014.

(49) Sanders, T.; Papas, P.; Veser, G. Supported Nanocomposite Catalysts for High-Temperature Partial Oxidation of Methane. *Chem. Eng. J.* **2008**, *142* (1), 122–132. https://doi.org/10.1016/j.cej.2008.04.018.

(50) Cao, A.; Veser, G. Exceptional High-Temperature Stability through Distillation-like Self-Stabilization in Bimetallic Nanoparticles. *Nat. Mater.* **2010**, *9* (1), 75–81. https://doi.org/10.1038/nmat2584.

(51) Huang, X.; Liu, Z.; Millet, M. M.; Dong, J.; Plodine, M.; Ding, F.; Schlögl, R.; Willinger, M. G. In Situ Atomic-Scale Observation of Surface-Tension-Induced Structural Transformation of Ag-NiPx Core-Shell Nanocrystals. *ACS Nano* **2018**, *12* (7), 7197–7205. https://doi.org/10.1021/acsnano.8b03106.

(52) Bonifacio, C. S.; Carenco, S.; Wu, C. H.; House, S. D.; Bluhm, H.; Yang, J. C. Thermal Stability of Core-Shell Nanoparticles: A Combined in Situ Study by XPS and TEM. *Chem. Mater.* **2015**, *27* (20), 6960–6968. https://doi.org/10.1021/acs.chemmater.5b01862.

(53) Jia, C. J.; Schüth, F. Colloidal Metal Nanoparticles as a Component of Designed Catalyst. *Phys. Chem. Chem. Phys.* **2011**, *13* (7), 2457–2487. https://doi.org/10.1039/c0cp02680h.

(54) Polte, J. Fundamental Growth Principles of Colloidal Metal Nanoparticles - a New Perspective. *CrystEngComm* **2015**, *17* (36), 6809–6830. https://doi.org/10.1039/c5ce01014d.

(55) Kwon, S. G.; Hyeon, T. Formation Mechanisms of Uniform Nanocrystals via Hot-Injection and Heat-up Methods. *Small* **2011**, *7* (19), 2685–2702. https://doi.org/10.1002/smll.201002022.

(56) LaMer, V. K.; Dinegar, R. H. Theory, Production and Mechanism of Formation of Monodispersed Hydrosols. *J. Am. Chem. Soc.* **1950**, *72* (11), 4847–4854.

(57) Reiss, H. The Growth of Uniform Colloidal Dispersions. *J. Chem. Phys.* **1951**, 482–487.

(58) Mozaffari, S.; Li, W.; Dixit, M.; Seifert, S.; Lee, B.; Kovarik, L.; Mpourmpakis, G.; Karim, A. M. The Role of Nanoparticle Size and Ligand Coverage in Size Focusing of Colloidal Metal Nanoparticles. *Nanoscale Adv.* **2019**, *1* (10), 4052–4066. https://doi.org/10.1039/C9NA00348G.

(59) Thanh, N. T. K.; Maclean, N.; Mahiddine, S. Mechanisms of Nucleation and Growth of Nanoparticles in Solution. *Chem. Rev.* **2014**, *114* (15), 7610–7630. https://doi.org/10.1021/cr400544s.

(60) Hornyak, G. L. *Introduction to Nanoscience & Nanotechnology*; CRC Press: Boca Raton, FL, 2009.

(61) Kamyshny, A.; Magdassi, S. Aqueous Dispersions of Metallic Nanoparticles: Preparation, Stabilization and Application in Nanoscience: Colloidal and Interfacial Aspects. *Surfactant Sci. Ser.* **2009**, *147*, 747–778.

(62) Hiemenz, P. C.; R, R. *Principles of Colloid and Surface Chemistry*, 3rd ed.; Marcel Dekker: New York, NY, 1997.

(63) Li, J.; Inukai, K.; Takahashi, Y.; Tsuruta, A.; Shin, W. Effect of PVP on the Synthesis of High-Dispersion Core–Shell Barium-Titanate–Polyvinylpyrrolidone Nanoparticles. *J. Asian Ceram. Soc.* **2017**, *5* (2), 216–225. https://doi.org/10.1016/j.jascer.2017.05.001.

(64) Park, J.; Joo, J.; Soon, G. K.; Jang, Y.; Hyeon, T. Synthesis of Monodisperse Spherical Nanocrystals. *Angew. Chemie - Int. Ed.* **2007**, *46* (25), 4630–4660. https://doi.org/10.1002/anie.200603148.

(65) Hyeon, T. Chemical Synthesis of Magnetic Nanoparticles. *Chem. Commun.* **2003**, *3* (8), 927–934. https://doi.org/10.1039/b207789b.

(66) Van Embden, J.; Chesman, A. S. R.; Jasieniak, J. J. The Heat-up Synthesis of Colloidal Nanocrystals. *Chem. Mater.* **2015**, *27* (7), 2246–2285. https://doi.org/10.1021/cm5028964.

(67) Kawasaki, H. Surfactant-Free Solution-Based Synthesis of Metallic Nanoparticles toward Efficient Use of the Nanoparticles ' Surfaces and Their Application in Catalysis and Chemo-/Biosensing. *Nanotechnol. Rev.* **2013**, *2* (1), 5–25. https://doi.org/10.1515/ntrev-2012-0079.

(68) Aliofkhazraei, M. *Handbook of Nanoparticles*; 2015. https://doi.org/10.1007/978-3-319-15338-4.

(69) Jensen, M. Synthesis and Characterization of Pt1-XPdx Nanoparticles and Their Suitability for NH3 Oxidation Catalysis, University of Oslo, 2017.

(70) Atkins, P.; de Paula, J. *Physical Chemistry Thermodynamics, Structure, and Change*, 10th ed.; W. H. Freeman and Company: New York, NY, 2014.

(71) Rumble, J. R. *CRC Handbook of Chemistry and Physics*, 102nd (Int.; CRC Press/Taylor & Francis: Boca Raton, FL, 2021.

(72) Chen, X.; Shangguan, W. Hydrogen Production from Water Splitting on CdS-Based Photocatalysts Using Solar Light. *Front. Energy* **2013**, *7* (1), 111–118. https://doi.org/10.1007/s11708-012-0228-4.

(73) Biacchi, A. J.; Schaak, R. E. The Solvent Matters: Kinetic versus Thermodynamic Shape Control in the Polyol Synthesis of Rhodium Nanoparticles. *ACS Nano* **2011**, *5* (10), 8089–8099. https://doi.org/10.1021/nn2026758.

(74) Niu, Z.; Peng, Q.; Gong, M.; Rong, H.; Li, Y. Oleylamine-Mediated Shape Evolution of Palladium Nanocrystals. *Angew. Chemie - Int. Ed.* **2011**, *50* (28), 6315–6319. https://doi.org/10.1002/anie.201100512.

(75) Fievet, F.; Lagier, J. P.; Blin, B.; Beaudoin, B.; Figlarz, M. Homogeneous and Heterogeneous Nucleations in the Polyol Process for the Preparation of Micron and Submicron Size Metal Particles. *Solid State Ionics* **1989**, *32–33* (PART 1), 198–205. https://doi.org/10.1016/0167-2738(89)90222-1.

(76) An, K.; Somorjai, G. A. Nanocatalysis I: Synthesis of Metal and Bimetallic Nanoparticles and Porous Oxides and Their Catalytic Reaction Studies. *Catal. Letters* **2015**, *145* (1), 233–248. https://doi.org/10.1007/s10562-014-1399-x.

(77) Ferrando, R.; Jellinek, J.; Johnston, R. L. Nanoalloys: From Theory to Applications of Alloy Clusters and Nanoparticles. *Chem. Rev.* **2008**, *108* (3), 845–910. https://doi.org/10.1021/cr040090g.

(78) Dai, S.; You, Y.; Zhang, S.; Cai, W.; Xu, M.; Xie, L.; Wu, R.; Graham, G. W.; Pan, X. In Situ Atomic-Scale Observation of Oxygen-Driven Core-Shell Formation in Pt3Co Nanoparticles. *Nat. Commun.* **2017**, *8* (1), 1–8. https://doi.org/10.1038/s41467-017-00161-y.

(79) Lu, N.; Wang, J.; Xie, S.; Xia, Y.; Kim, M. J. Enhanced Shape Stability of Pd-Rh Core-Frame Nanocubes at Elevated Temperature: In Situ Heating Transmission Electron Microscopy. *Chem. Commun.* **2013**, *49* (100), 11806–11808. https://doi.org/10.1039/c3cc46465b.

(80) Wang, D.; Li, Y. Bimetallic Nanocrystals: Liquid-Phase Synthesis and Catalytic Applications. *Adv. Mater.* **2011**, *23* (9), 1044–1060. https://doi.org/10.1002/adma.201003695.

(81) Gilroy, K. D.; Ruditskiy, A.; Peng, H. C.; Qin, D.; Xia, Y. Bimetallic Nanocrystals: Syntheses, Properties, and Applications. *Chem. Rev.* **2016**, *116* (18), 10414–10472. https://doi.org/10.1021/acs.chemrev.6b00211.

(82) Tojo, C.; Buceta, D.; López-Quintela, M. A. On Metal Segregation of Bimetallic Nanocatalysts Prepared by a One-Pot Method in Microemulsions. *Catalysts* **2017**, *7* (2), 17–21. https://doi.org/10.3390/catal7020068.

(83) An, K.; Somorjai, G. A. Size and Shape Control of Metal Nanoparticles for Reaction Selectivity in Catalysis. *ChemCatChem* **2012**, *4* (10), 1512–1524. https://doi.org/10.1002/cctc.201200229.

(84) Mehrabadi, B. A. T.; Eskandari, S.; Khan, U.; White, R. D.; Regalbuto, J. R. A Review of Preparation Methods for Supported Metal Catalysts; 2017; pp 1–35. https://doi.org/10.1016/bs.acat.2017.10.001.

(85) Chan, K.-Y.; Ding, J.; Ren, J.; Cheng, S.; Tsang, K. Y. Supported Mixed Metal Nanoparticles as Electrocatalysts in Low Temperature Fuel Cells. *J. Mater. Chem.* **2004**, *14* (4), 505. https://doi.org/10.1039/b314224h.

(86) Linares, N.; Serrano, E.; Rico, M.; Mariana Balu, A.; Losada, E.; Luque, R.; García-

Martínez, J. Incorporation of Chemical Functionalities in the Framework of Mesoporous Silica. *Chem. Commun.* **2011**, *47* (32), 9024–9035. https://doi.org/10.1039/c1cc11016k.

(87) Maciejewski, M.; Fabrizioli, P.; Grunwaldt, J. D.; Becker, O. S.; Baiker, A. Supported Gold Catalysts for CO Oxidation: Effect of Calcination on Structure, Adsorption and Catalytic Behaviour. *Phys. Chem. Chem. Phys.* **2001**, *3* (17), 3846–3855. https://doi.org/10.1039/b101184g.

(88) Comotti, M.; Li, W. C.; Spliethoff, B.; Schüth, F. Support Effect in High Activity Gold Catalysts for CO Oxidation. *J. Am. Chem. Soc.* **2006**, *128* (3), 917–924. https://doi.org/10.1021/ja0561441.

(89) Borodko, Y.; Habas, S. E.; Koebel, M.; Yang, P.; Frei, H.; Somorjai, G. A. Probing the Interaction of Poly(Vinylpyrrolidone) with Platinum Nanocrystals by UV - Raman and FTIR. *J. Phys. Chem. B* **2006**, *110* (46), 23052–23059. https://doi.org/10.1021/jp063338.

(90) Rinaldi, R.; Porcari, A. de M.; Rocha, T. C. R.; Cassinelli, W. H.; Ribeiro, R. U.; Bueno, J. M. C.; Zanchet, D. Construction of Heterogeneous Ni Catalysts from Supports and Colloidal Nanoparticles - A Challenging Puzzle. *J. Mol. Catal. A Chem.* **2009**, *301* (1–2), 11–17. https://doi.org/10.1016/j.molcata.2008.11.001.

(91) Lee, I.; Morales, R.; Albiter, M. A.; Zaera, F. Synthesis of Heterogeneous Catalysts with Well Shaped Platinum Particles to Control Reaction Selectivity. *Proc. Natl. Acad. Sci. U. S. A.* **2008**, *105* (40), 15241–15246. https://doi.org/10.1073/pnas.0805691105.

(92) Singh, A.; Chandler, B. D. Low-Temperature Activation Conditions for PAMAM Dendrimer Templated Pt Nanoparticles. *Langmuir* **2005**, *21* (23), 10776–10782. https://doi.org/10.1021/la051605h.

(93) Hua, Q.; Cao, T.; Gu, X.-K.; Lu, J.; Jiang, Z.; Pan, X.; Luo, L.; Li, W.-X.; Huang, W. Crystal-Plane-Controlled Selectivity of Cu 2 O Catalysts in Propylene Oxidation with Molecular Oxygen . *Angew. Chemie* **2014**, *126* (19), 4956–4961. https://doi.org/10.1002/ange.201402374.

(94) Leng, Y. *Materials Characterization*, Second.; Wiley-VCH: Weinheim, 2013.

(95) Williams, D. B.; Carter, C. B. *Transmission Electron Microscopy*, Second Edi.; Springer: New York, NY, 2009.

(96) Egerton, R. F. Dose Measurement in the TEM and STEM. *Ultramicroscopy* **2021**, *229* (July), 113363. https://doi.org/10.1016/j.ultramic.2021.113363.

(97) Nakayama, H.; Nagata, M.; Abe, H.; Shimizu, Y. In Situ TEM Study of Rh Particle Sintering for Three-Way Catalysts in High Temperatures. *Catalysts* **2020**, *11* (1), 19. https://doi.org/10.3390/catal11010019.

(98) https://www.protochips.com.

(99) Rietveld, H. A Profile Refinement Method for Nuclear and Magnetic Structures. *J. Appl. Crystallogr.* **1969**, No. 2, 65–71.

(100) Tilley, R. J. D. *Understanding Solids, The Science of Materials*, Second.; Wiley: West Sussex, 2013.

(101) Callister, W. D.; Rethwisch, D. G. *Materials Science and Engineering: An Introduction*, 10th ed.; Wiley, 2018.

(102) Termaks TS 8056 https://medtekn.no/nkkn2/nkkn.php?TypeCode=16460.

(103) Coelho, A. A. TOPAS and TOPAS-Academic : An Optimization Program Integrating Computer Algebra and Crystallographic Objects Written in C++. *J. Appl. Crystallogr.* **2018**, *51* (1), 210–218. https://doi.org/10.1107/S1600576718000183.

(104) Belsky, A.; Hellenbrandt, M.; Karen, V. L.; Luksch, P. New Developments in the Inorganic Crystal Structure Database (ICSD): Accessibility in Support of Materials Research and Design. *Acta Crystallogr. Sect. B Struct. Sci.* **2002**, *58* (3), 364–369. https://doi.org/10.1107/S0108768102006948.

(105) DIFFRAC.EVA. Bruker AXS 2020.

(106) Gates-Rector, S.; Blanton, T. The Powder Diffraction File: A Quality Materials Characterization Database. *Powder Diffr.* **2019**, *34* (4), 352–360. https://doi.org/10.1017/S0885715619000812.

(107) Velox Acquisition and Processing User Manual. Thermo Fisher Scientific 2021, p 214.

(108) Morrison, I. D.; Sydney, R. *Colloidal Dispersions: Suspensions, Emulsions, and Foams*; Wiley-Interscience: New York, NY, 2002.

(109) Mourdikoudis, S.; Liz-Marzán, L. M. Oleylamine in Nanoparticle Synthesis. *Chem. Mater.* **2013**, *25* (9), 1465–1476. https://doi.org/10.1021/cm4000476.

(110) Yang, Z.; Klabunde, K. J. Synthesis of Nearly Monodisperse Palladium (Pd) Nanoparticles by Using Oleylamine and Trioctylphosphine Mixed Ligands. *J. Organomet. Chem.* **2009**, *694* (7–8), 1016–1021. https://doi.org/10.1016/j.jorganchem.2008.11.030.

(111) Oxtoby, D.; Gillis, H. P.; Campion, A. *Principles of Modern Chemistry*, 7th ed.; Brooks/Cole: Belmont, CA.

(112) Jensen, M.; Gonano, B.; Kierulf-Vieira, W.; Kooyman, P.; Sjåstad, A. Innovative Approach to Controlled Pt-Rh Bimetallic Nanoparticle Synthesis. *Artic. Submitt. to RSC Adv.* **2022**, *Manuscript*.

(113) Zhou, R. -S; Snyder, R. L. Structures and Transformation Mechanisms of the η, γ and θ Transition Aluminas. *Acta Crystallogr. Sect. B* **1991**, *47* (5), 617–630. https://doi.org/10.1107/S0108768191002719.

(114) Zacharaki, E.; Kalyva, M.; Fjellvåg, H.; Sjåstad, A. O. Burst Nucleation by Hot Injection for Size Controlled Synthesis of ε-Cobalt Nanoparticles. *Chem. Cent. J.* **2016**, *10* (1), 1–11. https://doi.org/10.1186/s13065-016-0156-1.

(115) Bonet, F.; Delmas, V.; Grugeon, S.; Herrera Urbina, R.; Silvert, P.-Y.; Tekaia-Elhsissen, K. Synthesis of Monodisperse Au, Pt, Pd, Ru and Ir Nanoparticles in Ethylene Glycol. *Nanostructured Mater.* **1999**, *11* (8), 1277–1284. https://doi.org/10.1016/S0965-9773(99)00419-5.

(116) Zacharaki, E.; Beato, P.; Tiruvalam, R. R.; Andersson, K. J.; Fjellvåg, H.; Sjåstad, A. O. From Colloidal Monodisperse Nickel Nanoparticles to Well-Defined Ni/Al 2 O 3 Model Catalysts. *Langmuir* **2017**, *33* (38), 9836–9843. https://doi.org/10.1021/acs.langmuir.7b02197.

(117) Kawaguchi, T.; Keller, T. F.; Runge, H.; Gelisio, L.; Seitz, C.; Kim, Y. Y.; Maxey, E. R.; Cha, W.; Ulvestad, A.; Hruszkewycz, S. O.; et al. Gas-Induced Segregation in Pt-Rh Alloy Nanoparticles Observed by in Situ Bragg Coherent Diffraction Imaging. *Phys. Rev. Lett.* **2019**, *123* (24), 246001. https://doi.org/10.1103/PhysRevLett.123.246001.

(118) Steiner, C.; Schönfeld, B.; Portmann, M. J.; Kompatscher, M.; Kostorz, G.; Mazuelas, A.; Metzger, T.; Kohlbrecher, J.; Demé, B. Local Order in Pt-47 at.% Rh Measured with x-Ray and Neutron Scattering. *Phys. Rev. B - Condens. Matter Mater. Phys.* **2005**, *71* (10), 1–7. https://doi.org/10.1103/PhysRevB.71.104204.

(119) Bieber, A.; Gautier, F. Overview No. 54 Segregation and Order in Binary Substitutional Transition Metal Alloys—I. Homogeneous Ordered Structures in the Ground State: General Trends. *Acta Metall.* **1986**, *34* (12), 2291–2309. https://doi.org/10.1016/0001-6160(86)90133-1.

(120) Lu, Z. W.; Wei, S.-H.; Zunger, A. Long-Range Order in Binary Late-Transition-Metal Alloys. *Phys. Rev. Lett.* **1991**, *66* (13), 1753–1756. https://doi.org/10.1103/PhysRevLett.66.1753.

(121) Lu, Z. W.; Klein, B. M.; Zunger, A. Ordering Tendencies in Pd-Pt, Rh-Pt, and Ag-Au Alloys. *J. Phase Equilibria* **1995**, *16* (1), 36–45. https://doi.org/10.1007/BF02646247.

(122) Maisel, S. B.; Kerscher, T. C.; Müller, S. No Miscibility Gap in Pt–Rh Binary Alloys: A First-Principles Study. *Acta Mater.* **2012**, *60* (3), 1093–1098. https://doi.org/10.1016/j.actamat.2011.10.020.

(123) Lemaitre, J. *Handbook of Materials Behavior Models*, 1st ed.; Academic Press, 2001.

(124) Kumar, S.; Waller, D.; Fjellvåg, H.; Sjåstad, A. O. Development of Custom Made Bimetallic Alloy Model Systems Based on Platinum – Rhodium for Heterogeneous Catalysis. *J. Alloys Compd.* **2019**, *786*, 1021–1029. https://doi.org/10.1016/j.jallcom.2019.02.026.

(125) Xiong, G.; Clark, J. N.; Nicklin, C.; Rawle, J.; Robinson, I. K. Atomic Diffusion within Individual Gold Nanocrystal. *Sci. Rep.* **2015**, *4* (1), 6765.

https://doi.org/10.1038/srep06765.

(126) Yasuda, H.; Mori, H.; Komatsu, M.; Takeda, K. Spontaneous Alloying of Copper Atoms into Gold Clusters at Reduced Temperatures. *J. Appl. Phys.* **1993**, *73* (3), 1100–1103. https://doi.org/10.1063/1.353272.

(127) Yang, J.; Ying, J. Y. Diffusion of Gold from the Inner Core to the Surface of Ag2S Nanocrystals. *J. Am. Chem. Soc.* **2010**, *132* (7), 2114–2115. https://doi.org/10.1021/ja909078p.

(128) Shibata, T.; Bunker, B. A.; Zhang, Z.; Meisel, D.; Vardeman, C. F.; Gezelter, J. D. Size-Dependent Spontaneous Alloying of Au−Ag Nanoparticles. *J. Am. Chem. Soc.* **2002**, *124* (40), 11989–11996. https://doi.org/10.1021/ja026764r.

(129) Borodko, Y.; Lee, H. S.; Joo, S. H.; Zhang, Y.; Somorjai, G. Spectroscopic Study of the Thermal Degradation of PVP-Capped Rh and Pt Nanoparticles in H 2 and O 2 Environments. *J. Phys. Chem. C* **2010**, *114* (2), 1117–1126. https://doi.org/10.1021/jp909008z.

(130) Nadler, M. R.; Kempter, C. P. SOME SOLIDUS TEMPERATURES IN SEVERAL METAL—CARBON SYSTEMS. *J. Phys. Chem.* **1960**, *64* (10), 1468–1471. https://doi.org/10.1021/j100839a028.

9 Appendix

Table A.1 Raw data and calculation for the amount of Al_2O_3 to be used to prepare 0.5 % weight percent Pt (Synthesis 15) and solid solution $Pt_{0.50}Rh_{0.50}$ (Synthesis 18) supported on Al_2O_3.

	Relevant molar mass for calculations	
	$Pt(acac)_2$ [g/mol]	393.29
	$Rh(acac)_3$ [g/mol]	400.23
	Pt [g/mol]	195.08
	Rh [g/mol]	102.91
Estimation for the mass of Al_2O_3	**Pt NPs**	**$Pt_{0.5}Rh_{0.5}$ NPs**
Mass of $Pt(acac)_2$ [g]	0.0294	0.0594
Mass of $Rh(acac)_3$ [g]	0	0.0204
Mass of Pt [g]	0.01458301	0.029463632
Mass of Rh [g]	0	0.005245394
moles $Pt(acac)_2$ [mol]	0.00007	0.000151
millimoles $Pt(acac)_2$ [mmol]	0.07	0.1510
moles $Rh(acac)_3$ [mol]	0	0.000051
millimoles $Rh(acac)_3$ [mmol]	0.000	0.051
	Assume 70 % yield	Assume 35 % yield of Rh
		n(Rh) = n(Pt)
Moles of Rh [mol]	0	1.78397E-05
Moles of Pt [mol]	5.23278E-05	1.78397E-05
Total mass of Rh recovered [g]	0	0.001835888
Total mass of Pt recovered [g]	0.010208107	0.003480177
Total mass of metal recovered [g]	0.010208107	0.005316065
Want 0.5 wt.% metal on Al_2O_3	0.50%	0.50%
Mass of Al_2O_3 to be used [g]	**2.03**	**1.06**

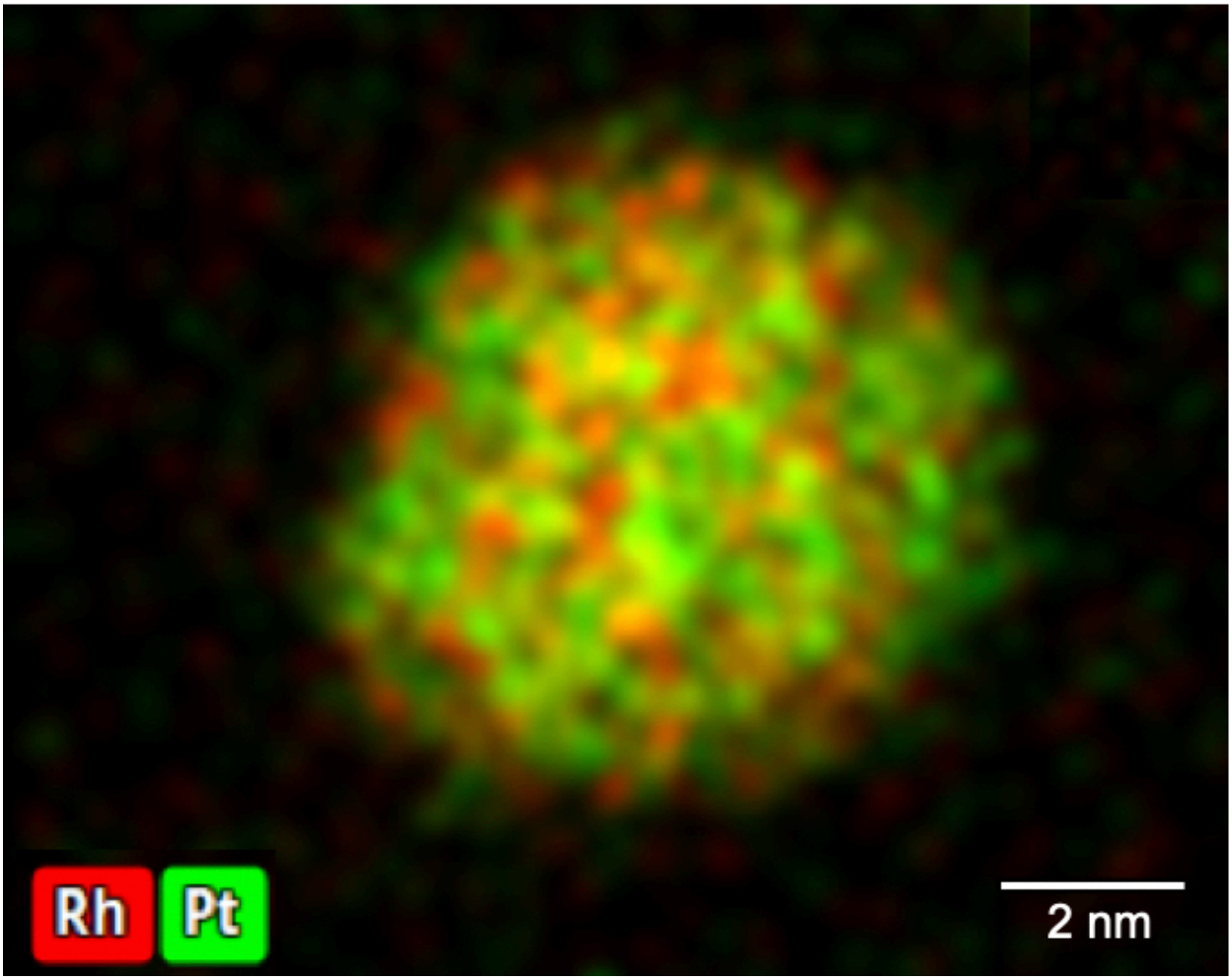

Figure A.1 STEM–EDS elemental map image of a representative nanoparticle from Synthesis 18. The EDS signal for Rh is shown in red and for Pt in green.

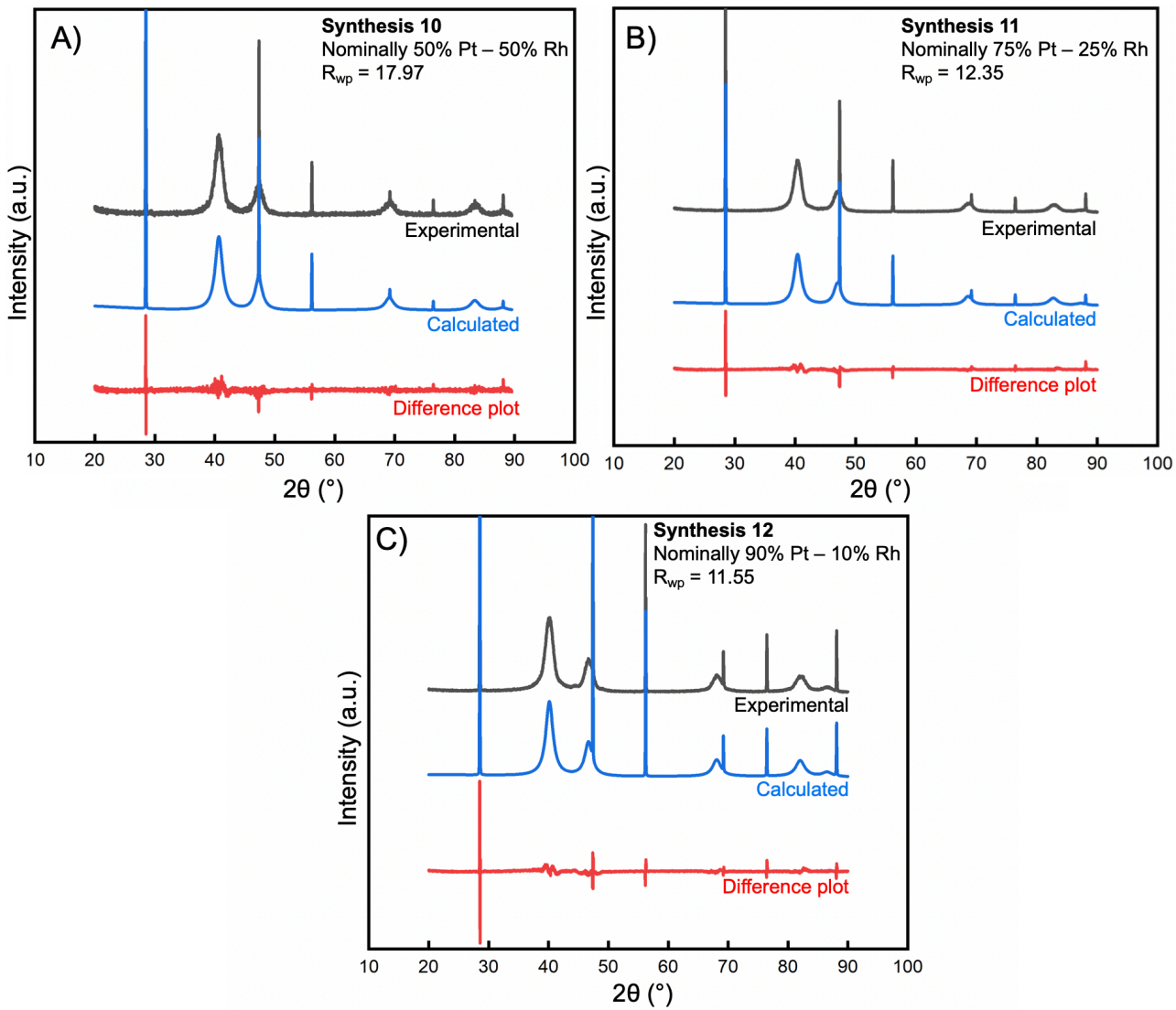

Figure A.2: Rietveld refinement raw data for the powder X-ray diffraction patterns of the product from A) Synthesis 10; B) Synthesis 11; C) Synthesis 12. The black line shows the experimental data, the blue line the calculated theoretical diffractogram and the red line the difference plot between the calculated and the theoretical diffractogram